# INNOVATIVE DESIGN FOR CYCLONE SEPARATORS AND PLATE HEAT EXCHANGERS USING COMPUTATIONAL FLUID DYNAMICS

By

Sai Guruprasad Jakkala

A DISSERTATION

Submitted to
Michigan State University
in partial fulfillment of the requirements
for the degree of

Mechanical Engineering - Doctor of Philosophy

2024

## ABSTRACT

A majority of equipment used in industry operate in the turbulent flow regime. Design of these equipment requires many iterations, often performed using computer simulations. Turbulence modelling is computationally expensive and time-consuming. In this study we investigate different turbulence models and their application in designing cyclone separators and novel plate heat exchangers. The performance of the various models are studied and the simulations are used to provide insight and guidance on the redesign of these two important systems. Cyclone separators and heat exchangers are ubiquitous in industry.

A good understanding of the flow features in cyclone separators is paramount to efficiently use them. The turbulent fluid flow characteristics are modeled using Unsteady Reynolds Averaged Navier-Stokes (URANS), Large Eddy Simulations (LES), and hybrid LES/RANS turbulent models. The hybrid LES/RANS approaches, namely, detached eddy simulation (DES), delayed detached eddy simulation (DDES), and improved delayed detached eddy simulation (IDDES) based on the k-omega SST RANS approaches are explored. The study is carried out for three different inlet velocities. The results from hybrid LES/RANS models are shown to be in good agreement with the experimental data available in the literature. Reduction in computational time and mesh size are the two main benefits of using hybrid LES/RANS models over the traditional LES methods. The Reynolds stresses are observed to understand the redistribution of turbulent energy in the flow field. The velocity profiles and vorticity quantities are explored to obtain a better understanding of the behavior of fluid flow in cyclone separators. The better prediction of turbulent quantities from the hybrid models can help in better modeling the multiphase interactions. Using the improved turbulent quantity predictions, we are able to design a cyclone separator for reduced erosion.

Supercritical CO2 cycles operating with high efficiency require new heat exchangers which can operate at high temperature (above 800$^o$C) and high pressure (above 80 bar) with tens of thousands of hours of operation. In this thesis, we discuss modified metallic plate heat exchangers which can withstand high temperature and high pressure with

new twisted S-shaped fins. Novel 3D twisted S-shaped fins are developed for better heat exchanger performance. The fins have a twist to induce a swirl in the flow resulting in enhanced heat transfer. Ni-based superalloy Haynes 214 is the material used for the heat exchanger plates and fins. The heat exchanger is manufactured using additive manufacturing processes. Turbulent Conjugate Heat Transfer simulations are carried out to obtain the temperature and pressure profiles in the heat exchanger in the turbulent regime. A parametric study is conducted to determine the performance of the newly developed 3D twisted S-shaped fins. The CFD results are compared with experiments.

The studies in this thesis resulted in an improved cyclone separator design which has improved operating life due to reduced erosion (maximum of 90%) without much compromise on the efficiency. 3D twisted S-shaped fins provide a better Performance Efficient Coefficient (PEC) than S-shaped fins. There is an improvement of 10%-13% better performance. There is considerable reduction (up to 75%) in the pumping requirement for 3D twisted S-shaped fins.

## ACKNOWLEDGMENTS

First, I would like to express my gratitude to my advisor, Professor Andre Benard. He is the one who saw potential in me to do PhD and hired me as a graduate research assistant in his research lab. He has taught me how to be persistent in doing research without being frustrated. I would like to thank him for being patient with my shortcomings and inadequacies.

I would like to thank Dr. S. Vengadesan for giving me the opportunity to explore the Joint Degree Program (JDP). This program has helped me gain exposure in research at international level. He has also constantly pushed me to do good work.

My colleagues at both IIT Madras and Michigan State University have been a constant source of inspiration. Shyam in particular has been helping me better myself. Anshul has been a great roommate and I enjoy discussing research with him. Parnab has helped me in navigating my first few months in USA.

Finally, mere words cannot express my deep gratitude for my parents and brother. This journey would not be possible without their unconditional support, sacrifices, and unwavering belief in me.

The support for this work by U.S. Department of Energy, Advanced Research Projects Agency–Energy (ARPA-E), under Award no. DE-AR0001123, is gratefully acknowledged.

## TABLE OF CONTENTS

## LIST OF FIGURES

## LIST OF TABLES

# Chapter 1

# Introduction

## 1.1 Motivation

Fluid mechanics is a fundamental discipline in the industrial sector, playing a crucial role in the design, analysis, and optimization of various equipment and processes. Understanding fluid behavior is essential for developing efficient systems such as pumps, turbines, compressors, and heat exchangers, which are integral to industries ranging from energy production to chemical manufacturing. Accurate fluid mechanics models enable engineers to predict and enhance the performance of these systems, leading to improved energy efficiency, reduced operational costs, and increased reliability. Experiments and numerical methods are two different ways to analyze fluid motion around us.

Computational fluid dynamics (CFD) is a powerful numerical tool that is increasingly being used in the design of industrial equipment. CFD simulations allow engineers to predict the behavior of fluids (such as gases and liquids) within complex systems, providing valuable insights that can help optimize the design of equipment for various applications. By leveraging the capabilities of CFD, engineers can save time and resources by identifying potential problems early in the design process, reducing the need for costly and time-consuming physical testing. As a result, the use of CFD in industrial equipment design has become essential for achieving efficient and effective operation.

Turbulence is a phenomenon found in many industrial flows. Turbulence is random and requires additional modelling to understand it. The Reynolds Averaged Navier-Stokes (RANS) equations are developed to understand turbulence. The RANS equations require a closure for the equations to be solved. The closure for the RANS models results in many turbulence models. The best turbulence model to use in a given situation depends on a number of factors, such as the type of flow, the flow conditions, and the accuracy and computational cost required for the analysis. In general, however, the Reynolds-averaged Navier-Stokes (RANS) equations are widely used for turbulence modeling, as they are able to provide good predictions for a wide range of flows.

Within the RANS models, there are various turbulence models that can be used to represent the turbulent motion of the fluid. Some common turbulence models include the $k-\epsilon$ model, the $k-\omega$ model, and the Reynolds stress model (RSM). These models differ in their complexity and ability to capture the details of the turbulent flow, with the RSM being the most advanced and accurate but also the most computationally expensive and complex.

Overall, the best turbulence model to use in a given situation will depend on the specific requirements of the analysis and the trade-off between accuracy and computational cost. Large Eddy Simulations (LES) are more accurate turbulence models than RANS, but they consume a lot of computational time and resources. To overcome the expensive cost of running LES, hybrid LES/RANS models have been developed which try to provide advantages of both RANS and LES. These hybrid models solve in the RANS mode near the wall region and scale resolving mode away from the wall. To choose a turbulence model for a particular CFD problem requires some testing and effort.

Two industrial equipment chosen for study in this thesis is the cyclone separator and plate heat exchanger. These two industrial equipment are widely used and there is a need for constant improvement in these equipment. These equipment operate in the turbulent regime and there is a lot of modelling effort required to get accurate results.

Cyclone separators are important for several reasons. They are widely used in various industries to separate and remove solid particles from a fluid stream, such as dust and debris from air or particulate matter from wastewater. This separation is important to prevent damage to downstream equipment, improve product quality, and protect the environment. Cyclone separators are also highly efficient, with some designs achieving separation efficiencies of over 90%. Additionally, they are relatively inexpensive and require minimal maintenance, making them a cost-effective solution for many applications. Overall, cyclone separators play a crucial role in a wide range of industries and are essential for maintaining the quality and performance of industrial equipment.

Plate heat exchangers are important in many industrial and commercial applications because they are highly efficient and versatile. A plate heat exchanger consists of a series

of metal plates that are arranged in a corrugated pattern, with a small gap between each plate. This design allows for a large surface area for heat transfer, allowing the heat exchanger to operate at a high rate of heat transfer. Additionally, the plates can be easily removed and replaced, allowing for easy cleaning and maintenance. This makes plate heat exchangers ideal for a wide range of applications, including HVAC, food processing, and chemical processing. Overall, plate heat exchangers are an essential component of many industrial and commercial systems, providing efficient and effective heat transfer capabilities. The heat exchangers in this study are developed for supercritical $CO_2$ applications. These heat exchangers need to perform at high temperatures (¿800$^o$ C) and high pressure (25 MPa). It requires new materials and manufacturing methods to develop such heat exchangers which will have good creep strength.

## 1.2 Objective

The objective of this work is to use CFD tools to improve the designs of cyclone separators and plate heat exchangers. Turbulence modelling is widely present in the devices being used in the industry. Cyclone separators involve multiphase flows and we utilize the Lagrangian approach to track the particles. With accurate prediction of hydrodynamics and particle motion in cyclone separators, we aim to reduce the erosion in cyclone separators. The heat exchangers involve heat transfer and require the energy equation to be solved. Novel 3D twisted S-shaped fins are developed to improve the thermo-hydraulic performance of heat exchangers.

## 1.3 Thesis Organization

- Chapter 2 provides a brief review of the existing work done in the area of cyclone separators and plate heat exchangers.
- Chapter 3 discusses the modelling of cyclone separators and lagrangian modelling of particle phase in the cyclone separator to reduce the overall erosion in the cyclone separator.

- Chapter 4 discusses the novel 3D twisted S-shaped fins developed for plate heat exchangers.
- Chapter 5 discusses the design of a single plate heat exchanger, graphite heater for high temperature application and full scale plate heat exchanger simulations.
- The last chapter summarizes the conclusions made in this study and the scope of future work.

# Chapter 2

# Literature Review

## 2.1 Cyclone Separators

The occurrences of cyclone separators are ubiquitous in industries where there is a need for separating two phases such as solid–liquid, liquid–liquid, or liquid–gas. For example, they may be used to separate solid particles from liquids in mining industries, oil droplets from water in petroleum purification, plastics from water, etc. Sawmills use large-scale cyclone separators to remove sawdust from extracted air. Cement industries also use cyclone separators as a process in kiln preheaters. Industrial and professional kitchen ventilation employs cyclone separators to separate grease from exhaust air. Having numerous applications, it is key to understand the behavior of fluid flow in cyclone separators to optimize the designs for particular applications. A cyclone separator typically has a tangential inlet for the feed and two outlets (at the top and bottom). The inlet feeds into a cylindrical section followed by a conical section and finally into a bin. The heavier phase exits through the bin, whereas the lighter phase exits through the vortex finder. Due to its simple geometry and high throughput, it is used extensively in industrial processes. The flow-field characteristics observed in cyclone separators are predominantly turbulent and multiphase in nature. The design of cyclone separators is usually done using empirical correlations due to the complications in measuring the flow field using experimental techniques and difficulties in modelling turbulence. With advances in both fields, there has been a tremendous improvement in the design and operation of cyclone separators. A recent review by Ni *et al.* [2] discussed an increased interest in the improvement of designs of existing cyclone separators for industrial applications.

The flow field in the cyclone separator is three-dimensional and is usually represented using the cylindrical coordinate system ($r$, $\theta$, $z$). Preliminary experimental studies focussed on capturing the tangential component of velocity in the cyclone separator. The tangential component of velocity is responsible for the creation of the centrifugal forces on the particles, while the axial component of velocity helps in transportation of parti-

cles to the bin. The radial component velocity can be calculated using the continuity equation. In this analysis, the flow field is assumed to be symmetric about the z-axis. Dabir and Petty [3] used Laser Doppler Anemometry (LDA) to study the flow field in a hydrocyclone. LDA is a non-intrusive measurement device that produces accurate results of the tangential and axial velocity flow fields. Quian *et al.* [4] used LDA to measure the three components of velocity. Another technique commonly used for flow measurement is the Phase Doppler Particle Analyser (PDPA) which uses tracer particles to measure the flow fields. Dai *et al.* [5] used PDPA method to study particle motion and velocity fields. The primary diffiulty encountered in experimental studies is the measurement of the three velocity components. The usage of V3V (Volumetric 3-component Velocimetry) and PIV (Particle Image Velocimetry) techniques has helped to overcome this difficulty as highlighted by Wang *et al* [6]. Wang *et al* [6] used V3V and reconstructed the 2D images of the flow field to generate a 3D flow field. Liu *et al.* [7] was among the first who worked on PIV for hydrocyclone flows. They used Stereoscopic PIV to measure the 3 components of velocity and attempted to explain the backflow which occurs near the vortex finder.

Most of the preliminary numerical studies on the flow field in cyclone separators were based on the two-equation turbulence models namely the $k$-$\epsilon$ and the $k$-$\omega$ models, but results obtained from these simulations were not satisfactory as the models were not able to predict the anisotropic nature of Reynolds stresses in the flow. With an improvement in the computational facilities, more accurate results compared to two-equation models, were obtained. The use of second-moment closures such as Reynolds Stress Models (RSM) which solves for the six Reynolds stresses, increases the accuracy of the results. Large Eddy Simulations (LES) were employed to study the flow characteristics which led to more systematic results when compared to RSM. The results obtained from LES were found to be in good agreement with those obtained from experiments but were not entirely accurate. However, this method is computationally expensive when compared to the Reynolds Stress Model (RSM). The advantages of hybrid LES/RANS methods has been highlighted in the paper by Vengadesan and Nithiarasu [8]. Recent attempts by

Vakamalla and Mangadoddy [9] to study the flow characteristics using hybrid LES/RANS model (Detached Eddy Simulations (DES)) based on the Spalart-Allmaras RANS model were unsuccessful as the simulation results were not in good agreement with experimental measurements. Many studies on the numerical simulation of cyclone separators use Reynolds Stress Model (RSM) which requires lesser computational resources. Gao *et al.* [10] studied the effect of vorticity and vortex structures (Q criteria) on the performance of cyclone separators. They concluded that the study of vortex structures can be used to design cyclone separators and improve the flow stability in the cyclone separator. Saidi *et al.* [**?** ] investigated the flow field in a hydrocyclone using Large Eddy Simulations (LES) and examined the vortex structures using $\lambda_2$ criterion. They also studied the droplet motion in the hydrocyclone. Wang *et al.* [11] studied the effect of different inlet angles on the flow and particle tracks in the Hoekstra cyclone separator.

In recent times, hybrid turbulence models have been proposed as an alternative solution to LES and RSM. Hybrid turbulence models not only have the accuracy of LES, but also computationally less expensive. RSM usually tends to be numerically unstable due to the coupling of many equations which are avoided in hybrid models. Recent studies by many authors [12], [13], [14], [15] have shown the importance of studying the effect of hybrid turbulence models to various engineering problems. These studies help in better adaptation of hybrid turbulence models in the future, and also improve the accuracy of results for industrial problems.

The Lagrangian particle tracking requires various forces on the particles to be modelled. The forces that are considered for particle motion influence the accuracy of the predicted results. Hsieh and Rajamani [16] used only the drag and centrifugal forces, and concluded that there was good agreement between results of LDV (Laser Doppler Velocimetry) and simulations results for slurries in cyclone separators. Saffman and Magnus lift forces were used by Tofighian *et al.* [17] in addition to drag and gravitational forces. It was clear from their study that excluding the lift forces resulted in inaccurate erosion predictions for larger particles. Fluid turbulence causes fluctuations which affect particle motion and needs to be modelled when using the frozen-field approach. This is

done using dispersion models. There are two major dispersion models: Discrete Random Walk (DRW) and Continuous Random Walk (CRW). DRW models were initially used widely. CRW models were found to perform far better than the DRW models, especially in complex flows [18]. Hoekstra [1] used the CRW model along with LES as suggested by Pope [19] to obtain a good agreement with experiments for the collection efficiency curve. Sommerfeld's CRW model [20] was found to be effective in modelling particle dispersion in the study of Lipowsky and Sommerfeld [21].

Erosion becomes critical when large particles are involved. From previous studies, it can be seen that there are areas of concentrated high erosion. This leads to an increased cost of maintenance. There are many erosion models available in the literature (Finnie [22], Zhang [23], Neilson and Gilchrist [24] etc.). Standard elbow case is used to compare the performance of these models (Tofighian *et al.* [17] and Liu *et al.* [25]). These models had to be used in combination with restitution models like Grant and Tabakof's model [26], Forder model [27] and Jun and Tabakof's model [28] for betterment in results.

Some erosion studies have been carried out on different type of cyclone separators. Dizajyekan *et al.* [29] evaluated many parameters like centrifugal force and erosion in the Stairmand high-efficiency cyclone separator, and concluded that centrifugal forces increased with inlet velocity. Here, Oka's erosion model [30] was used, and it was concluded that the maximum erosion was at the inlet and conical regions. Dehdarinejad *et al.* [31] demonstrated that erosion was lower with non-uniform surface roughness when compared to the case with smooth walls. Karri *et al.* [32] investigated the influence of cyclone separator cylinder length and gas outlet velocity on the erosion of second-stage cyclone separators, and reported that vortex stabilizers could be very useful in reducing the erosion and maintaining the performance. Parvaz *et al.* [33] showed that when the height of the inner cone increased, erosion increased too. Sedrez *et al.* [34] compared the performance of Oka's model [30] and DNV model [35] for erosion with the experimental results for the cyclone separator. They concluded that Oka's model performed better at the top and the DNV model was better for predicting erosion in the cone. The former was the only work which compared the erosion both numerically and experimentally.

Various geometric modifications were developed in the cyclone separators for different goals. Yang *et al.* [36] used the RNG k-$\epsilon$ model and other particle models without dispersion modelling to conclude that helical triangular fins increased the separation efficiency of the device. A similar observation was reported on adding a 3D-printed guide vane to the device after using RNG k-$\epsilon$ model with simple particle models [37]. Fu *et al.* [38] used RSM and Dispersed Phase Modelling along with experiments to show that a slotted vortex finder increased the cut size of the equipment. Jihai *et al.* [39] used RSM turbulence model to affirm that their novel cyclone with an additional inner cylinder and an inlet at a lower height stabilized the flow field more. Due to the recirculating structures at the top part of the cyclone separator, the particles get trapped between these structures and the boundary layer leading to long particle residence at the top, forming ash rings [40] and causing more erosion [17]. Zhang *et al.* [41] used complex geometric modifications at various parts of the cyclone separators to reduce erosion. Extra inlets were used by Liu *et al.* [25] to reduce the erosion around the cone bottom. Both these recent works used a Rosin-Rammler particle distribution. An idea of avoiding sharp corners was used to lower the erosion in elbow pipes by Duarte *et al.* [42].

A large number of studies have been conducted on the cyclone separators using experimental and numerical methods. In this study we aim to use different turbulence models to study if hybrid turbulence models are able to provide accurate predictions of the hydrodynamics. Then a design modification is studied to reduce the erosion in cyclone separators.

### 2.2 Fins for Plate Heat Exchangers

Supercritical carbon dioxide (sCO2) is a potential working fluid for next-generation power conversion systems owing to its high density, low viscosity, and high thermal conductivity [43]. The sCO2 power cycle can achieve high thermal efficiency due to the reduction in compression work. In addition, the fluid characteristics of sCO2 make it possible to design compact and simple turbomachinery. Therefore, the rest of the sCO2 power cycle and the exchanger determine the compactness of the entire system [44]. One of the major

advantages of using PCHE is that the system can be scaled by increasing the number of plates used in the assembly.

The PCHE (printed circuit heat exchanger) is a compact heat exchanger which can provide high thermal-hydraulic performance. It has high heat transfer surface area density. The first enhancements to be tried on the PCHE are the zig-zag channels. The pressure drop was high when the flow went through the sharp bends, which led to the development of the sine-wave flow channels. This channel is obtained by rounding off the sharp bends in the zig-zag channel. The next iteration of the design to further improve the performance of PCHE, the sine wave channels were cut at the bends and were moved from the center to create the offset configuration. These fins had a blunt end which helps in promoting turbulence and enhancing heat transfer. The S-shaped fins were developed from the offset configuration which resulted in reduced pressure drop with almost identical heat transfer performance when compared to the zig-zag model [45]. Another type of enhancement for PCHE was developed by Kim *et al.* [46] They proposed a new discontinuous airfoil fin channel which resulted in a significant reduction in the pressure drop using numerical analysis.

The S-shaped fins were first introduced by Ngo *et al* [47]. They performed an experimental study on S-shaped fins for application in recuperator for carbon dioxide gas turbine cycle. They concluded that the new S-shaped fin heat exchanger design resulted in 3.3 times smaller volume and a 37% reduction in pressure drop requirement. Another study by Ngo *et al.* [48] compared the performance of the S-shaped fins with the zig-zag fins using ANSYS Fluent. They reported that the S-shaped fins provided 6-7 times lower pressure drop while maintaining similar heat transfer performance. Tsuzuki *et al.* [45] performed a parametric study on the S-shaped fins exploring the effect of the fin-angle, overlapping length, fin width, fin length and edge roundness. Rounded fins resulted in an increase of pressure drop by 30% when compared to no roundness. Tsuzuki *et al.* [49] in another study provided Nusselt number correlations for both the hot ($CO_2$) and cold sides (water). The correlations for the cold (water) side is for $100 < Re < 1500$ and the correlations for the hot side are valid from $1500 < Re < 15000$. Zhang *et al.* [50]

performed a structural assessment of the S-shaped fins in PCHE developed for gas-cooled fast reactors. Zhang *et al.* proposed using S-shaped fins with alloys which have high mechanical strength. Ding *et al.* [51] used the S-shaped fins to build a new adaptive flow path for regenerator heat exchangers. The new adaptive path resulted in a 69% reduction in pressure loss. Zeng *et al.* [52] conducted experiments in a microchannel heat exchanger assembly with S-shaped fins with water as the working fluid and provided Nusselt number and friction factor correlations.

Rao *et al.* [53] used the S-shaped fins as a starting point to a multi-objective optimization problem to develop a recuperator for supercritical carbon dioxide recompression Brayton cycle. Yin *et al.* [54] performed a comparative study on different fin patterns for a shell and plate particle supercritical $CO_2$ moving packed bed heat exchanger. S-shaped fins provided the best hydraulic performance among all the fin shapes considered. Kong *et al.* [55] compared the performance of different fin shapes for lead-s$CO_2$ intermediate heat exchanger (IHX) for lead-cooled fast reactor (LFR) and concluded that the S-shaped channel heat exchanger provides better power density than straight and airfoil channels. Kindra *et al.* [56] studied the feasibility of using S-shaped fin heat exchangers in the Oxy-Fuel Combustion power cycle. They were able to find optimum operating conditions for the S-shaped fin heat exchanger.

In this study we will be focussing on the thermal-hydraulic performance of the 3D twisted S-shaped fins and its comparison with S-shaped fins. The performance will be studied for various Reynolds number and Prandtl numbers. The change in the flow patterns due to the twist in the fins can be used to explain the reduction in the friction factor.

# Chapter 3

# Design of Cyclone Separator

## 3.1 Problem Statement

In this study, the focus is on the fluid flow characteristics in cyclone separators. We propose the use of hybrid LES/RANS models as opposed to the RSM and LES methods for capturing the flow features. The hybrid LES/RANS methods are computationally less expensive than the LES model and are also able to capture instantaneous flow features better than the predictions made by Reynolds Stress Model. The study is carried out for three different inlet velocities ($v$ = 8, 16.1, and 32 $m/s$) to understand the effect of inlet velocity on the flow features in the cyclone separator.

## 3.2 Numerical methods and turbulence modelling

The simulations in this study are carried out using the finite-volume based open-source software OpenFOAM-v1806 [57]. The turbulence models ($k$-$\omega$ SST, RSM LRR, LES WALE (Wall-Adapting Local Eddy-viscosity), $k$-$\omega$ SST based DES (Detached Eddy Simulation), $k$-$\omega$ SST based DDES (Delayed Detached Eddy Simulation) and $k$-$\omega$ SST based IDDES(Improved Delayed Detached Eddy Simulation)) implemented in OpenFOAM are discussed in the following sub-sections, and are followed by a case description and the boundary conditions used in the study.

### 3.2.1 Turbulence Modelling

#### RANS model

The RANS model used in this study is the two-equation $k-\omega$ SST model. In this model, we solve for the turbulent kinetic energy ($k$) and the specific rate of dissipation ($\omega$). The key difference between the regular $k-\omega$ and the $k-\omega$ SST model is that the SST model switches to $k-\epsilon$ from $k-\omega$ model in the free shear flow region. The model implemented in OpenFOAM is based on the study by Menter *et al.* [58].

The $k-\omega$ SST model is not sufficient to capture all the turbulent flow features, therefore results pertaining to the Reynolds Stress from the two-equation model is not discussed. One of the key phenomenon observed in the cyclone separator is the flow separation, and however using the $k-\omega$ SST model to predict the flow separation might result in erroneous results [59]. Only the mean velocity profiles from the model are used for comparison with the other turbulence models. It is not recommended to use two-equation models to solve for the turbulent flow field of cyclone separators. [9]

**Reynolds Stress Model (RSM)**

The Reynolds Stress Model (RSM) or the second-moment closure model focusses on solving six Reynolds stresses along with mean flow equations to solve the turbulent flow field. The model can predict anisotropy in the Reynolds stresses when compared to the two-equation RANS models. The RSM model used in OpenFOAM is the LRR (Launder-Reece-Rodi) model based on the study by Launder *et al.* [60]

The LRR model uses the linear pressure strain correlation. The LRR RSM model has been used to model cyclone separators in the study by Shalaby *et al.*[61] The flow in the cyclone separator exhibits streamline curvature and it is a key feature of the fluid flow in the cyclone separator. The LRR RSM model is deficient in predicting the mean rotational effects and streamline curvature. The shortcomings of the LRR RSM have been documented in the works [62], [63]. Previous studies have shown that the rapid pressure strain correlation is a limitation in rotating turbulent flows [64], [65], [66]. Quadratic pressure strain correction RSM models are available and can be used, but the scope of the paper is to investigate the applicability of hybrid LES/RANS models to cyclone separators, not to investigate in details the suitability of various RSM models.

**Large Eddy Simulations**

Large Eddy Simulations (LES) in this study is done using the WALE (Wall-Adapting Local Eddy-viscosity) model. This model is chosen based on the results accomplished by Poncet *et al.* [67] where they have concluded that the WALE model is computationally

less expensive when compared to other LES models. This ensures that we are comparing the computationally least expensive LES model to hybrid LES/RANS models. The WALE model as described by Nicoud and Ducros [68] is used in the simulations.

$$\frac{\partial \tilde{u_i}}{\partial t} + \frac{\partial \tilde{u_i}\tilde{u_j}}{\partial x_j} = \frac{-1}{\rho}\frac{\partial p}{\partial x_i} + \nu\frac{\partial^2 \tilde{u_i}}{\partial x_j^2} - \frac{\partial \tau_{ijSGS}}{\partial x_j} \tag{3.1}$$

$$\tau_{ijSGS} = \widetilde{u_i u_j} - \tilde{u_i}\tilde{u_j} \tag{3.2}$$

$$\mu_t = \rho\Delta_s^2 \frac{\left(S_{ij}^d S_{ij}^d\right)^{3/2}}{\left(\tilde{S}_{ij}\tilde{S}_{ij}\right)^{5/2} + \left(S_{ij}^d S_{ij}^d\right)^{5/4}} \tag{3.3}$$

$$\Delta_s = C_w V^{1/3} \tag{3.4}$$

$$S_{ij}^d = \frac{1}{2}\left(\tilde{g}_{ij}^2 + \tilde{g}_{ji}^2\right) - \frac{1}{3}\delta_{ij}\overline{g}_{kk}^2 \tag{3.5}$$

$$\tilde{g}_{ij} = \frac{\partial \tilde{u_i}}{\partial x_j} \tag{3.6}$$

$$\tilde{g}_{ij}^2 = \tilde{g}_{ik}\tilde{g}_{kj} \tag{3.7}$$

In the above equations $u_i$ is the fluid velocity and $\tilde{u_i}$ is the filtered velocity component. Coefficients used in the simulation are: $C_k = 0.094, C_e = 1.048, C_w = 0.325$.

### $k-\omega$ SST based hybrid models

The hybrid LES/RANS models used in this study are $k-\omega$ SST based models. These models use equations to solve for turbulent kinetic energy ($k$) and specific rate of dissipation ($\omega$). The two quantities are then used to calculate turbulent viscosity. Switching between the $k-\epsilon$ and $k-\omega$ models as a part of the $k-\omega$ SST model is also retained in the hybrid model. Detached Eddy Simulation (DES) model implemented here is based on the study by Strelets [69]. The Delayed Detached Eddy Simulation (DDES) and Improved Delayed Detached Eddy Simulation (IDDES) are based on a study by Gritskevich *et al* [70].

$$\frac{\partial \rho k}{\partial t} = \nabla \cdot (\rho D_k \nabla k) + \min\left(\rho G, (c_1 \beta^*)\, \rho k \omega\right) - \frac{2}{3}\rho k\, (\nabla \cdot u) - \rho \frac{k^{1.5}}{\tilde{d}} + S_k \tag{3.8}$$

$$\frac{\partial \rho \omega}{\partial t} = \nabla \cdot (\rho D_\omega \nabla \omega) + \rho \gamma \frac{G}{\nu} - \frac{2}{3}\rho \gamma \omega\, (\nabla \cdot u) - \rho \beta \omega^2 - \rho\, (F_1 - 1)\, CD_{k\omega} + S_\omega \tag{3.9}$$

$$\tilde{d} = \min\left(C_{DES}\Delta, \frac{\sqrt{k}}{\beta^* \omega}\right) \tag{3.10}$$

$$\nu_t = a_1 \frac{k}{\max\left(a_1 \omega, b_1 F_{23} \mathbf{S}\right)} \tag{3.11}$$

where $\alpha_{k1} = 0.85, \quad \alpha_{k2} = 1, \quad \alpha_{\omega 1} = 0.5, \quad \alpha_{\omega 2} = 0.856, \quad \beta_1 = 0.075, \quad \beta_2 = 0.0828,$ $\gamma_1 = 5/9, \quad \gamma_2 = 0.44, \quad \beta^* = 0.09, \quad a_1 = 0.31, \quad b_1 = 1, \quad c_1 = 10, \quad CDES_{k\epsilon} = 0.6,$ $CDES_{k\omega} = 0.82$

In the hybrid LES/RANS models, LES is solved in some regions and the RANS equations are solved in the other regions. Many different hybrid models have been proposed and they differ in the way the model switches between the LES and RANS region. Some models employ prefixed switching between the LES and RANS regions also, called as zonal models [71]. The models which facilitate a smooth transition (no prefixed distance) from RANS region to LES region are called non-zonal models [71]. In this study, non-zonal models (smooth transition) are used and during the simulation the transition is based on the equations 3.12 - 3.14, respectively for DES, DDES and IDDES. These equations are based on Strelets [69] and Gritskevich *et al* [70]. The switching between the models is based on the length scales calculated for the models. $L_{LES}$ corresponds to the length scale used in LES and $L_{RANS}$ is the length scale used for the RANS model. For the DDES and IDDES models, the length scales are multiplied by an empirical delay function $f_d$ to shift the switch between the models.

$$\tilde{d}_{DES} = \min\left(\Psi C_{DES}\Delta, y\right) \tag{3.12}$$

$$\tilde{d}_{DDES} = \max\left[L_{R\Delta S} - f_d, \max\left(L_{RANS} - L_{LES}, 0\right)\right] \tag{3.13}$$

$$\tilde{d}_{IDDES} = \max\left(f_d L_{RANS} + (1 - f_d)\, L_{LES}, 1e-6\right) \tag{3.14}$$

The variables in the above equations are defined below:

$$L_{RANS} = y \tag{3.15}$$

$$L_{LES} = \Psi C_{DES} \Delta \tag{3.16}$$

$$f_d = 1 - \tanh\left[\left(C_{d1} r_d\right)^{C_{d2}}\right] \tag{3.17}$$

$$\Psi^2 = \min\left[10^2, \frac{1 - \frac{1-C_{\mathrm{b1}}}{C_{\mathrm{w1}\kappa} f_w^*}\left[f_{t2} + (1 - f_{t2})\, f_{\mathrm{v2}}\right]}{f_{\mathrm{v1}} \max\left(10^{-10}, 1 - f_{t2}\right)}\right] \tag{3.18}$$

$$r_d = \min\left(\frac{\nu_{eff}}{|\nabla \mathbf{u}| \kappa^2 y^2}, 10\right) \tag{3.19}$$

where $\nu_{eff}$ is the effective viscosity, $\kappa$ is a constant of value 0.41 and $y$ is the distance from the nearest wall. The other constants are $\sigma_{\nu_t} = 2/3$, $C_{b1} = 0.1355$, $C_{b2} = 0.622$, $C_{w1} = \frac{C_{b1}}{\kappa^2} + \frac{1+C_{b2}}{\sigma_{\nu_t}}$, $C_{w2} = 0.3$, $C_{w3} = 2$, $C_{v1} = 7.1$, $C_s = 0.3$, $C_{DES} = 0.65$, $C_k = 0.07$, $C_{t3} = 1.2$, $C_{t4} = 0.5$, $f_w^* = 0.424$.

### 3.2.2 Case Description and Boundary Conditions

The geometry of the cyclone separator used in this study is shown in Fig. 3.1. The dimensions of the cyclone separator are non-dimensionalised using the diameter of the cylindrical section (D = 290 mm). The results are discussed at three planes (z = 0.75D, 2D and 2.5D as shown in Fig. 3.1) as done in the experimental work by Hoekstra [1]. Uniform velocity is provided at the inlet. Pressure is kept constant, and all other scalars are given zero gradient boundary condition at the outlets. Standard wall functions are used for turbulent quantities in all the turbulent models. Air, at constant density of 1.2 $kg/m^3$ and kinematic viscosity of $1.57 \times 10^{-5}$ $m^2/s$ is used as the working fluid. Time step used in the simulations is $5 \times 10^{-6}$, which ensures that it is smaller than the residence time for the cyclone separator. Courant number using the time step mentioned is between 0.2-0.3. Transient simulations are carried out with pisoFOAM solver in OpenFOAM. All the mean flow quantities in this study are obtained by averaging after attaining the stationary state of the turbulent flow in the cyclone separator.

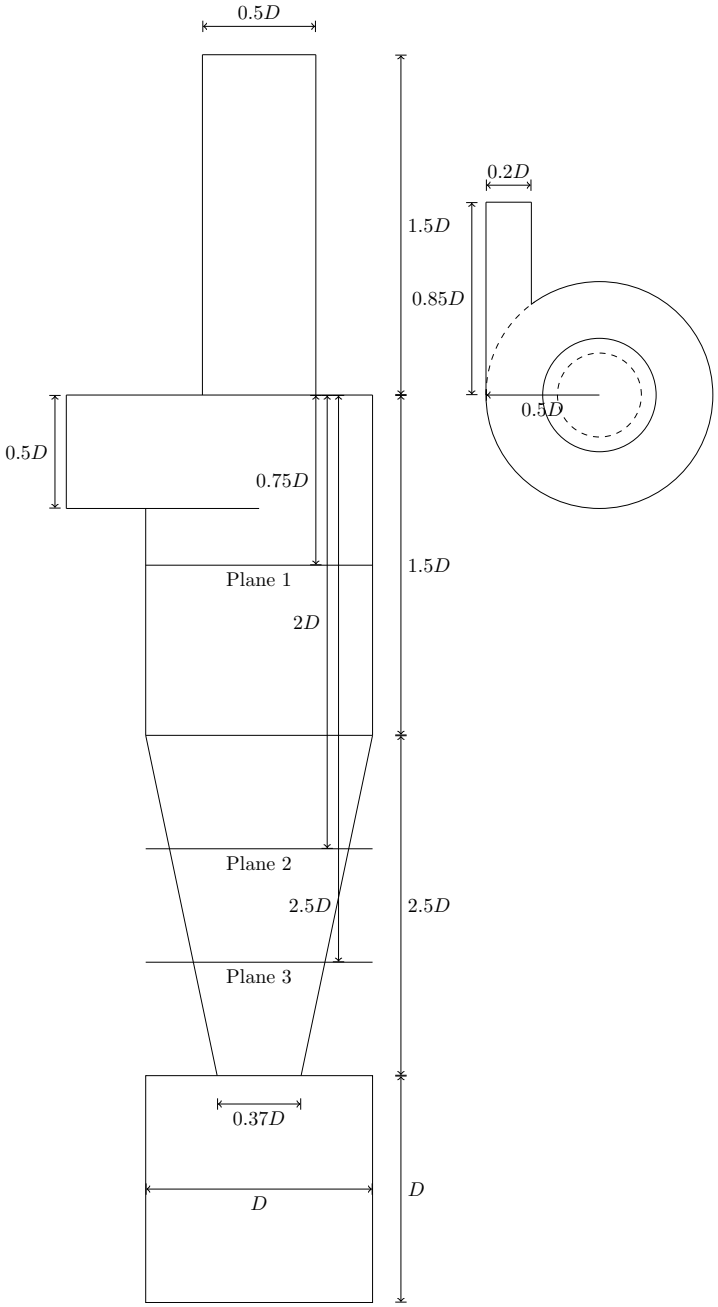


Figure 3.1: Solid particle cyclone separator

### 3.2.3 Mesh independence study

The simulations for mesh independence study are carried out for inlet velocity of 16.1 $m/s$ and compared with the experimental results of Hoekstra [1]. Three mesh sizes (Mesh - 1, 2 and 3) in Table 3.1 are used for the hybrid models, and meshes 3 and 4 are used for the LES WALE model. Smaller sized meshes are not used for LES as they will result in erroneous results since the grid sizes are not enough to resolve the flow field. The

most optimum mesh is selected by looking at the tangential velocity prediction by the different meshes. The tangential velocity for different meshes is shown in Fig. 3.2 for the three different hybrid LES/RANS models and the LES model. Fig. 3.2 demonstrates that mesh 2 is sufficient to capture the velocity profile in the cyclone separator for hybrid models. Mesh 3 also predicts accurate results for the hybrid models but has almost twice the number of cells as compared to mesh 2. The difference between the velocity values for the two meshes is less, as shown in the magnified view. Therefore for faster computation without compromising the quality of results, mesh 2 is used. Mesh 2 is also used for the Reynolds stress model and the two-equation $k-\omega$ SST model. For LES, mesh 3 produces results as comparable to the experimental results, whereas mesh 4 over-predicts the velocity values.

Table 3.1: Mesh independence test details

| Mesh number | Number of elements |
|---|---|
| Mesh 1 | 188756 |
| Mesh 2 | 312441 |
| Mesh 3 | 499194 |
| Mesh 4 | 992162 |

## 3.3 Results and Discussion

The results discussed in this paper are related to the fluid flow characteristics of cyclone separators. Accurate fluid flow characteristics are essential to understand the multiphase nature of the cyclone separator. Firstly, the effect of different turbulence models is discussed, and the most accurate model is chosen to discuss other results. Velocity profiles and vorticity profiles are then discussed to understand the effect of different inlet velocities.

### 3.3.1 Turbulence modelling

In this current study, three different hybrid LES/RANS turbulence models ($k-\omega$ SST based DES, DDES, and IDDES) are considered as an alternative to the RSM and LES models. The hybrid models differ in the region where the model switches between the

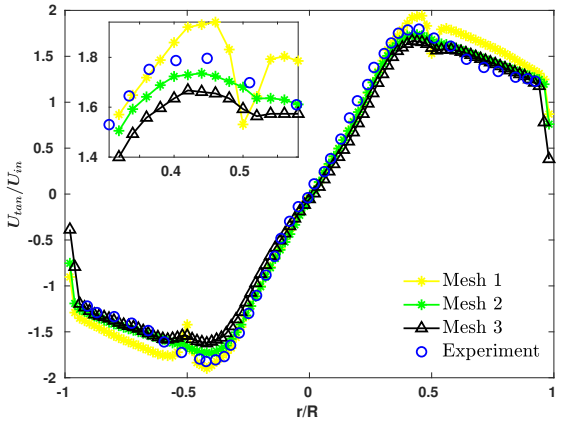


(a) DES $k-\omega$ model

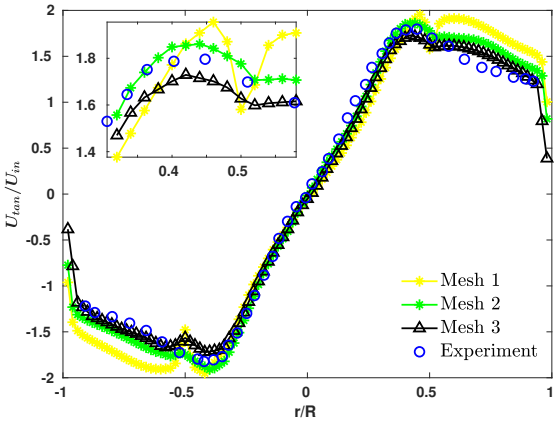


(b) DDES $k-\omega$ model

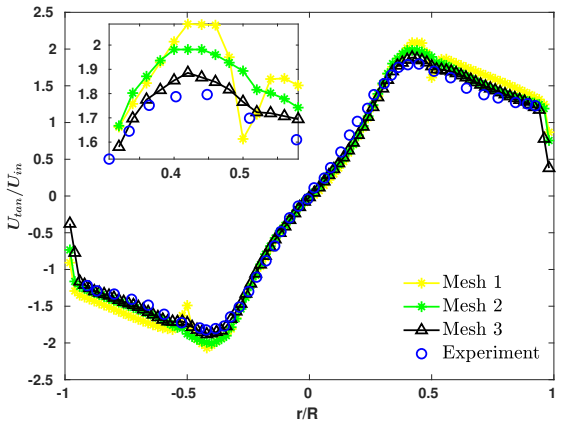


(c) IDDES $k-\omega$ model

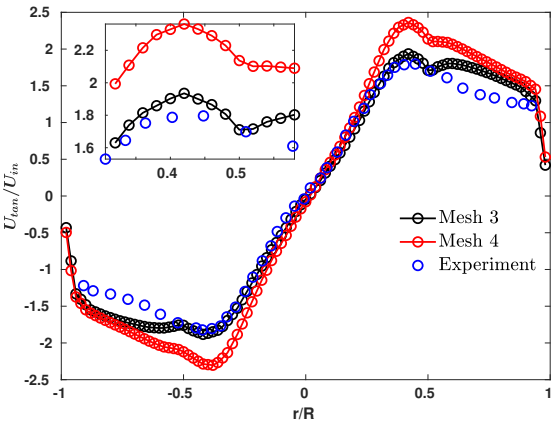


(d) LES WALE model

Figure 3.2: Mesh independence study for hybrid models (Experiment: Hoekstra [1])

RANS and LES model regions. The velocity profiles and turbulence parameters are discussed for the different models.

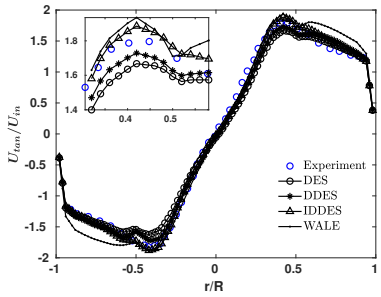


(a) Plane 1

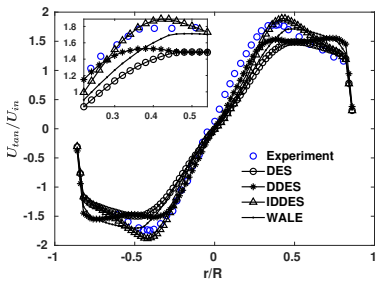


(b) Plane 2

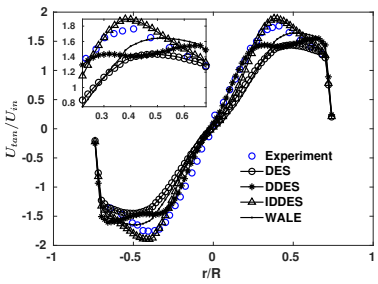


(c) Plane 3

Figure 3.3: Tangential velocity profiles at three different planes for different turbulence models (Experiment: Hoekstra [1])

To compare the performance of the different hybrid models, the tangential and axial

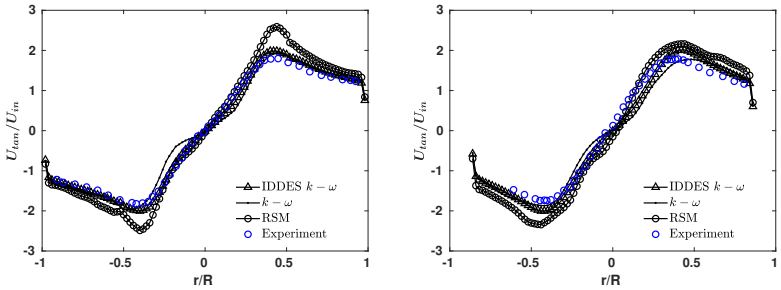


(a) Plane 1 (b) Plane 2

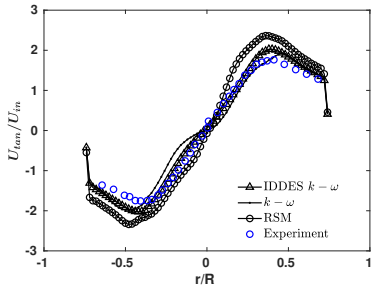


(c) Plane 3

Figure 3.4: Comparison of turbulence models (Experiment: Hoekstra [1])

component of velocities for the three different planes (plane 1, plane 2, and plane 3) are plotted in Fig. 3.3 and compared with the experimental values. The velocity is normalised using the inlet velocity. The region near the peak velocity is zoomed in to show the differences in the models' prediction. From Figure 3.3, it can be inferred that $k-\omega$ SST based IDDES hybrid model performs better than the $k-\omega$ SST based DES and DDES hybrid models. When comparing the results of the hybrid LES/RANS and the LES model, we see that the IDDES model results are more accurate than the LES WALE model for reduced mesh size in the near wall region and the central region of the cyclone separator. All the models (hybrid LES/RANS and LES) are able to predict the tangential component of the velocity profile throughout the width of the cyclone separator at plane 1 with reasonable accuracy. However, as we move further down the cyclone separator to plane 2 and plane 3, there are differences in the tangential component of velocity profile for different models. The IDDES hybrid model is able to predict the velocity profile remarkably good at various locations in the cyclone separator. Fig. 3.4 shows the tangential velocity profiles at three different planes comparing the RANS $(k-\omega)$ SST, RSM and $k-\omega$ SST based IDDES models. We can see that the RSM model overpredicts

the velocity at all the planes. The $k-\omega$ SST model is able to predict the peak value, but is not able to predict the velocity around the centre region ($|r/R| < 0.2$) where it underpredicts the velocity. This is because the two-equation $k-\omega$ SST model is not able to capture the flow separation effects in the flow [72],[73]. When the hybrid turbulence models based on the $k-\omega$ SST model are used, LES models are used in the regions where flow separation occurs and this improves the velocity predictions made by the hybrid turbulence models in the core region ($|r/R| < 0.2$).

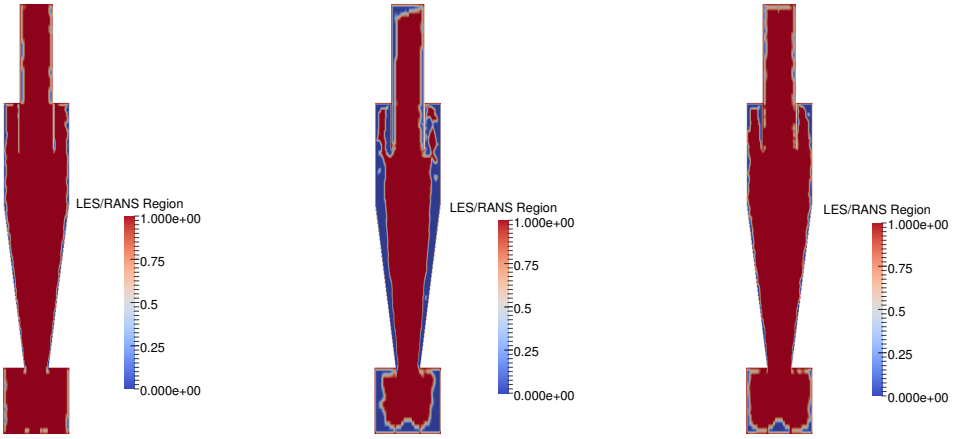


(a) DES (b) DDES (c) IDDES

Figure 3.5: The LES (red) and RANS (blue) regions for the different hybrid models

The switching between the LES and RANS region is demonstrated in Fig. 3.5. This figure is obtained by plotting the distance $\tilde{d}$ defined for each hybrid LES/RANS model as defined in equation 3.10. The section for plotting is taken at the center of the cyclone separator perpendicular to the inlet of the cyclone along the y-axis. The red region corresponds to the LES model, while the blue region corresponds to the RANS model. The RANS region is mainly concentrated near the wall region while the LES region is spread over the entire volume. The DES hybrid model has the highest concentration of the LES region when compared with other hybrid models, but underpredicts the velocity at planes 2 & 3. The IDDES model has a lower concentration of LES region when compared to DES but is able to better approximate the velocity profiles at all planes. The IDDES hybrid model has a larger LES region than the DDES model, which improves its prediction of velocity profiles when compared to the latter. Therefore appropriate

region of LES and RANS is required to obtain accurate results.

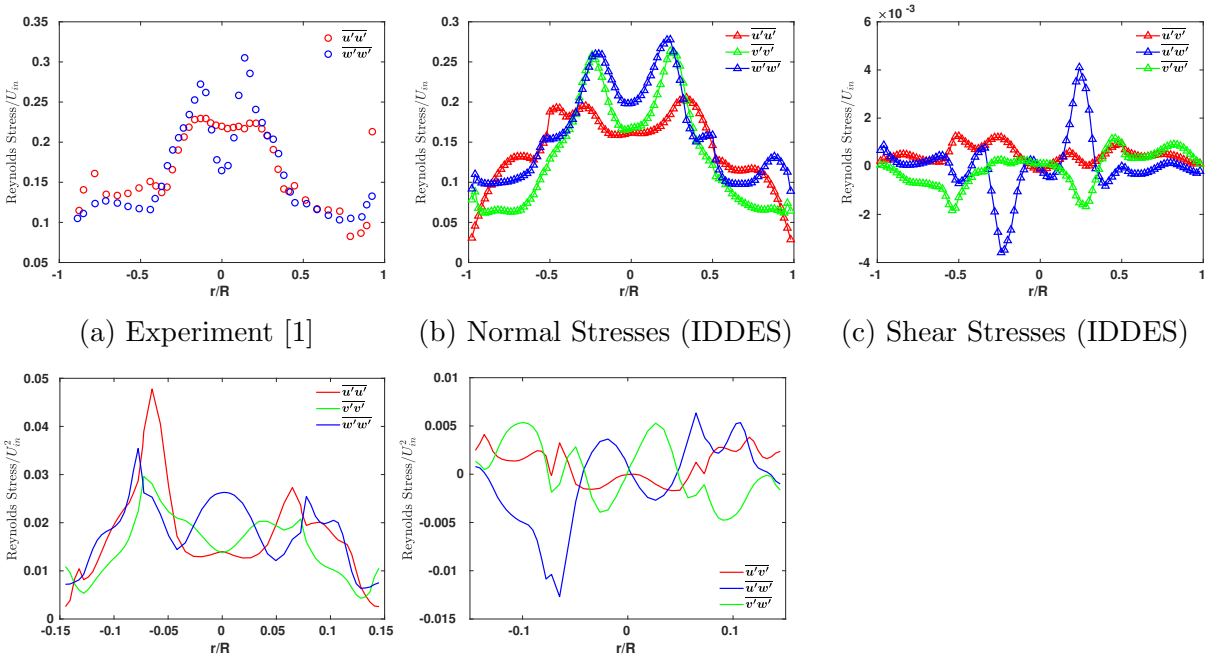


(a) Experiment [1] (b) Normal Stresses (IDDES) (c) Shear Stresses (IDDES)

(d) Normal Stresses (RSM) (e) Shear Stresses (RSM)

Figure 3.6: $u'_{RMS}$ and $v'_{RMS}$ from experimental data and Reynolds stress profiles at plane 1 from the IDDES and RSM model

Reynolds stresses play a role in modelling the motion of particles. When particle tracking simulations are done for the cyclone separator, dispersion modelling is required to model the turbulent fluctuations seen by the particle. The results provided here can aid in developing a better model for turbulent fluctuations seen by the particle in a rotating turbulent flow. The Reynolds stresses are scaled by the square of the inlet velocity to facilitate a comparison with the experimental results available. The hybrid turbulence models are able to capture anisotropy in the turbulence field better than RSM values as seen in Fig. 3.6. The Reynolds stress values are plotted for $v = 16.1\ m/s$ in Fig. 3.6. In the figure the values of the Reynolds stress are compared to the RMS values of the the fluctuating velocity data found in the experimental study and the RSM model results. The trend of the Reynolds stress profile from the hybrid models is similar to the experimental data published and are able to capture the location of the peak values of Reynolds stress near the central region of the cyclone separator. The Reynolds stresses $\overline{u'v'}$, $\overline{u'w'}$ and $\overline{v'w'}$ have not been reported from experimental studies. The profiles for these Reynolds stresses are provided in this study.

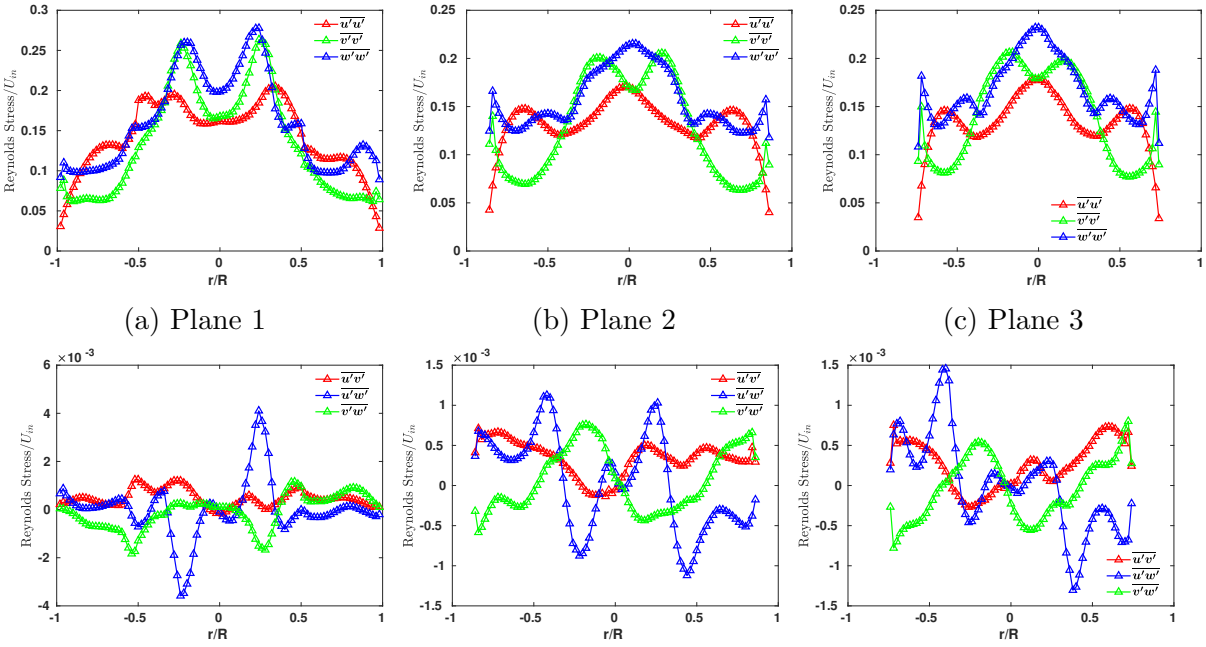


(a) Plane 1 (b) Plane 2 (c) Plane 3

(d) Plane 1 (e) Plane 2 (f) Plane 3

Figure 3.7: Reynolds stress profiles for $v = 16.1\ m/s$ at different planes of the cyclone separator

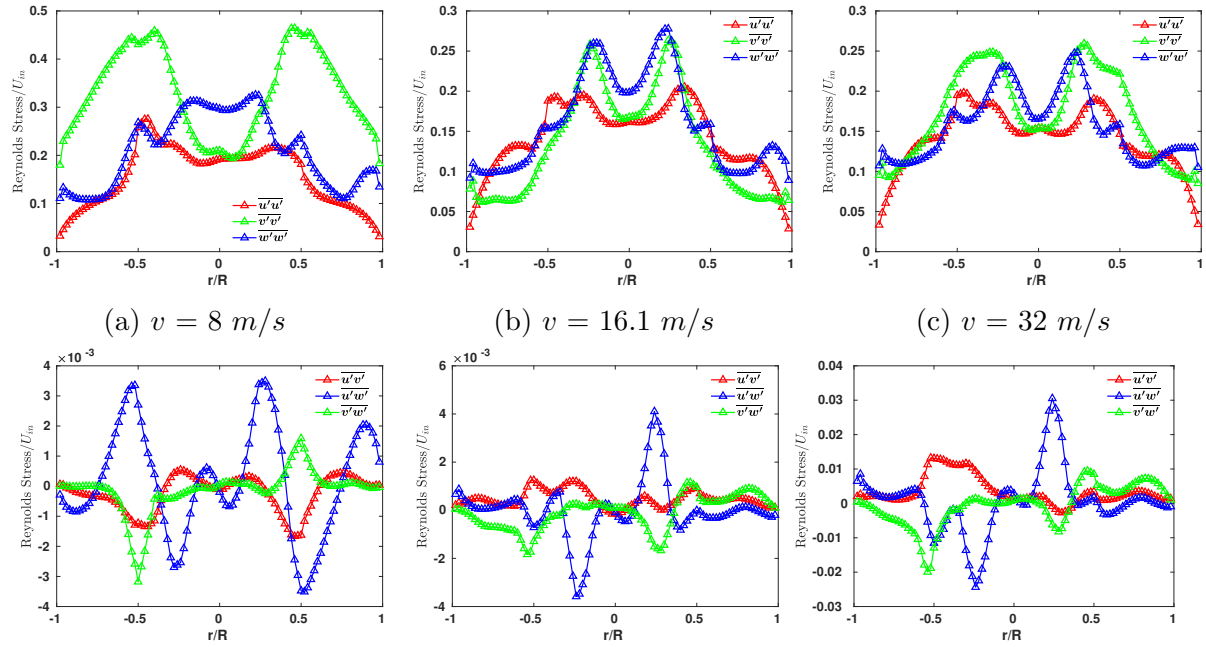


(a) $v = 8\ m/s$ (b) $v = 16.1\ m/s$ (c) $v = 32\ m/s$

(d) $v = 8\ m/s$ (e) $v = 16.1\ m/s$ (f) $v = 32\ m/s$

Figure 3.8: Reynolds stress profiles for different velocities at Plane 1 of the cyclone separator

The Reynolds stresses at different planes are shown in Fig.3.7. As we move down the cyclone separator, undulations in the Reynolds stress increase due to a decrease in the

cross-sectional area. This affects the velocity fluctuations, which act on the particles due to high variation in the stress values. The effect of inlet velocity on Reynolds stresses is shown in Fig. 3.8. The interesting result observed here is that at lower inlet velocities, the value of $\overline{v'v'}$ is higher in magnitude than the other Reynolds stresses, which are qualitatively similar to the one in experimental results.

In the annular region ($|r/R| > 0.9$) of the cyclone separator, large velocity gradients are present near the wall region which leads to higher predictions of the Reynolds Stress. The velocity gradients increase as we move down in the cyclone separator, which leads to a higher production of Reynolds stress. Due to the presence of the processing vortex core at the centre ($|r/R| < 0.2$), the Reynolds stress decreases [74], [75]. The RSM model is able to capture the anisotropy in the flow, but is not able to give a good prediction of the Reynolds stress. The models are not able to capture the precessing vertex core effects. The secondary peaks observed in the Reynolds stress are present near the peak values of the velocity profile.

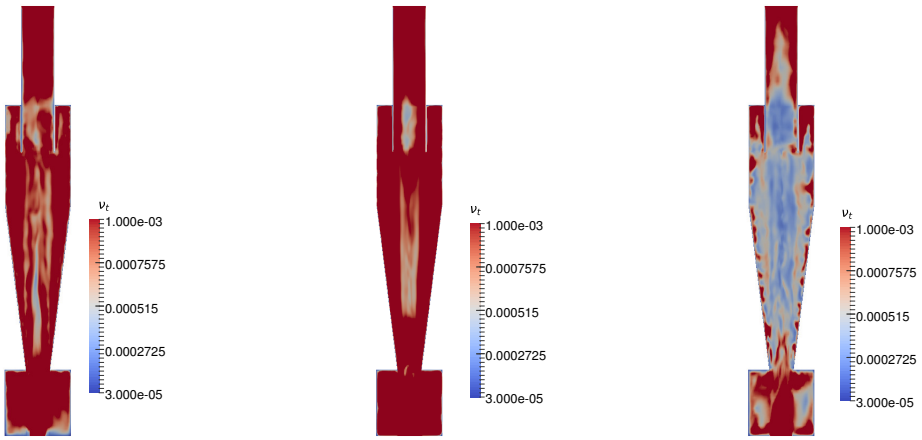


(a) DES (b) DDES (c) IDDES

Figure 3.9: Turbulent viscosity ($\nu_t$) for three different hybrid models

Reynolds stresses are modelled using turbulent viscosity and the gradients of the velocity. Overprediction of turbulent viscosity leads to overprediction in the turbulent quantities. Therefore correctly predicting the value of turbulent viscosity is important for obtaining accurate turbulent flow features. The turbulent viscosity is plotted for different hybrid models in Fig. 3.9. The IDDES model has a low turbulent viscosity in the central

region when compared to the other hybrid models, which could be the reason for higher accuracy in the velocity and the turbulent quantities.

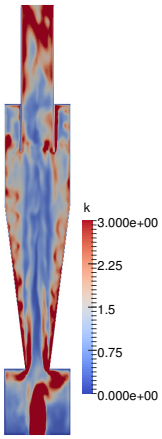


(a) DES, $v = 16.1\ m/s$

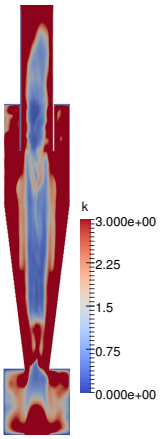


(b) DDES, $v = 16.1\ m/s$

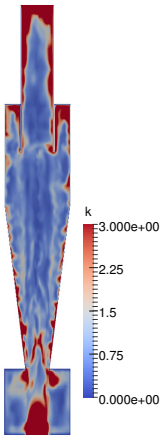


(c) IDDES, $v = 16.1\ m/s$

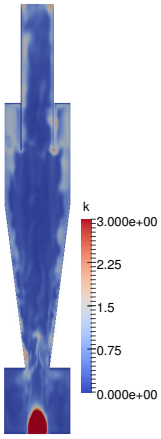


(d) IDDES, $v = 8\ m/s$

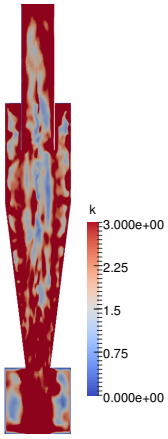


(e) IDDES, $v = 32\ m/s$

Figure 3.10: Turbulent kinetic energy ($k$) for three different hybrid models and different inlet velocities

Figs. 3.10 a-c shows the turbulent kinetic energy for the three different hybrid models, and also the effect of inlet velocity (Figs. 3.10 d-e) on turbulent kinetic energy distribution in the cyclone separator. There is a significant difference in the distribution of TKE between different hybrid LES/RANS models. The DDES model predicts a higher TKE value near the walls, which is not accurate. As the inlet velocity is increased, we find that the TKE also increases proportionally. The TKE predominantly increases in the region where vorticity magnitude increases.

### 3.3.2 Computational Time

One of the major advantage of using the hybrid LES/RANS models over the LES model is its reduction in computational time. The computational time is calculated for all the models after reaching stationary state for the flow in the cyclone separator. Simulations are run for 20000 iterations on an Intel i7-7700 3.60 GHz processor with 4 cores for comparison of computational time (see Table 3.2).

Computational time required for the hybrid models are comparable to each other. Difference between the models arises because of different switching formulas between LES and RANS regions for the hybrid models. There is a 55% reduction in computational time for the $k-\omega$ SST based IDDES model compared to the LES WALE model. The reduction in simulation time will also be reflected when we study the multiphase flow in the cyclone separator, as these simulations take up a lot of time.

Table 3.2: Computational time for various models

| Model | Computational time (s) |
|---|---|
| $k-\omega$ SST | 12931 |
| Reynolds Stress Model LRR | 16201 |
| $k-\omega$ SST based DES | 14326 |
| $k-\omega$ SST based DDES | 14359 |
| $k-\omega$ SST based IDDES | 14878 |
| LES WALE | 33700 |

### 3.3.3 Velocity distributions

The flow distribution in cyclone separators is three-dimensional and turbulent. The profiles for velocity are obtained after statistical stationarity is achieved in the flow field of the cyclone separator. After statistical stationarity, the profiles are averaged to obtain mean velocity profiles.

The tangential and axial components of velocity profiles for $k-\omega$ SST based IDDES model are shown in Fig. 3.11. The model is able to predict the correct trend of the tangential and axial velocity profile at the three different planes. It is also able to capture the downward trend of axial velocity at the center of the cyclone separator. The

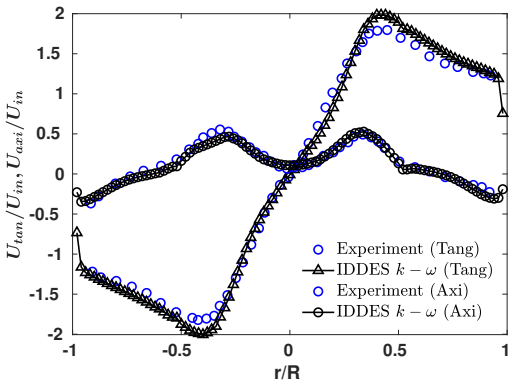


(a) Plane 1

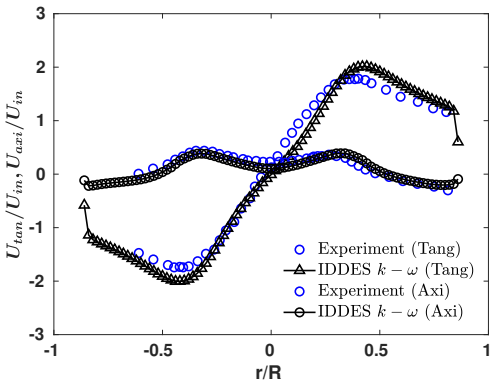


(b) Plane 2

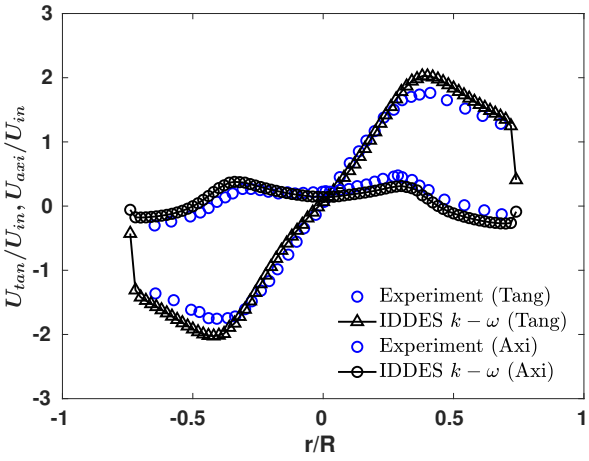


(c) Plane 3

Figure 3.11: Tangential (Tang) and axial (Axi) velocity profiles at three different planes (Experiment: Hoekstra [1])

magnitude of peak value in the tangential component of velocity is not captured, but the location of the peak value is predicted accurately by the models. The peak value of the tangential component of velocity increases as we go from plane 1 to plane 3. This is due to the decrease in the cross-sectional area in the conical region of the cyclone separator.

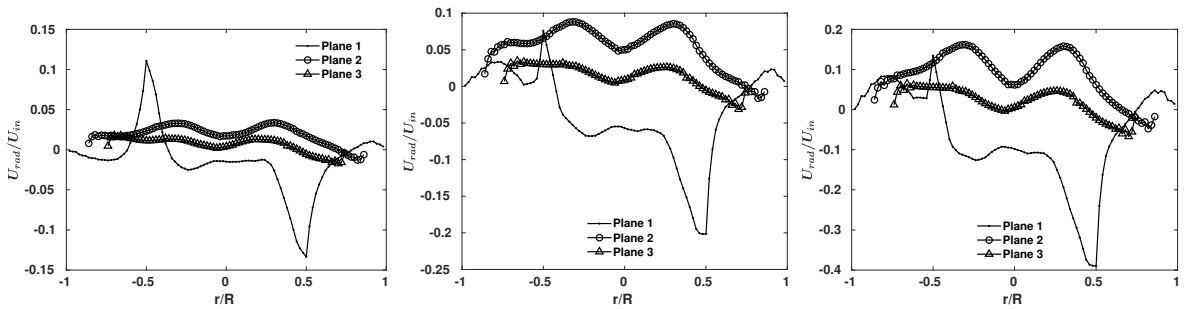


(a) $v = 8\ m/s$ (b) $v = 16.1\ m/s$ (c) $v = 32\ m/s$

Figure 3.12: Radial velocity profiles at three different planes for different inlet velocities

The radial component of the velocity profile for the cyclone separator is shown in Fig. 3.12. It is challenging to obtain this velocity measurement in experimental studies and is usually obtained from the continuity equation using the tangential and axial velocity. The asymmetric pattern in the radial component of the velocity profile in planes 2 and 3 shows that flow is not symmetric about the vertical axis. Therefore simulating with axisymmetric conditions as reported in most of the literature will lead to errors in the calculation of the velocity profiles and turbulent quantities.

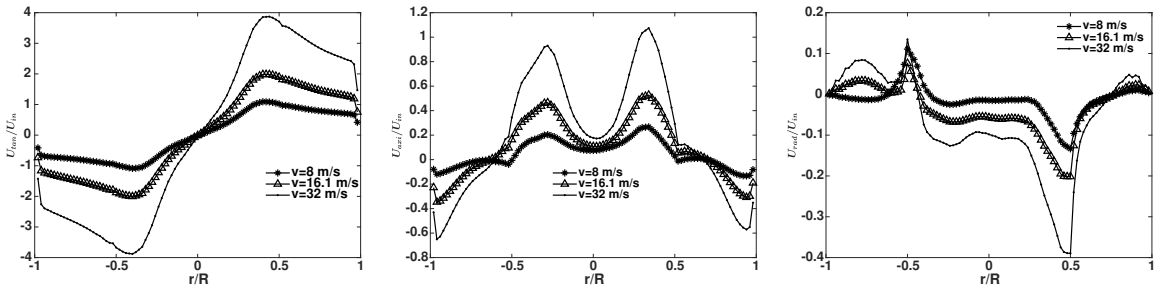


(a) Tangential (b) Axial (c) Radial

Figure 3.13: Velocity profiles at plane 1 for different inlet velocities

The effect of inlet velocity on the velocity profiles is shown in Fig. 3.13. The magnitude of the peak velocity for all the velocity components increases as the inlet velocity is increased from v=8 m/s to v=32 m/s. The position of the peak velocity does not, however, change with the change in the inlet velocity. This shows that the vortex formed at the central region does not change size as we increase or decrease the inlet velocity.

Some of the fluid from the inlet directly escapes through the vortex finder. This flow is called the shortcut flow. The IDDES model is able to capture the shortcut flow from the inlet through the vortex finder as shown in Fig. 3.14. A red circle is marked near the vortex finder to show the shortcut flow in the cyclone separator. The amount of leakage fluid does not vary much when the inlet velocity is changed.

### 3.3.4 Vorticity distribution

Insights on energy distributions in the cyclone separator can be obtained from the study of vorticity. The magnitude of vorticity is plotted at three different planes for three

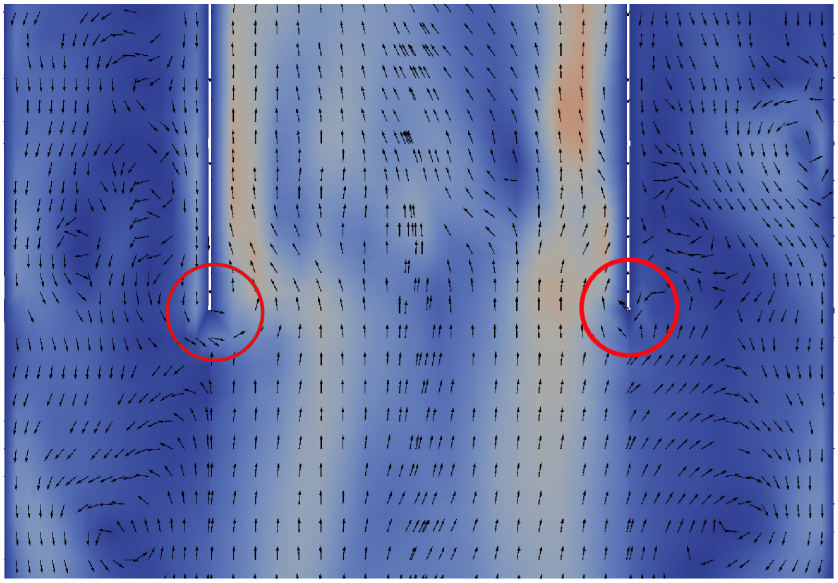

Figure 3.14: Image showing the leakage of fluid through the vortex finder at inlet velocity of 16.1 $m/s$

different inlet velocities in Fig. 3.15. The increase in the vorticity magnitude near the wall (r/R=1 and -1) shows that a large quantity of energy is lost to the wall. The vorticity is maximum, where there exists a steep gradient in the tangential and axial velocity. The vorticity reduces as we move towards the wall. Near the wall region, the vorticity peaks again and is maximum around the region closest to the wall. This is where the majority of the energy in the cyclone separator is lost. A secondary peak is also visible at all inlet velocities at plane 1, and this is due to the vortices formed at the vortex finder region due to shortcut flow. The peak of the vorticity in the central region decreases as we move down to planes 2 and 3. It is to be observed that the peak is not located at the geometric center. The increase in inlet velocity increases the strength of the vorticity.

The vortices also influence the motion of particles, as some particles can get trapped in vortices and be transported along with it. The instantaneous streamline patterns for different inlet velocities are shown in Fig. 3.16. The streamlines are plotted in a section perpendicular to the y-axis for non-dimensional time of $125T$ ($T = D/u$). From the figure, it is evident that the vorticity strength increases as the inlet velocity is increased. The vortices are concentrated primarily near the wall region, where the vorticity magnitude is high, as seen in the line plot of vorticity in Fig. 3.15. The vortices seem to detach from the wall due to swirl of the fluid. Some vortices are also concentrated near the vortex

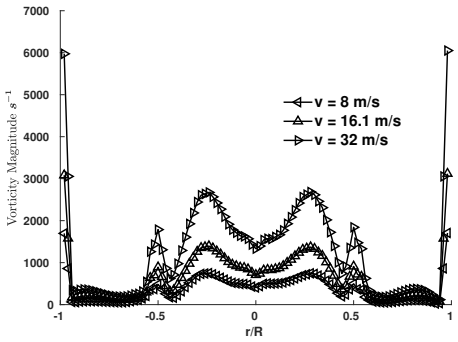


(a) Plane 1

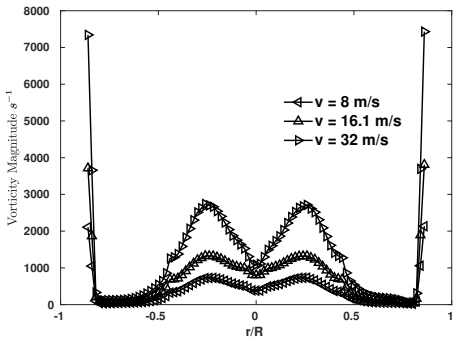


(b) Plane 2

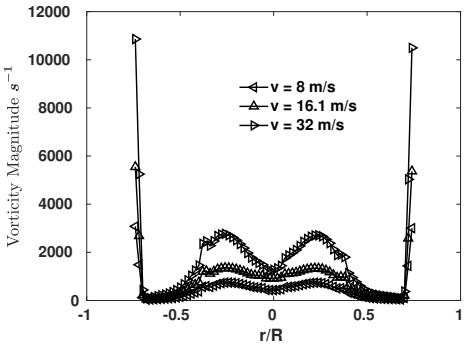


(c) Plane 3

Figure 3.15: Vorticity profiles at three different planes

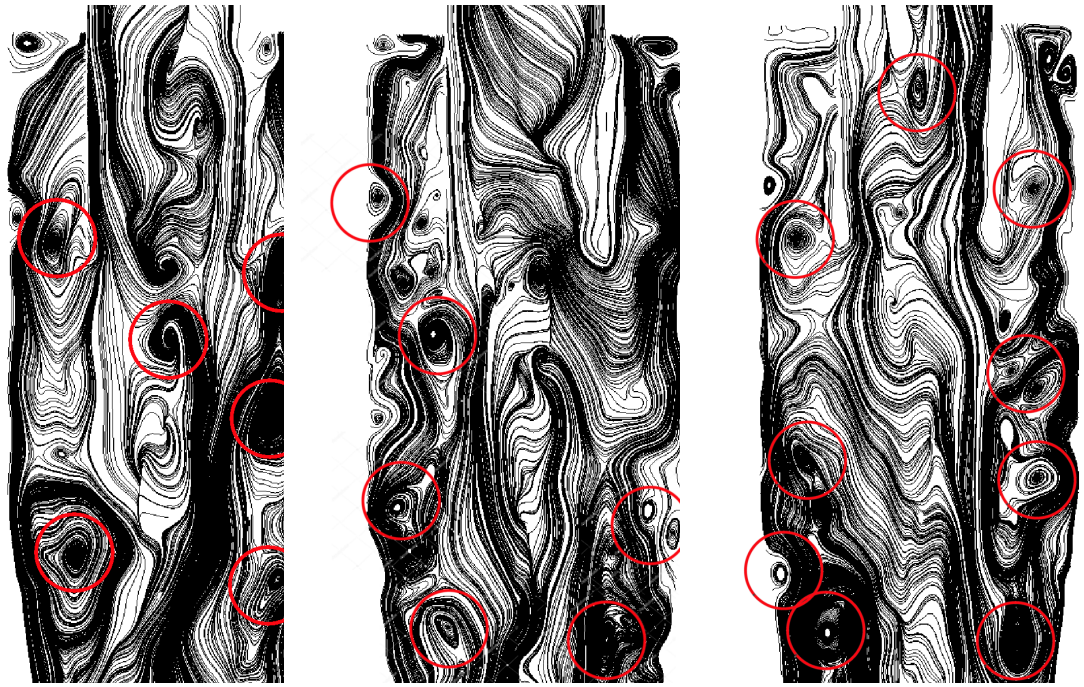

(a) $v = 8\ m/s$ (b) $v = 16.1\ m/s$ (c) $v = 32\ m/s$

Figure 3.16: Streamline patterns

finder region. This is because shortcut flow that occurs in this region.

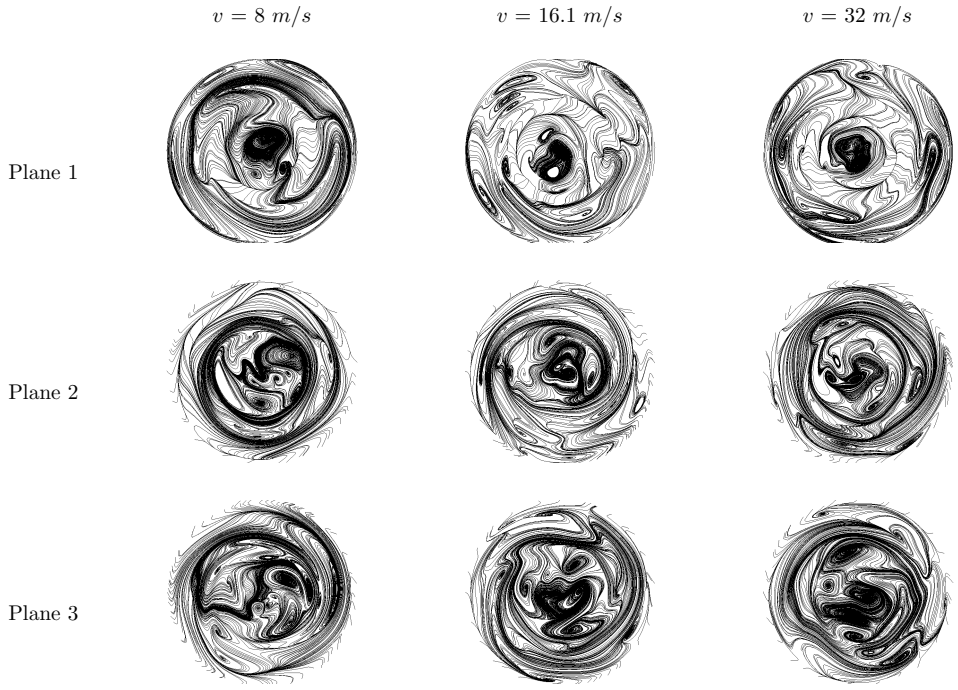


Figure 3.17: Vorticity line patterns at various z cross-sections

The vorticity lines are plotted for the three different planes of the cyclone separator in Fig. 3.17. As we move down the cyclone separator, the vorticity strength increases due to a decrease in the cross-sectional area, which further increases the mixing of the fluid. Vortices are mainly concentrated around the central region of cross-section, and some vortices are also formed near the wall region. There is an increase in the vorticity strength as we increase the inlet velocity.

## 3.4 Improvements

One of the major concerns in the operation of cyclone separators is erosion. Recent studies have shown an increase in interest to reduce the erosion in cyclone separators. Many design changes are recommended to change the geometry of the cyclone separator without impacting its performance.

The major region of concern for erosion in cyclone separators is the top part. For certain particle size ranges, particles are trapped in the vortices formed at the sharp

corners of the cyclone separator and they continuously erode the surface. This can be reduced by introducing fillets at the sharp corners. Different fillet radii (5mm, 10mm and 15mm) are considered and their effect on erosion is studied.

### 3.4.1 Particle motion modelling

$x_p$ refers to the position vector of the particle with respect to the origin, $u_p$ and $\omega_p$ refer to the particle velocity and angular velocity respectively. $m_p$ is the particle mass. As the particles move inside the fluid domain, it is affected by the forces that act on it. For the flow regimes in our study, the drag force ($F_D$), Saffman lift force ($F_S$), Magnus lift force ($F_M$) and the gravitational force ($F_G$) are the forces which play a major role and the other forces can be neglected [17].

$$\frac{dx_p}{dt} = u_p \tag{3.20}$$

$$m_p \frac{du_p}{dt} = F_D + F_S + F_M + F_G \tag{3.21}$$

$$F_D = \frac{m_p u_r}{\tau_p} \tag{3.22}$$

where, $\tau_p$ is the particle relaxation time.

$$\tau_p = \frac{\tau_{pst}}{f_d}, \tau_{pst} = \frac{\rho_p d_p^2}{18\mu} \tag{3.23}$$

where $\tau_{pst}$ is the particle Stokes number.

$$u_r = u_s - u_p \tag{3.24}$$

$u_r$ is the relative velocity between the fluid and the particle. ans $u_s$ is the fluid velocity seen by the particle.$u_s = U_{mean} + u'_s$ and $u'_s$ is reconstructed from hydrodynamic variables by the turbulent dispersion model. $U_{mean}$ is calculated as $< \overline{u} >$ where ¡ ¿ indicates ensembled average.

$$Re_p = \frac{|u_r| d_p}{\nu} \tag{3.25}$$

is the particle Reynolds number. $f_d$ is obtained by the following equations using the Schiller and Neumann correlation. [76]:

$$f_d = \begin{cases} 1; & Re_p \leq 1 \\ 1 + 0.15 Re_p^{0.687}; & 1 < Re_p \leq 1000 \\ \frac{0.44 Re_p}{24}; & Re_p > 1000 \end{cases} \tag{3.26}$$

Drag is the force that dominates among the forces taken into consideration, especially in the smaller particle regimes.

Saffmann force is a result of velocity gradients present in the fluid domain along the path of the particle, resulting in a pressure gradient which in turn produces a lift on particles.It is calculated using the Saffman-Mei correlation [77],[78]:

$$F_S = 1.61 C_s d_p^2 \rho (2\nu)^{1/2} |\omega|^{-1/2} (u_r \times \omega) \tag{3.27}$$

$$C_s = \begin{cases} (1 - 0.3314\lambda^{1/2}) exp(-0.1 Re_p) + 0.3314\lambda^{1/2}; & Re_p \leq 40 \\ 0.0524(\lambda Re_p)^{0.5}; & Re_p > 40 \end{cases} \tag{3.28}$$

where $\omega = 0.5(\nabla \times < u >)$ is the angular velocity of rotation of the fluid element and $\lambda = \frac{d_p |\omega|}{|u_r|}$.

Magnus force acts on a particle because of it's own spin which generates the lift. Magnus and Saffman forces become more important when the particle sizes become larger and particularly in erosion study [17] .This is calculated by Rubin and Keller relation [79].

$$F_M = \frac{\pi C_{LR} \rho d_p^2 |u_r|}{8|\omega|} (u_r \times \omega_r) \tag{3.29}$$

$$Re_\omega = \frac{|\omega_r| d_p^2}{\nu} \tag{3.30}$$

$$I_p \frac{d\omega_p}{dt} = T; T = -\frac{d_p^5 \rho}{64} C_R |\omega_r| \omega_r \tag{3.31}$$

$I_p = 0.1 m_p d_p^2$, where $I_p$ is the particle moment of inertia and the torque given by [80]. $C_R$ is as derived by Dennis *et al* [81]:

$$C_R = \begin{cases} 64\pi/Re_\omega; & Re_\omega \leq 32 \\ 12.9/Re_\omega^{0.5} + 128.4/Re_\omega; & 32 < Re_p \leq 1000 \end{cases} \tag{3.32}$$

### 3.4.2 Dispersion modeling

Initially, the model was derived from isotropic Langevin equations and was extended to LES by Limpowsky and Sommerfeld [21]. The velocity fluctuation that the particle will see in the next time step of its motion depends on the amount of fluctuation it sees at the present time. This effect is quantified by the drift term and indicates the memory effect. In the Sommerfeld's CRW, this involves a Lagrangian temporal correlation ($R_L$) and an Eulerian spatial correlation ($R_{E,ij}$).This effect is quantified by the drift term and indicates the memory effect. In the Sommerfeld's CRW, this involves a Lagrangian temporal correlation ($R_L$) and an Eulerian spatial correlation ($R_{E,ij}$).

$$u_i'^{n+1} = R_{P,i}(\Delta t_L, \Delta r) u_i'^n + \sigma_f \sqrt{1 - R_{P,i}^2(\Delta t_L, \Delta r)}\zeta_i + \left[\frac{1}{1+St_d}\right]\frac{1}{\rho}\frac{\partial(\rho < u_i' u_j' >)}{\partial x_j} \tag{3.33}$$

$$R_{E,ij}(\Delta r) = (f(\Delta r) - g(\Delta r))\frac{\Delta r_i \Delta r_j}{|\Delta r|^2} + g(\Delta r)\delta_{ij} \tag{3.34}$$

$$R_L(\Delta t_L) = exp(-\frac{\Delta t}{T_L}) \tag{3.35}$$

$$f(\Delta r) = exp(-\frac{\Delta r_i}{L_{E,i}}), g(\Delta r) = f(\Delta r)(1 - \frac{\Delta r_i}{2L_{E,i}}) \tag{3.36}$$

$$R_{P,i} = R_{E,ij}(\Delta r) \times R_L(\Delta t_L) \tag{3.37}$$

$$L_{E,\parallel} = 2L_{E,\perp} \tag{3.38}$$

The equation is written in the local coordinate system with the the first coordinate parallel to $-U_r$ at that point. So, the variables involved must be transformed to the local

coordinate system with transformation tensor and after the fluctuations are obtained locally, they must be back transformed to the global coordinate system. In Equation 3.35, the fluid time scale $T_L = \frac{C_T \sigma_F^2}{\epsilon_{SGS}}$ and the turbulent length scale $L_E = C_L \sigma_f T_L$. Here, $\sigma_f = \sqrt{\frac{2k_{SGS}}{3}}$ and constants $C_T = 0.24$, $C_L = 3.0$. $\Delta r_i$ refers to the relative position vector and $\Delta r$ refers to the magnitude of relative displacement. In Equation 3.33, the third term is called the drift correction term and is of great importance in accounting for the inhomogeneity in turbulence and, if excluded could even result in an error of 500% as highlighted by Bockshell and Loth [82].

### 3.4.3 Erosion modelling

Zhang's model[83] was used to predict erosion in our work, since it gave best experimental match for us. The model has been applied to various mateials and flow situations and has always yielded good results. This E/CRC model predicts erosion ratio as follows:

$$ER = C(BH)^{-0.59} F_s V_p^n F(\theta) \tag{3.39}$$

$$F(\theta) = \sum_{i=1}^{5} A_i \theta_i \tag{3.40}$$

Here, $A_1 = 5.4, A_2 = -10.11, A_3 = 10.93, A_4 = -6.33, A_5 = 1.42$. ER refers to the mass of the wall material removed per mass of impinging particle. BH refers to the Brinell Hardness of the material which is eroded and $V_p$ is the impact velocity of the particle and n is the exponent of velocity associated with the model and is taken to be 2.41. $F_s$ refers to the particle shape coefficient and is 1 for sharp/angular particles. 0.53 for semi rounded particles and 0.2 for fully rounded particles. Our cases are all for fully rounded particles. C is an empirical constant whose value is $2.17 \times 10^{-7}$. The Erosion ratio must be multiplied by mass of the particle impacting it and divided by area of the cell of impact and the density of the wall material to get the units to m/kg which is what we use. The value is multiplied by mass during every collision and the summation of these values is normalised with the total mass injected to be reported.

### 3.4.4 Restitution and coefficient of friction modelling

Of the restitution models available, we have used the model of Forder *et al* [27]. This model was originally developed on Stainless steel chokes which raise from reservoirs and have been used widely used since then in various scenarios to capture the particle wall local interaction.

$$e_n = 0.988 - 0.78\alpha + 0.19\alpha^2 - 0.024\alpha^3 + 0.027\alpha^4 \tag{3.41}$$

$$e_t = 1 - 0.78\alpha + 0.84\alpha^2 - 0.21\alpha^3 + 0.028\alpha^4 - 0.022\alpha^5 \tag{3.42}$$

$$\mu_{st} = \mu_{dy} = \mu = max(0.5 - 0.175\alpha, 0.15) \tag{3.43}$$

$e_n$, $e_t$ are coefficients of restitution in the normal and tangential directions to the wall normal vector respectively. $\alpha$ is the angle of contact between the particle velocity vector and the unit wall normal vector.$\mu_{st}$ and $\mu_{dy}$ are static and dynamic coefficients of friction respectively.The coefficient of friction plays an important role in the particle wall interaction. In the studies carried out by Pereria *et al.* [84], it is clear that this way of modelling coefficient of friction gives the best match to experiments and thus has been used by us. The model in 3.43 was developed by Sommerfield and Huber [85] in their work on particle laden horizontal flow measured with Laser beams.

### 3.4.5 Rebound model

When the particle collides with the wall, there is exchange of energy and momentum between the wall and particles. This leads to a change in linear and angular velocities after collision and the modelling approach of Breuer *et al.*[86] is applied here. Sufficient mass loading was used to test and validate for different scenarios in 3D, which makes the model highly generic [86].$u_{pr}$ is the relative velocity of the point of contact during collision, $\nu_{cr}$ is the critical relative velocity,$n$ is the unit normal vector.

$$u_{pr} = u_p^- - (u_p^- \cdot n)n - \frac{d_p}{2}\omega_p \times n \tag{3.44}$$

$$\nu_{cr} = -\frac{7\mu_{st}(1+e_n)u_p^- \cdot n}{2(1+e_t)} \tag{3.45}$$

$$u_p^+ = u_p^- - \frac{2(1+e_t)u_{pr}^-}{7} + (1+e_n)(u_p^- \cdot n)n \tag{3.46}$$

$$\omega_p^+ = \omega_p^- + \frac{10(1+e_t)n \times u_{pr}^-}{7d_p} \tag{3.47}$$

If $|u_{pr}| <= \nu_{cr}$, it is considered non sliding collision and the equations 3.46 and 3.47 are applied.

$$u_p^+ = u_p^- + (1+e_n)(u_p^- \cdot n)[\mu_{dy}\frac{u_{pr}^-}{|u_{pr}^-|} - n] \tag{3.48}$$

$$\omega_p^+ = \omega_p^- - \frac{5}{d_p}(1+e_n)(u_p^- \cdot n)\frac{\mu_{dy}}{|u_{pr}^-|}n \times u_{pr}^- \tag{3.49}$$

Otherwise, the collision is taken to be sliding and 3.48 and 3.49 are used in post collision calculations. Here, '+' and '-' refers to values after and before the collision respectively.

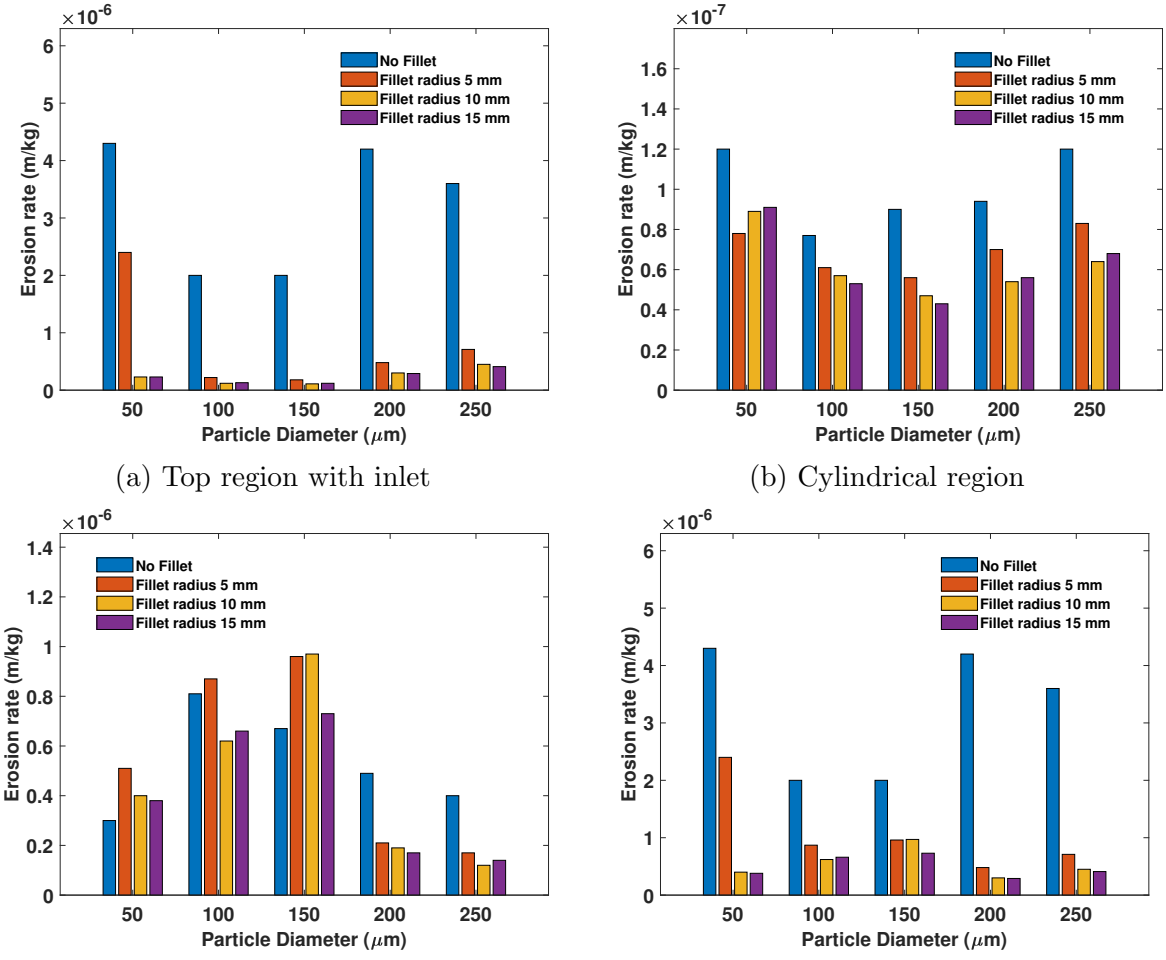


(a) Top region with inlet

(b) Cylindrical region

(c) Cone region

(d) Total cyclone

Figure 3.18: Erosion reduction due to fillets

## 3.5 Conclusions

The flow field characteristics observed in cyclone separators are predominantly turbulent and multiphase in nature. This requires precise calculations of the velocity fields and Reynolds stress to augment the design of cyclone separators. In this study, the hybrid LES/RANS models DES, DDES and IDDES based on the two-equation $k-\omega$ SST RANS model are studied in detail and are proposed as an alternative to the Reynolds Stress Model (RSM) and the Large Eddy Simulations (LES) for cyclone-separator fluid flow simulations. The hybrid models are able to accurately reproduce the experimental results and require a smaller mesh size than the LES model. The hybrid turbulence models are also able to capture the anisotropy in the Reynolds stresses much better than the Reynolds Stress Model (RSM) which is important for multiphase dispersion models. The RSM model is not able to account for the precessing vortex core effects which limits the usage of the model. Among the hybrid models, it is found that the IDDES model based on $k-\omega$ SST produces the most accurate results due to better switching model between the RANS and LES regions.

The predictions of velocity between the different models are discussed and it is found that the location of peak velocity remains the same across various inlet velocities. The radial velocity profiles which are difficult to measure in experiments are plotted and are found not to be axisymmetric. This observation is further established by looking at the anisotropy of the Reynolds stress profiles obtained from the simulations. Therefore for cyclone separators, it is recommended not to use axisymmetric simulation conditions. RANS models predict the Reynolds stresses which are on the plane strain limit, which is not desired for dispersion models in particle motion. The hybrid/LES models perform better than the RANS and RSM models in providing better predictions to Reynolds Stresses.

The flow within the cyclone separator is predominantly vortex dominated. The vortex line graphs are plotted at various cross-sections helps to visualise the vorticity and understand the energy losses in the flow.

The main objective of this study is to highlight the gain in speed of simulations and reduction in mesh requirement. There is a reduction in computational time of 55% when compared to the LES model for a 37% reduction in mesh size. Saving in computational time is paramount for industrial research studies, as it leads to quicker development.

There is considerable erosion reduction due to filleting the sharp corner of the cyclone separator. For fillet radius of 10 mm, there is a reduction of erion of 90% for the 50 $\mu m$ particle.

# Chapter 4

# Performance of 3D twisted S-shaped fins

## 4.1 Numerical modeling

To reduce the computational time spent in simulating the fins on the plate heat exchanger, it is economical to use a periodic domain of the repeating fin pattern. This section describes the geometry, the governing equations and boundary conditions used in this study.

### 4.1.1 Geometry

The parameterization of S-shaped fins is shown in Equation 4.1.

$$y = \zeta sin(\omega x) \tag{4.1}$$

where the variables are defined as follows:

Table 4.1: Parameters for S-shaped fin

| Variable name | Expression |
|---|---|
| $\zeta$ | $0.5 l_f sin(\psi)$ |
| $\omega$ | $\pi$ / $(l_f cos\psi)$ |
| $\psi$ | $tan^{-1}((2/\pi)tan\phi)$ |

The curve is formed by moving the curve along the direction vector (a,b), which are defined as follows:

$$a = \frac{d_f cos\beta}{2cos(\frac{\pi}{2} - \phi - \beta)} \tag{4.2}$$

$$b = \frac{d_f sin\beta}{2cos(\frac{\pi}{2} - \phi - \beta)} \tag{4.3}$$

where $\beta$ is the direction vector angle with respect to the x-axis. $\beta$ needs to be selected by us.

The parameters which can be varied are:

1. Length of the fin ($l_f$)

2. Width of the fin ($d_f$)

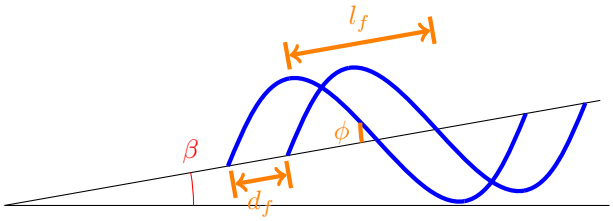


Figure 4.1: 2D drawing of S-shaped fin and parameters involved

Figure 4.2: Geometry

3. $\phi$ - Angle the curve makes with the horizontal

4. $\beta$

The 2D construction of the S-shaped fins is shown in Fig. 4.1. To create normal S-shaped fins, the overlapping region is extruded in the normal direction. To create a 3D twisted S-shaped fin, we must include a rotation about the centre of the fin while extruding.

The geometry is shown in Figure 4.2. The geometry consists of the S-shaped fin and repetition of the fin in the streamwise ($x$) and spanwise ($y$) direction. The dimensions of the geometry is two times the pitch in the $x$ and $y$ direction. The pitch chosen for this study is 8.45 mm in the streamwise direction and 3.45 mm in the spanwise direction. The fins are extruded for 1 mm in the z direction. The S-shaped fins are then twisted in the z direction about the center of the fin. The twist angles chosen for this study are $0^o$ (No twist), $10^o$, $20^o$ and $30^o$. The maximum twist angle is restricted by manufacturing constraints from additive manufacturing. The no twist and $30^o$ twisted S-shaped fins are shown in Figure 4.3.

(a) No twist fin (b) $30^o$ twisted fin

Figure 4.3: 3D twisted S-shaped fins

### 4.1.2 Numerical Modeling

The Navier-Stokes and Energy equations need to be modified to account for the periodic boundary conditions in the streamwise and spanwise directions. The equations accounting for this are given in Equations 4.4-4.9. The equations are implemented in OpenFOAM as a separate solver[87]. A momentum source ($\chi$) needs to be added to maintain the mass-flow rate or pressure drop in the flow. In the same manner, there is a sourcing term for the energy equation ($\gamma$). The method used here is the one proposed by Patankar [88] and also used by Allan Bjerg and Kristian Christoffersen [89].

$$\frac{\partial \overline{u}_i}{\partial x_i} = 0 \tag{4.4}$$

$$\frac{\partial \overline{u}_i}{\partial t} + \overline{u_j}\frac{\partial \overline{u_i}}{\partial x_j} = -\frac{1}{\rho}\frac{\partial \overline{p}}{\partial x_i} + \frac{\partial}{\partial x_j}\left[\left(\nu + \nu_\mathrm{t}\right)\frac{\partial \overline{u}_i}{\partial x_j}\right] + \chi\delta_{1i} \tag{4.5}$$

$$\frac{\partial \overline{T}}{\partial t} + \overline{u_j}\frac{\partial \overline{T}}{\partial x_j} = \frac{\partial}{\partial x_j}\left[\left(\frac{\nu}{\mathrm{Pr}} + \frac{\nu_\mathrm{t}}{\mathrm{Pr}_\mathrm{t}}\right)\frac{\partial \overline{T}}{\partial x_j}\right] - \gamma\bar{u}_1 \tag{4.6}$$

$$\chi = \frac{\overline{p}(x,y) - \overline{p}\left(x + L_\mathrm{d}, y\right)}{L_\mathrm{d}} \tag{4.7}$$

$$\gamma = \frac{\overline{T}\left(x + L_\mathrm{d}, y\right) - \overline{T}(x,y)}{L_\mathrm{d}} \tag{4.8}$$

$$\gamma = \frac{\dot{q}}{H c_{\mathrm{p}} u_{\mathrm{bulk}}\, \rho} \tag{4.9}$$

The equations only allow for a flow with a primary direction as the x axis. This can be seen in Equation 4.5 where the momentum source is only multiplied by the Delta function and applies only to the x momentum equation. For the energy equation, the thermal source is multiplied by $u_1$, which is the velocity in the x direction. In the above equations, $L_D$ is the length of the domain in the x direction.

### 4.1.3 Turbulence modeling

The Reynolds number involved in this study fall in the turbulent regime. Since the equations are implemented in OpenFOAM, it is possible to make use of the various turbulence models available in the software. For this study the RANS based k-$\omega$ SST turbulence model is used. The equations for the k-$\omega$ SST model are given in Equations 4.10 - 4.13.

$$\frac{\partial k}{\partial t} + \overline{u_j}\frac{\partial k}{\partial x_j} = P_k - \beta^* k\omega + \frac{\partial}{\partial x_j}\left[\left(\nu + \sigma_k \nu T\right)\frac{\partial k}{\partial x_j}\right] \tag{4.10}$$

$$\frac{\partial \omega}{\partial t} + \overline{u_j}\frac{\partial \omega}{\partial x_j} = \alpha S^2 - \beta\omega^2 + \frac{\partial}{\partial x_j}\left[\left(\nu + \sigma_\omega \nu_T\right)\frac{\partial \omega}{\partial x_j}\right] + 2\left(1 - F_1\right)\sigma_{\omega 2}\frac{1}{\omega}\frac{\partial k}{\partial x_i}\frac{\partial \omega}{\partial x_i} \tag{4.11}$$

$$F_1 = \tanh\left\{\min\left[\max\left(\frac{\sqrt{k}}{\beta^*\omega y}, \frac{500\nu}{y^2\omega}\right), \frac{4\sigma_{\omega 2} k}{C D_{k\omega} y^2}\right]\right\}^4 \tag{4.12}$$

$$\nu_T = \frac{a_1 k}{\max\left(a_1\omega, S F_2\right)} \tag{4.13}$$

$$F_2 = \tanh\left[\max\left(\frac{2\sqrt{k}}{\beta^*\omega y}, \frac{500\nu}{y^2\omega}\right)\right]^2 \tag{4.14}$$

$$P_k = \mu_t \left( \frac{\partial \overline{u_j}}{\partial x_i} + \frac{\partial \overline{u_i}}{\partial x_j} \right) \frac{\partial \overline{u_j}}{\partial x_i} - \frac{2}{3} \rho k \frac{\partial \overline{u_j}}{\partial x_i} \tag{4.15}$$

The values of $k$ and $\omega$ are used to calculate $\nu_t$ which is used in the Navier-Stokes and energy equations. The term $P_k$ in Equation 4.10 is the production term and is defined in Equation 4.15. The constants used in the turbulence model are shown in Table 4.2. $S$ is the strain-rate tensor. The constants are computed by a blend from the corresponding constant of $k-\epsilon$ and the $k-\omega$ model via $\alpha = \alpha_1 F + \alpha_2(1-F)$. $y$ is the distance to the nearest wall.

Table 4.2: Constants for k-$\omega$ SST model

| $\sigma_{k1}$ | $\sigma_{k2}$ | $\sigma_{\omega 1}$ | $\sigma_{\omega 2}$ | $\beta_1$ | $\beta_2$ | $\gamma_1$ | $\gamma_2$ | $\beta^*$ | $a_1$ | $b_1$ | $c_1$ |
|---|---|---|---|---|---|---|---|---|---|---|---|
| 0.85 | 1.0 | 0.5 | 0.856 | 0.075 | 0.0828 | 5/9 | 0.44 | 0.09 | 0.31 | 1 | 10 |

### 4.1.4 Boundary conditions

Cyclic Arbitary Mesh interface (AMI) boundary conditions are used in the stream-wise and span-wise directions for all the variables ($\overline{u}$, $\overline{T}$, $\overline{p}$, $k$ and $\omega$). This boundary condition allows for non-conformal patches to have a periodic boundary condition. The walls have a no-slip boundary condition for velocity and constant temperature. The equations are iterated till a constant value of gamma is achieved which corresponds to a constant heat flux condition. The fvOptions is used to set the forcing velocity for the periodic flow.

### 4.1.5 Calculated Quantities

The quantities quantified in this study are the friction factor ($f$) and Nusselt number ($Nu$). The friction factor is calculated from the pressure drop obtained from the solver.

$$f = \frac{D_h}{0.5 \rho u_{ref}^2} \frac{dP}{dx} \tag{4.16}$$

The Nusselt number is calculated on all the wall patches in the domain. This includes all the fin surfaces as well as the bounding walls in the non-periodic directions. This is

done to reflect the conditions in a plate heat exchanger with fins.

$$Nu = -\frac{dT}{dn}\frac{D_h}{\Delta T} \tag{4.17}$$

$$\frac{dT}{dn} = \frac{\sum \frac{dT}{dn} A_i}{\sum A_i} \tag{4.18}$$

$$\Delta T = T_{wall} - T_{ref} = T_{wall} - \frac{\sum T_i u_1 A_i}{\sum u_1 A_i} \tag{4.19}$$

The reference temperature ($T_{ref}$) is calculated on the periodic patch in the streamwise direction. It is calculated on the velocity-weighted average in the streamwise direction. The temperature gradient is calculated by area-weighted average over all the wall patches in the domain.

The performance evaluation criteria (PEC) is calculated from the friction factor and Nusselt number. PEC is calculated for equal pumping power.

$$PEC = \frac{Nu/Nu_0}{(f/f_0)^{1/3}} \tag{4.20}$$

## 4.2 Validation

### 4.2.1 Solver Validation

For validating the solver, we use the DNS data of Poiseuille flow for a $Re_\tau = 180$. This flow was chosen for its simple geometry and the presence of periodic boundary conditions in the streamwise and spanwise directions. The results from the $k - \omega$ SST model is compared with the DNS data. The results are shown in Figure 4.4.

From the results, it can be concluded that the solver is able to solve periodic flows with periodic boundary conditions in the streamwise and spanwise directions.

## 4.3 Results

The simulations in this study are run for 8 different Reynolds number. Variations in flow variables are observed due to vortex shedding from the fins. Therefore the variables are

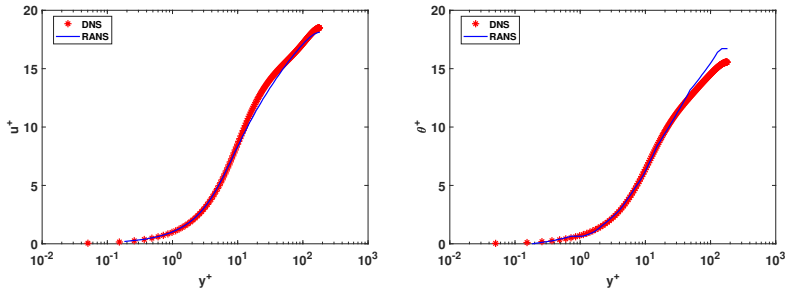


(a) $u^+$




(b) $\theta^+$

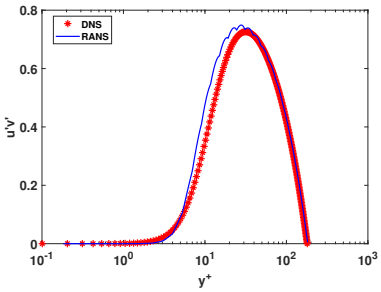


(c) $< u'v' >$

Figure 4.4: Solver Validation

time averaged to get the statistics. All the simulations are run for 15 flow through time to let the flow reach a steady state. After the 15 flow through times, the flow variables are averaged for another 11 flow through time to capture the variations in the Nusselt number and friction factor prediction.

### 4.3.1 Performance

Thermo-hydraulic performance is the key factor which needs to be considered for any new fin developed. The Nusselt number and friction factor are calculated for the 4 different twists. The Nusselt number decreases with increase in the twist angle. The variation of Nusselt number with Reynolds number for Prandtl number of 0.8449 is shown in Fig. 4.5. The Prandtl number 0.8449 corresponds to the inlet conditions on the cold side of the heat exchanger. The Nusselt number decreases as we increase the twist. The difference in Nusselt number increases as the Reynolds number increases.

The friction factor is the major reduction we see with the increase in the twist angle. There is reduction of approximately 70% in the friction factor. This will greatly reduce the pumping requirement. The variation of friction factor with Reynolds number for

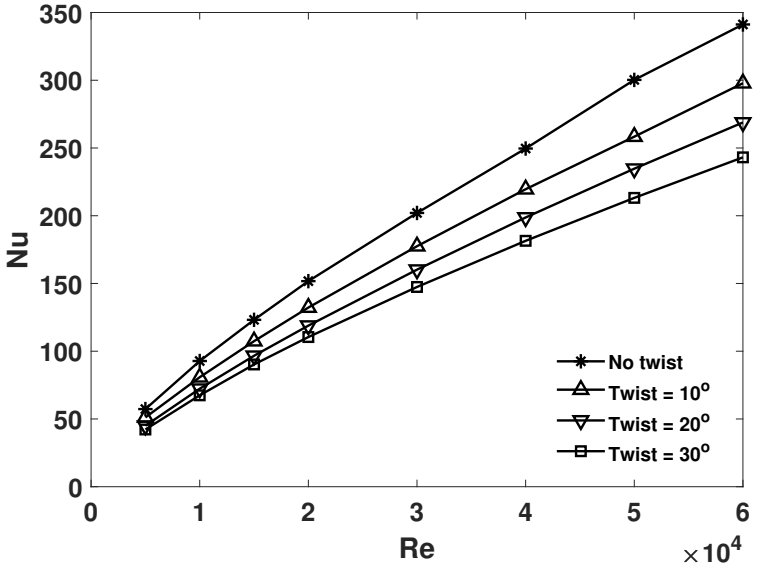


Figure 4.5: Nusselt number variation for Pr = 0.8449

different twist angles is shown in Fig. 4.6. In the turbulent regime, the friction factor continuously reduces with increase in Reynolds number and this is observed in all the twist angles.

Despite the reduction in Nusselt number, the reduction in friction factor overshadows it and we see an increase in the Performance Evaluation Coefficient (PEC). This increase in PEC is shown in Fig. 4.7. We see maximum PEC for twist of $30^o$. The maximum PEC is 13%. The increase in PEC shows that increasing the twist angle results in a higher performance.

The Chilton and Colburn J-factor analogy is calculated to find the relationship between fluid flow and heat transfer. This is shown in Fig. 4.8. The X axis has the friction factor and the Y axis corresponds to $Nu/(RePr^{(1/3)})$. When this line is plotted, we see that for a given twist angle, all the data points fall in a straight line. This data can be used to predict the performance of the system at intermediate data points and can also be extrapolated.

The non-dimensional variables used for post-processing are defined as:

$$U^* = \frac{u}{u_{ref}} \tag{4.21}$$

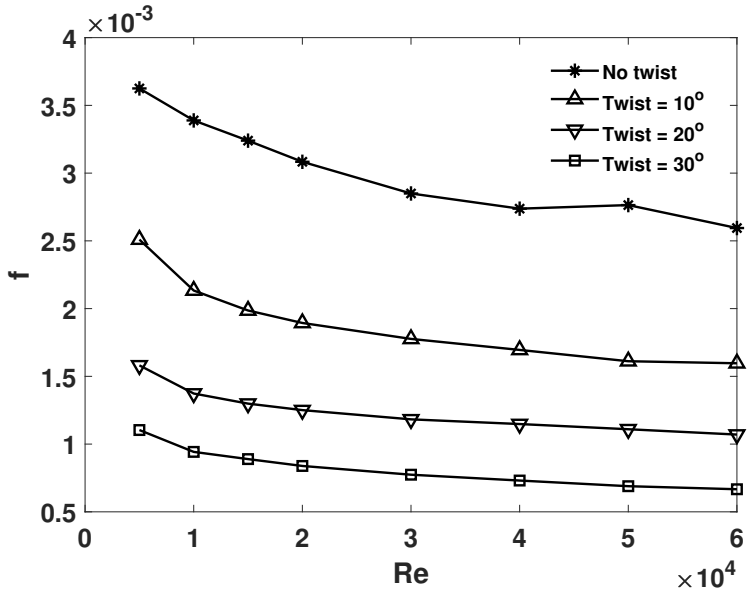


Figure 4.6: Friction factor variation for Pr = 0.8449

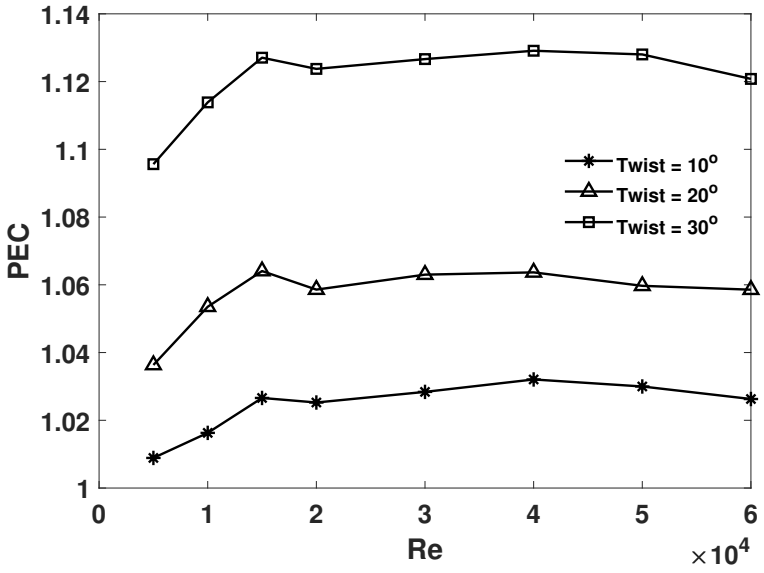


Figure 4.7: PEC for Pr = 0.8449

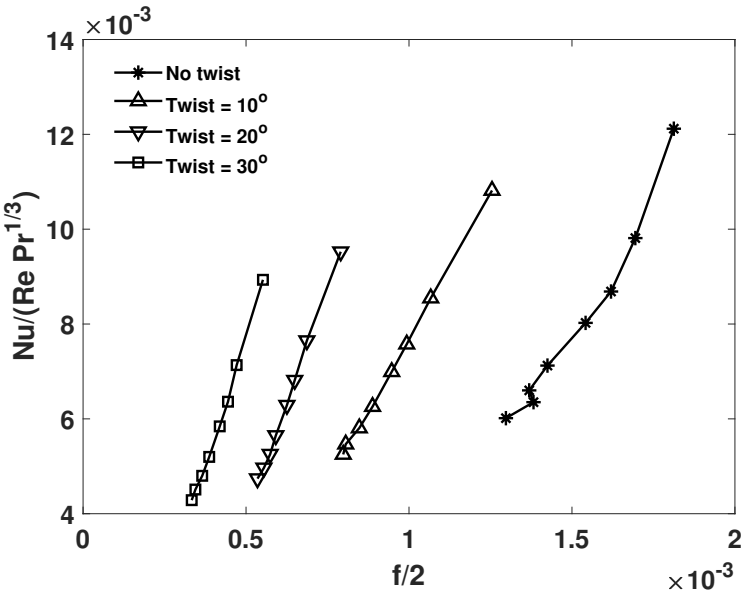


Figure 4.8: j factor for Pr = 0.8449

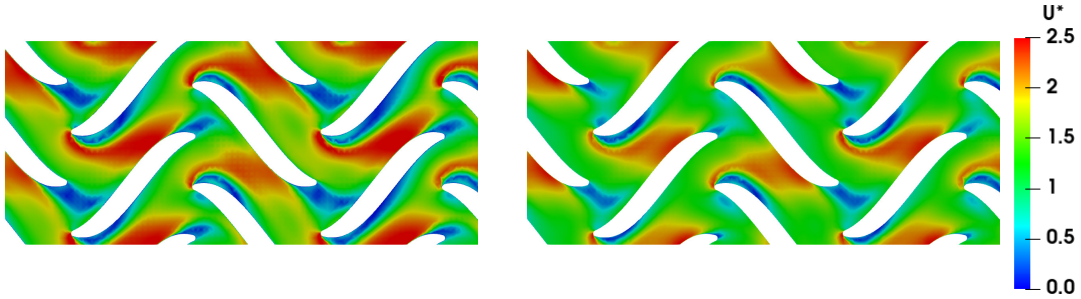


(a) Re = 5000 (b) Re = 60000

Figure 4.9: Time-averaged velocity contour for no twist

$$\omega^* = \frac{\omega}{(u_{ref}/D_h)} \tag{4.22}$$

$$\tau^* = \frac{\tau_w}{0.5\rho u_{ref}^2} \tag{4.23}$$

$D_h$ is the hydraulic diameter. It is defined based on the smallest area between two fins ($D_h = 4A/P$). The hydraulic diameter changes with twist angle as the area between two fins changes. $u_{ref}$ is defined based on the Reynolds number of the flow. $Re = \rho u_{ref} D_h/\mu$.

Figures 4.9, 4.10 and 4.11 show the normalized velocity, normalized vorticity and normalized wall shear stress for the no twist fin at Reynolds number of 5000 and 60000. As we increase the Reynolds number, we see that the recirculation region behind the fin reduces. This is seen in the velocity and vorticity contours. In the wall shear stress contour, we observe that the negative wall shear stress region reduces as we increase the

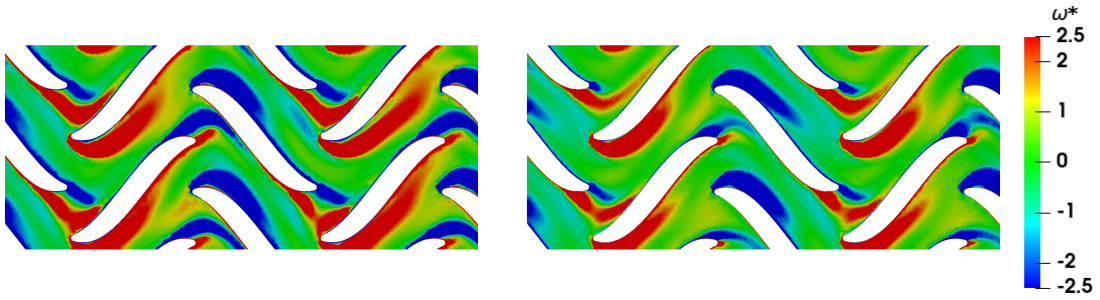


(a) Re = 5000 (b) Re = 60000

Figure 4.10: Time-averaged vorticity contour for no twist

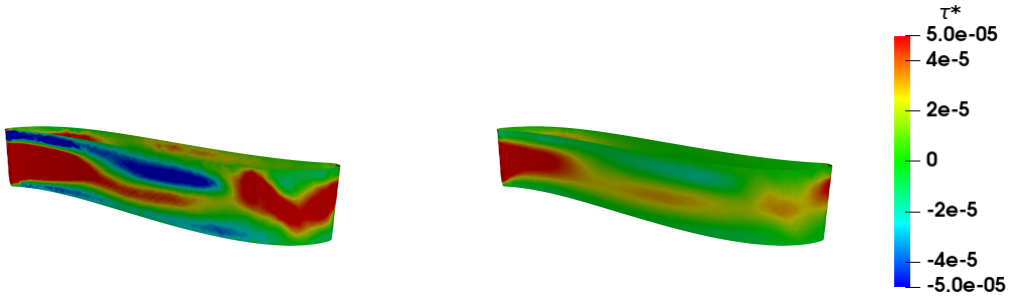


(a) Re = 5000 (b) Re = 60000

Figure 4.11: Time-averaged Wall Shear Stress contour for no twist in the central fin

Reynolds number. This results in reduced friction factor.

Figures 4.12, 4.13 and 4.14 show the normalized velocity, normalized vorticity and normalized wall shear stress for the $10^o$ twist fin at Reynolds number of 5000 and 60000. Compared to the no twist fin, we find that the vortex regions behind the fin is more closer to the fin. This is because the streamlines tend to stick to the twisted fin and not separate. There is significant change in the wall shear stress contour when compared to the no twist. The wall shear stress contour for Re 60000 is mostly close to zero as there

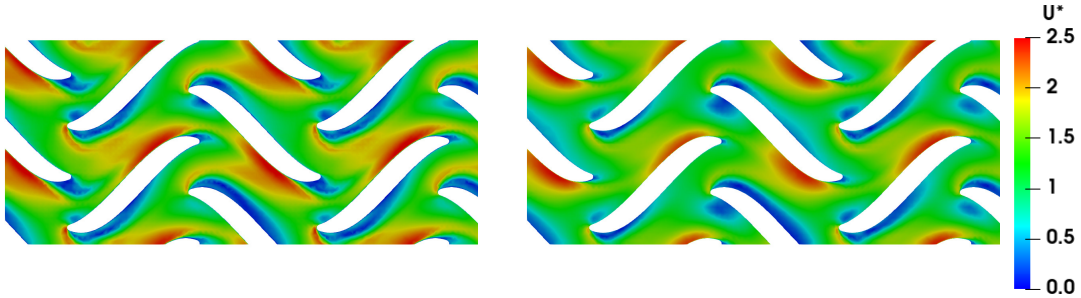


(a) Re = 5000 (b) Re = 60000

Figure 4.12: Time-averaged velocity contour for $10^o$ twist

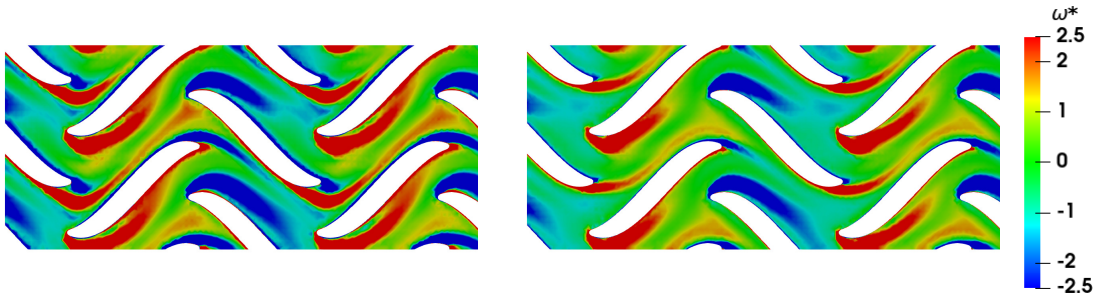


(a) Re = 5000 (b) Re = 60000

Figure 4.13: Time-averaged vorticity contour for $10^o$ twist

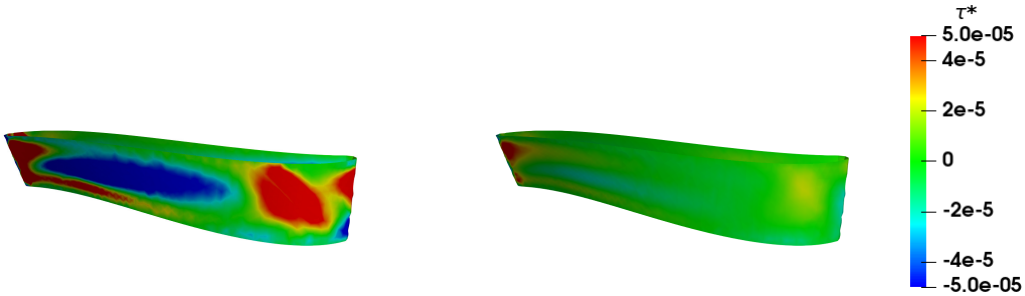


(a) Re = 5000 (b) Re = 60000

Figure 4.14: Time-averaged Wall Shear Stress contour for $10^o$ twist in the central fin

is less separation and recirculation.

Figures 4.15, 4.16 and 4.17 show the normalized velocity, normalized vorticity and normalized wall shear stress for the $20^o$ twist fin at Reynolds number of 5000 and 60000. The vortex regions are much closer to the fin and this results in even more reduction in the friction factor. There is reduction in the Nusselt number as the recirculation region is reduced compared to the no twist and $10^o$ twist fins.

Figures 4.18, 4.19 and 4.20 show the normalized velocity, normalized vorticity and

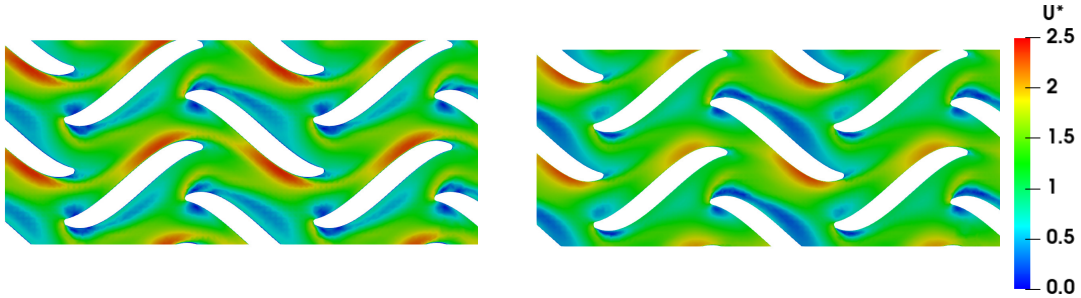


(a) Re = 5000 (b) Re = 60000

Figure 4.15: Time-averaged velocity contour for $20^o$ twist

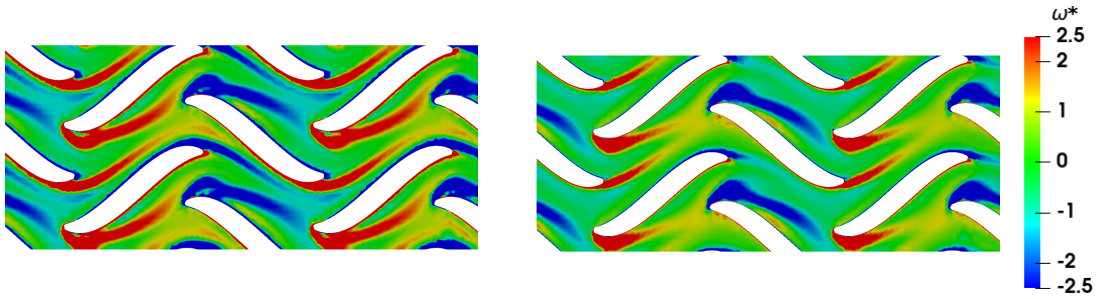


(a) Re = 5000 (b) Re = 60000

Figure 4.16: Time-averaged vorticity contour for $20^o$ twist

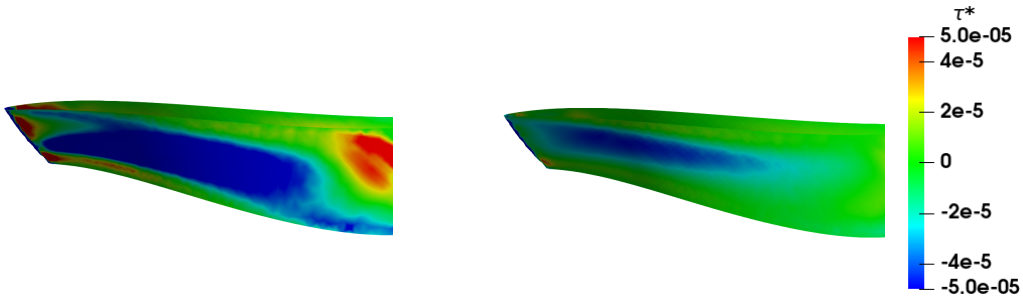


(a) Re = 5000 (b) Re = 60000

Figure 4.17: Time-averaged Wall Shear Stress contour for $20^o$ twist in the central fin

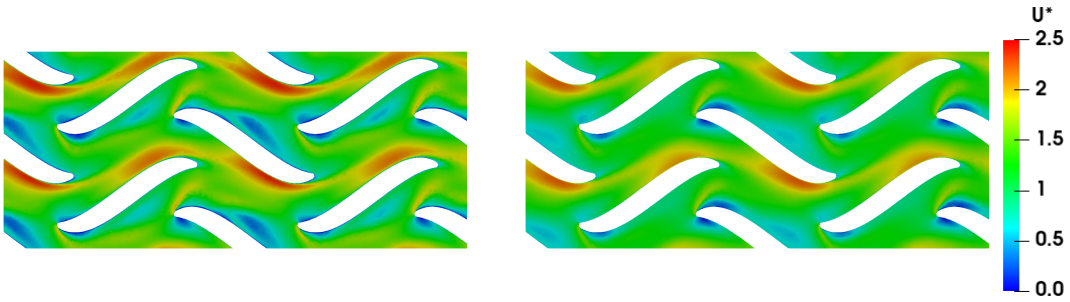


(a) Re = 5000 (b) Re = 60000

Figure 4.18: Time-averaged velocity contour for $30^o$ twist

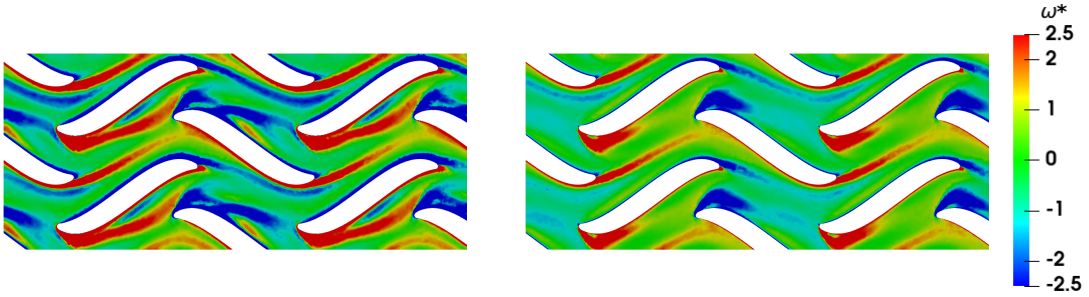


(a) Re = 5000 (b) Re = 60000

Figure 4.19: Time-averaged vorticity contour for $30^o$ twist

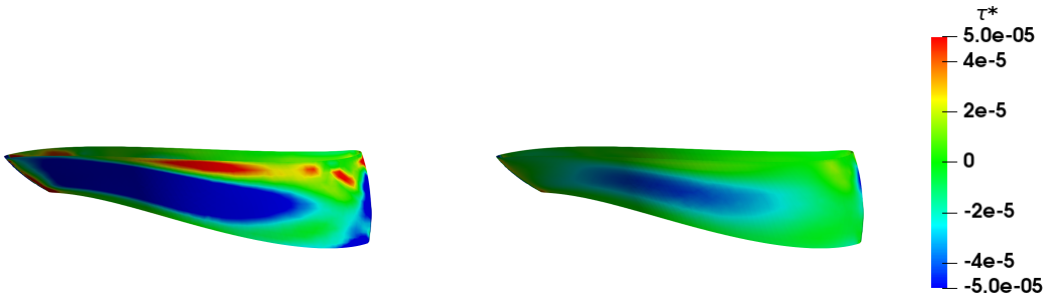


(a) Re = 5000 (b) Re = 60000

Figure 4.20: Time-averaged Wall Shear Stress contour for $30^o$ twist in the central fin

normalized wall shear stress for the $30^o$ twist fin at Reynolds number of 5000 and 60000.

Figures 4.9 to 4.20 show the time-averaged non-dimensional velocity, time-averaged non-dimensional vorticity and time-averaged non-dimensional wall shear-stress on the central fin for different angles of twist. The time-averaged wall shear stress reduces as the we increase the Reynolds number for all angles of twist. For the highest Reynolds number (Re = 60000), we see that there is reduction in the negative wall shear stress when compared to the lower Reynolds numbers. This results in a decrease in the friction factor.

The velocity patterns change as we increase the twist of the fin. The no twist fins have a separation region which has high velocity. But as we increase the twist of the fins, the separation region reduces in length and the velocity is more streamlined. The velocity tends to stay connected to the fins. The maximum velocity also decreases as we increase the twist of the fins.

The vorticity is much higher in the no twist fins compared to the $30^o$ twisted fins. The twist reduces the separation and removal of recirculation zones. This reduces the pressure drop drastically and also the friction factor.

## 4.4 Conclusions

Novel 3D twisted S-shaped fins are designed for plate heat exchangers. These heat exchangers are to be used in the next generation supercritical $CO_2$ power plants. There is always a need to improve the performance of heat exchangers to reduce the pumping

requirement without losing heat transfer performance. Instead of simulating the entire plate of the heat exchanger, a representative periodic domain is chosen to reduce the computational time for studying more designs. Periodic heat transfer with turbulence modelling is used to gather data on the performance of the 3D twisted S-shaped fins. The 3D twisted S-Shaped fins provide almost 75% reduction in the pumping requirement with improved performance efficient coefficient of 10%-13%. The reduction in the friction factor is due to the reduction in the recirculation zone behind the fin. The streamlines are more attached to the fin as we increase the twist angle.

# Chapter 5

# Design of Full Scale Heat Exchanger

## 5.1 Introduction

In this chapter, we build on the 3D twisted S-shaped fins performance to build full-scale heat exchangers. Firstly we evaluate the performance of a single plate of a plate heat exchanger built using Laser Powder Bed Fusion (LPBF) with titanium material with 3D twisted fins. The CFD data is compared with the experimental data obtained in-house. The friction factor and Nusselt number are compared with the experimental data. In addition to the 3D twisted fin plate, a flat plate data is also obtained to calculate the efficiency of the fins.

A heater for the full scale heat exchanger testing was developed by the experimental team. Testing on the heater was limited, therefore CFD was used to supplement the experiments. CFD is used to measure the performance of the heater and get detailed temperature measurements over the heater.

Finally, full-scale themo-mechanical and fluid flow simulations of the plate heat exchangers have been carried out for various geometric dimensions. The plates are manufactured using Additive Manufacturing technologies. Two additive manufacturing techniques considered in this study are the Laser Powder Bed Fusion (LPBF) and SEAM process. The green parts made from manufacturing process have to be sintered in furnaces and this process also posses some constraints on the geometric dimensions. Using the existing equipment available in-house, the maximum size of parts that can be generated is 12.5 cm $\times$ 12.5 cm using the SEAM process and 8.5 cm $\times$ 8.5 cm using LPBF.

## 5.2 Single Plate Data

### 5.2.1 Geometry

The simulations for a single plate is carried out using ANSYS 2021R2. The geometry of the assembly is shown in Fig. 5.1. The geometry is an assembly of 5 different parts - titanium plate (bluish gray), aluminium header(green), rubber seal (magenta), copper

sheet (pink) and polyamide heaters (pink). Seven polyamide heaters are used to provide the heat flux. The heaters are mounted on a copper sheet. The copper sheet is then attached to the backside of the plate assembly. The plate assembly consists of the titanium plate which is enclosed in an aluminium header. The aluminium header is sealed with the titanium plate using a rubber seal. The thickness of the plate is 4 mm, with a fluid gap of 1 mm. The closeup of the fins is shown in Fig. 5.2. The geometry for the flat plate is similar to the plate with fins, with only the fins removed.

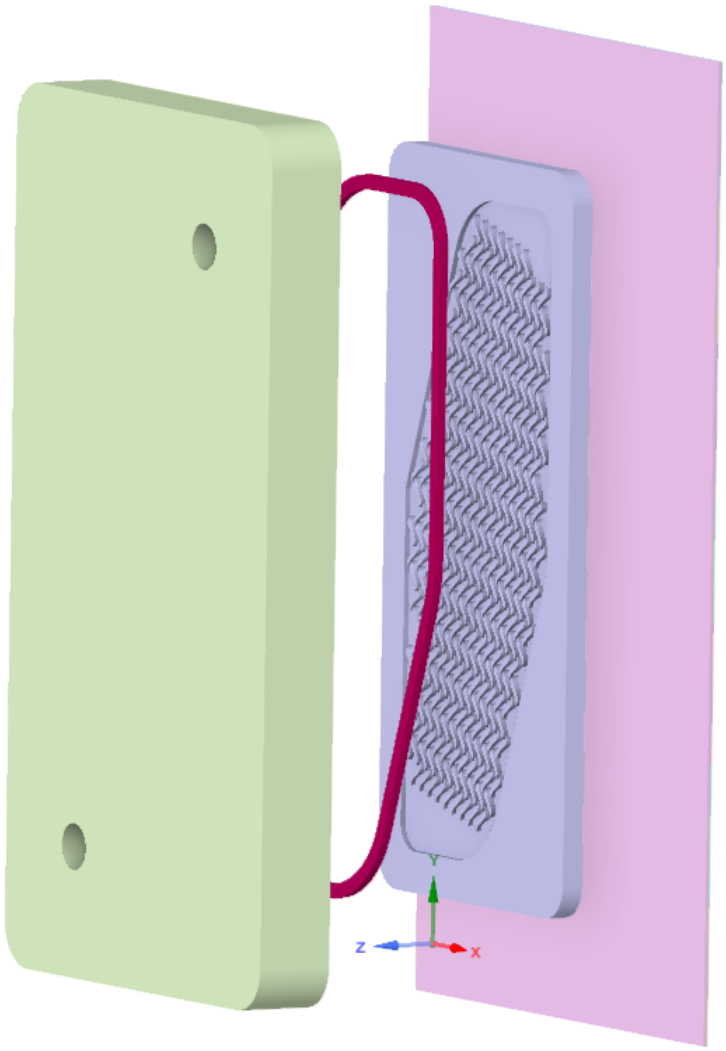


Figure 5.1: Exploded view of assembly

The mesh is generated for the entire assembly using ANSYS Fluent Meshing. Generating the mesh for this geometry was difficult owing to the close gaps between the 3D twisted S-shaped fins. Initial attempts were made using the tetrahedral elements, but

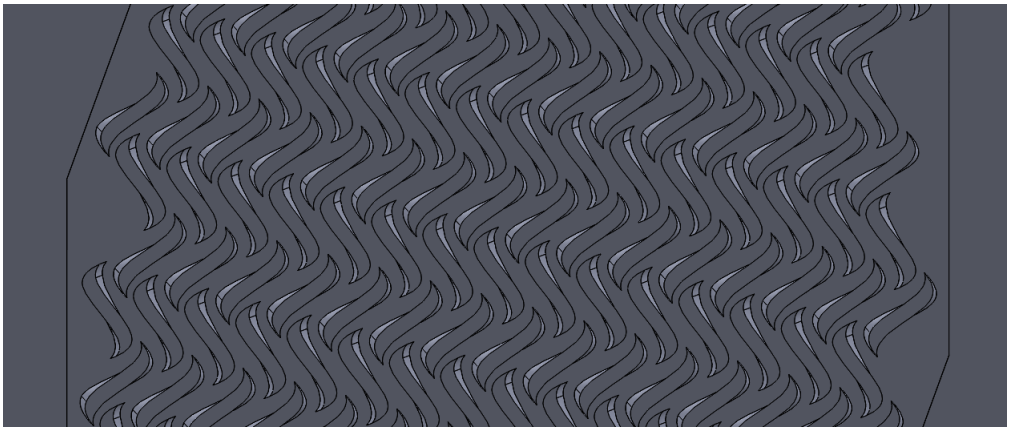

Figure 5.2: Close up of the 3D twisted S-shaped fins

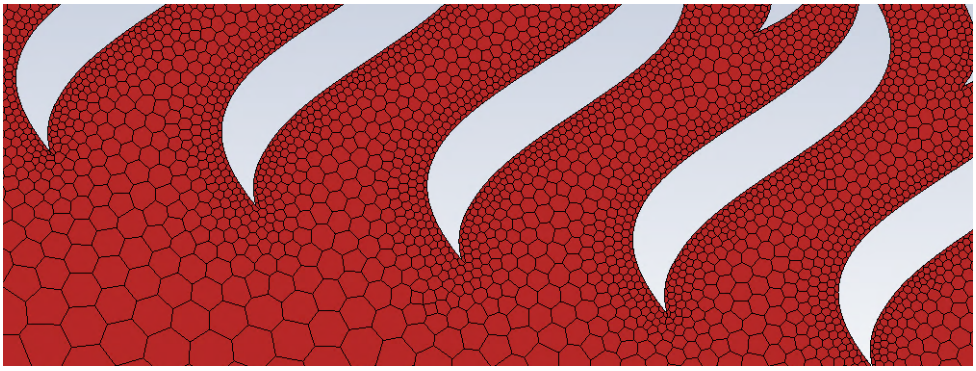

Figure 5.3: Polyhedral mesh of the fluid region

the software was not able to generate the prism layers near the fins. Therefore polyhedral mesh elements were used to mesh the geometry. Polyhedral meshes are generated in parallel in ANSYS Fluent, whereas tetrahedral meshes are generated in serial as of in ANSYS 2021R2. Meshing in parallel greatly reduces the mesh generation time. The mesh on the a face in the fluid region is shown in Fig. 5.3. Conformal meshes are generated between the fluid and solid regions to reduce the computational time. The mesh is generated to maintain a $y^+ < 5$ for the highest Reynolds number.

### 5.2.2 Modelling

This is a conjugate heat transfer simulation. The heat flux is applied at every heater as a boundary condition. Pressure inlet boundary condition is used to specify the pressure and temperature in the inlet. Mass-flow outlet is mentioned at the outlet. All internal walls (in contact with other surfaces) are set to coupled boundary condition to account for conjugate heat transfer. All external walls (not attached to other surfaces) are set to

Table 5.1: Material Properties

| Material | Density ($kg/m^3$) | Thermal conductivity W/m $\cdot$ °C | Specific heat J/kg°C |
|---|---|---|---|
| Aluminium | 2719 | 202 | 871 |
| Rubber | 1300 | 0.25 | 1350 |
| Ti-6Al-4V | 4430 | 6.7 | 526.3 |

zero heat flux (fully insulated).

ANSYS Fluent has the in-built NIST Refprop database which has the thermal properties for many fluids. Air is the working fluid in these simulations, and the NIST Refprop is used to generate the thermal properties. The material properties of the solid are tabulated in Table 5.1.

The simulations are carried for a range of Reynolds number varying from 1000 - 8000. For lower Reynolds number (less than 2500) are in the laminar regime and no turbulence model is used. The $k-\omega$ SST turbulence model is used to model the fluid flow for higher Reynolds number flow.

Constant heat flux boundary conditions are used on the heater surfaces. The resistance of the heaters was measured in the lab by the experimental team and the voltage applied to each heater was also given. Using this information, the heat flux from the surface is calculated in $W/m^2$. The heat provided to the heaters for different Reynolds numbers are given in Table 5.2.

The results are compared with the experimental data provided by the team. Nusselt number ($Nu$) and friction factor ($f$) are compared. The Nusselt number is calculated using Equation 5.5 and the friction factor is calculated using Equation 5.6.

$$\Delta T_{in} = T_{surface,in} - T_{fluid,in} \tag{5.1}$$

$$\Delta T_{out} = T_{surface,out} - T_{fluid,out} \tag{5.2}$$

$$\Delta T_{LM} = \frac{\Delta T_{in} - \Delta T_{out}}{ln\left(\frac{\Delta T_{in}}{\Delta T_{out}}\right)} \tag{5.3}$$

Table 5.2: Heat flux boundary condition

| Re | Heater 1 ($W/m^2$) | Heater 2 ($W/m^2$) | Heater 3 ($W/m^2$) | Heater 4 ($W/m^2$) | Heater 5 ($W/m^2$) | Heater 6 ($W/m^2$) | Heater 7 ($W/m^2$) |
|---|---|---|---|---|---|---|---|
| 1202.31 | 4148.73 | 4090.19 | 4140.27 | 4098.45 | 4140.27 | 4090.19 | 4140.27 |
| 1605.31 | 5732.59 | 5651.70 | 5720.90 | 5663.11 | 5720.90 | 5651.70 | 5720.90 |
| 1997.41 | 7061.91 | 6962.25 | 7047.50 | 6976.31 | 7047.50 | 6962.25 | 7047.50 |
| 2382.65 | 8667.040 | 8544.72 | 8649.35 | 8561.99 | 8649.35 | 8544.72 | 8649.35 |
| 2789.73 | 10179.09 | 10035.44 | 10158.32 | 10055.71 | 10158.32 | 10035.44 | 10158.32 |
| 3196.76 | 11649.50 | 11485.10 | 11625.73 | 11508.30 | 11625.73 | 11485.10 | 11625.73 |
| 3624.65 | 12737.85 | 12558.09 | 12711.86 | 12583.46 | 12711.86 | 12558.09 | 12711.86 |
| 4064.26 | 13701.38 | 13508.02 | 13673.42 | 13535.31 | 13673.42 | 13508.02 | 13673.42 |
| 2795.72 | 10191.62 | 10047.79 | 10170.82 | 10068.09 | 10170.82 | 10047.79 | 10170.82 |
| 3209.10 | 11698.24 | 11533.15 | 11674.37 | 11556.45 | 11674.37 | 11533.15 | 11674.37 |
| 3607.32 | 13163.80 | 12978.03 | 13136.94 | 13004.25 | 13136.94 | 12978.03 | 13136.94 |
| 4060.42 | 13792.59 | 13597.94 | 13764.45 | 13625.41 | 13764.45 | 13597.94 | 13764.45 |
| 4442.05 | 13865.06 | 13669.39 | 13836.77 | 13697.01 | 13836.77 | 13669.39 | 13836.77 |
| 4878.15 | 13915.37 | 13718.99 | 13886.98 | 13746.70 | 13886.98 | 13718.99 | 13886.98 |
| 5308.06 | 13907.43 | 13711.16 | 13879.05 | 13738.86 | 13879.05 | 13711.16 | 13879.05 |
| 5742.00 | 13967.39 | 13770.27 | 13938.89 | 13798.09 | 13938.89 | 13770.27 | 13938.89 |
| 6205.07 | 14162.94 | 13963.07 | 14134.04 | 13991.27 | 14134.04 | 13963.07 | 14134.04 |
| 6629.82 | 14034.59 | 13836.53 | 14005.96 | 13864.48 | 14005.96 | 13836.53 | 14005.96 |
| 7053.83 | 14096.18 | 13897.24 | 14067.41 | 13925.32 | 14067.41 | 13897.24 | 14067.41 |
| 7493.38 | 14165.13 | 13965.22 | 14136.23 | 13993.44 | 14136.23 | 13965.22 | 14136.23 |
| 7937.95 | 14084.36 | 13885.60 | 14055.63 | 13913.65 | 14055.63 | 13885.60 | 14055.63 |
| 8271.58 | 14325.67 | 14123.50 | 14296.44 | 14152.03 | 14296.44 | 14123.50 | 14296.44 |

$$U = \frac{\dot{m} C_p (T_{fluid,out} - T_{fluid,in})}{\Delta T_{LM} A_{HX}} \tag{5.4}$$

$$Nu = \frac{U D_h}{k_{fluid}} \tag{5.5}$$

$$f = \Delta P \frac{\rho D_h A_C^2}{2L\dot{m}} \tag{5.6}$$

The surface and fluid temperatures are obtained from 7 different locations in the plate heat exchanger. The solid probes are placed 1.6 mm from the bottom of the plate and the fluid probes are placed at the interface of the fluid and solid at the top surface. The calculation of Nu and f in CFD follows the same procedure as in the experiments.

### 5.2.3 Results

The simulations are carried out for various Reynolds number ranging from 1000 - 8000. This Reynolds number is lower than the Reynolds number range for the full scale heat exchanger. The Nusselt number and friction factor for the finned and flat plate are shown in Fig. 5.4.

The Nusselt number for the finned plate is under-predicted compared to experiments by about 35-38% at all Reynolds number, whereas for the flat plate, the Nusselt number is much better predicted and the maximum error observed is 18%. There could be 2 reasons for the high mismatch in the Nusselt number prediction for the finned plate: 1. Turbulence modelling and 2. Surface roughness. This has been studied by Garg *et al.* [90]. In the study by Garg *et al.*, they have documented the increase in the Nusselt number and friction factor for additively manufactured surfaces. They found that due to roughness, they had 1.2-3 times enhancement in heat transfer compared to smooth pipes. The additive manufacturing used in that study is Laser Powder Bed Fusion with material IN939. The roughness on the sides of the fins also increases the friction factor which is seen in Fig. 5.4c. These trends are not that pronounced in the flat plate case.

The probe temperatures are measured at different locations in the domain and are presented in Fig. 5.5. The solid probes in the flat plate case are within 1% percent error with the experimental data which is within experimental measurement error. The solid

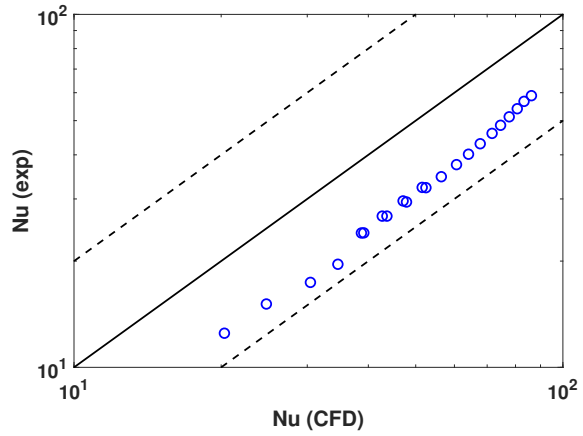


(a) Nusselt number - finned

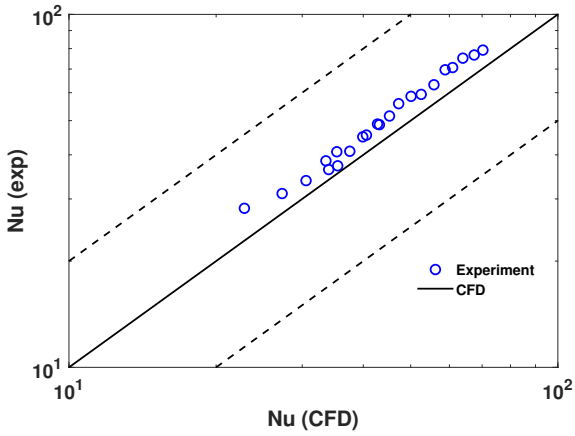


(b) Nusselt number - flat plate

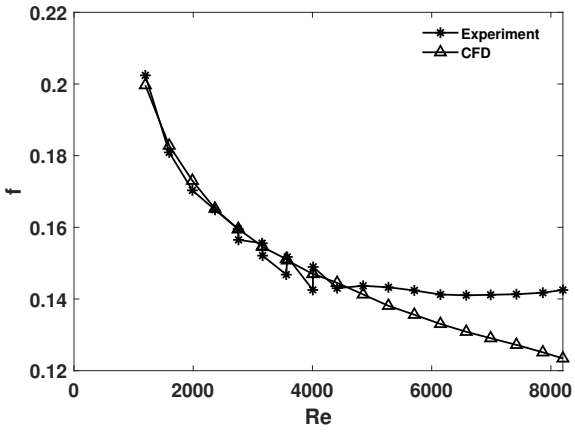


(c) Friction factor - finned

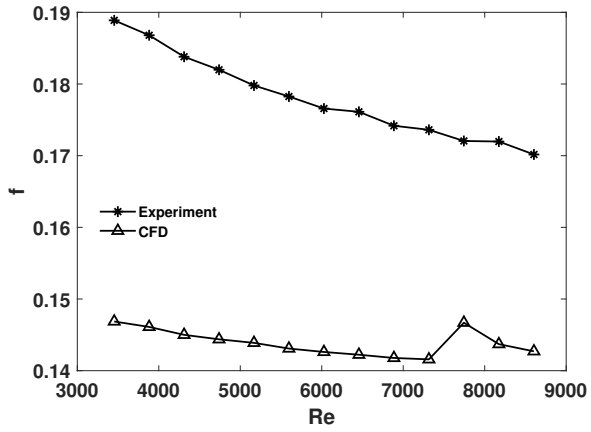


(d) Friction factor - flat plate

Figure 5.4: Performance of single plate - Nu and f

probe temperatures for the finned case has a higher mismatch with the experimental data with the maximum mismatch for the Probe 1, which is near the inlet. The bounds drawn with dashed lines in all the figures correspond to 7% from the ideal value. The fluid probe data has a greater spread because it was not possible to know exactly where the probe was placed in the fluid.

The temperature difference between inlet and outlet, and the pressure drop between inlet and outlet is shown in Fig. 5.6. The temperature difference is captured well by CFD and the maximum difference with experiments is 2% in the finned case. We also get a good prediction of dT for the flat plate case. The pressure drop has a maximum error of 12% for the finned case.

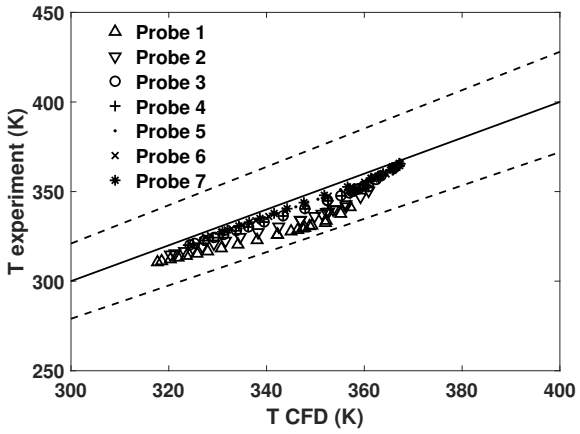


(a) Solid probes - finned

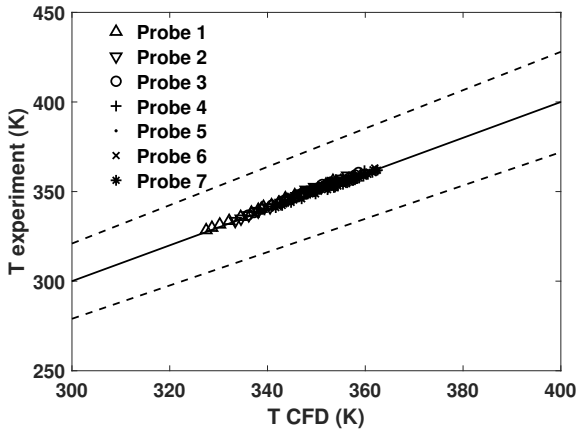


(b) Solid probes - flat plate

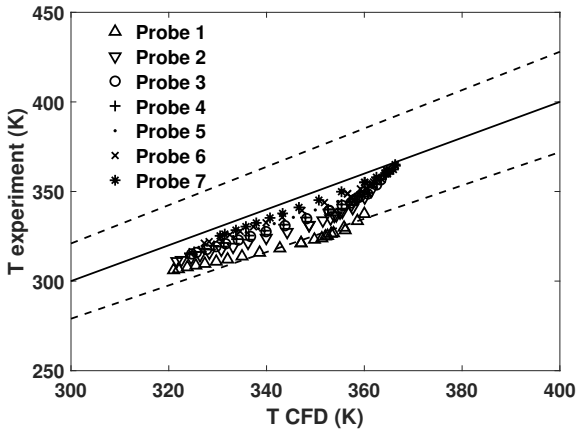


(c) Fluid probes - finned

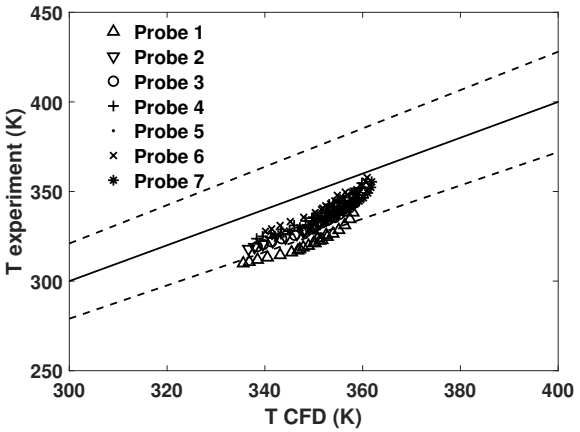


(d) Fluid probes - flat plate

Figure 5.5: Performance of single plate - temperature probes

## 5.3 Design of High Temperature Heater

A custom heater is required to be designed for the testing the full scale heat exchangers at high temperatures (800$^o$C - 900$^o$C). A heater has been designed by the experimental team using graphite. Testing these heaters for different test conditions is very difficult and expensive. To aid in capturing the performance of the heater, CFD simulations are used to study the performance of the graphite heater. The graphite heater has been machined using wire EDM.

### 5.3.1 Geometry

The geometry of the heater is shown in Fig. 5.7. The heater is designed in a way to have maximum heat transfer area. The heater is enclosed in an aluminium sheath and the

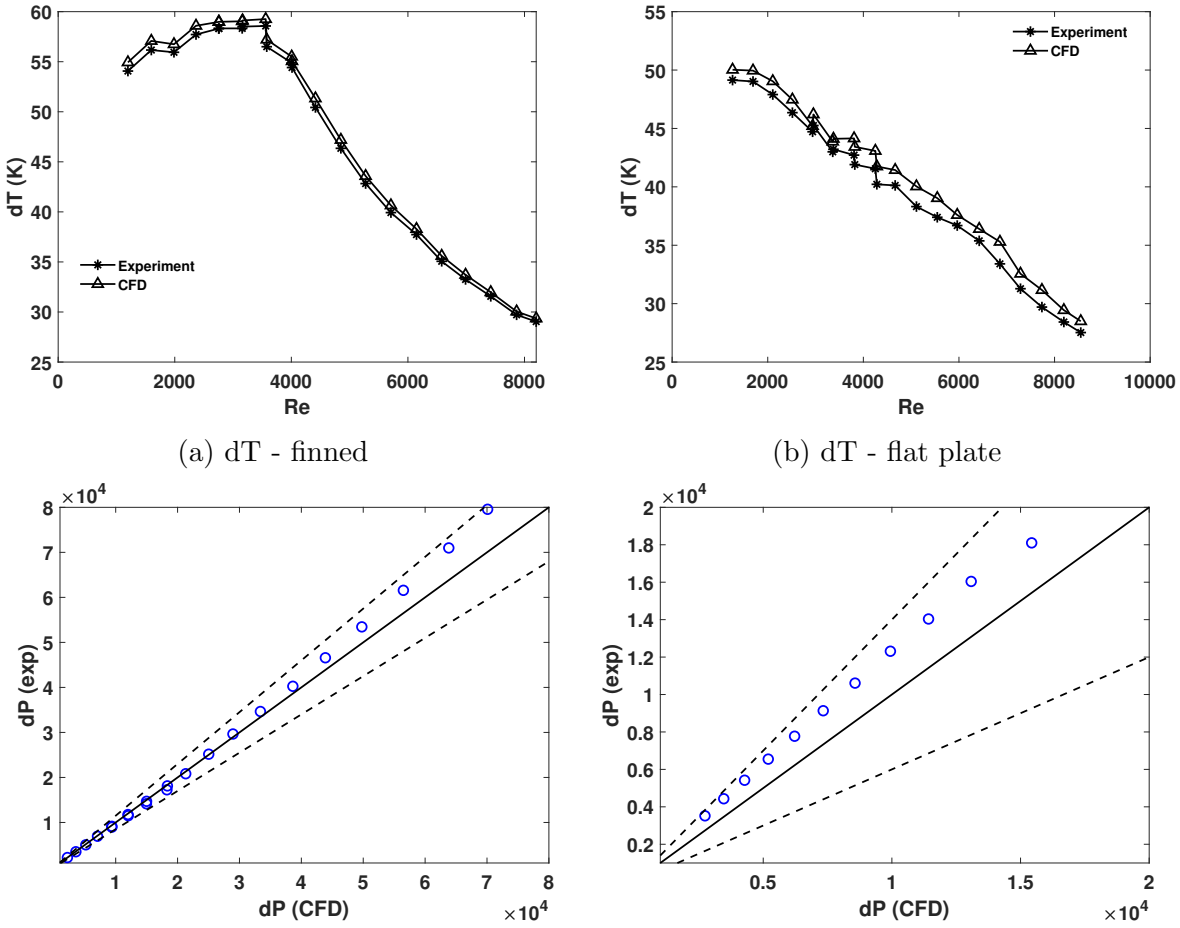


(a) dT - finned

(b) dT - flat plate

(c) dP - finned

(d) dP - flat plate

Figure 5.6: Performance of single plate - dT and dP

entire assembly is covered by insulation.

The mesh for this geometry is generated using ANSYS Fluent 2021R2. Polyhedral mesh with prism layers to maintain the $y^+ < 5$. The computational domain of the geometry is shown in Fig. 5.8. The inlet is on the right side of the image and the outlet on the left side. The heater is placed in the centre of the computational domain, insulated.

### 5.3.2 Modelling

The heater works on the principle of Joule's heating. For measuring the performance of the graphite heater, it is required to model the electric potential in the heater. An additional equation is solved for the electric potential in addition to the Navier-Stokes and energy equation. The turbulence modelling is done using the $k - \omega$ SST turbulence

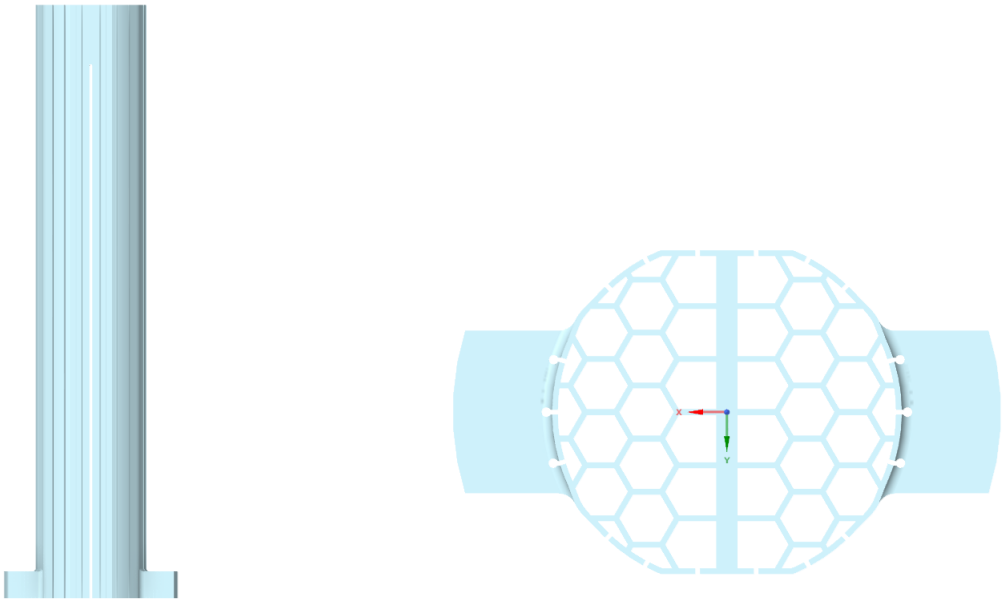

(a) Front View (b) Top View

Figure 5.7: Graphite heater

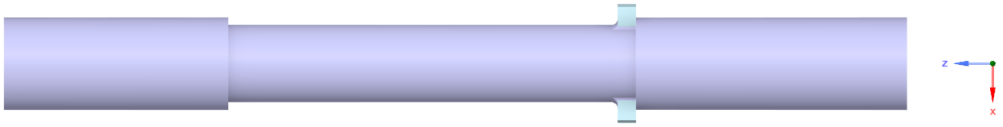

Figure 5.8: Computational domain for the heater

model.

$$\frac{\partial \overline{u}_i}{\partial x_i} = 0 \tag{5.7}$$

$$\overline{u_j}\frac{\partial \overline{u_i}}{\partial x_j} = -\frac{1}{\rho}\frac{\partial \overline{p}}{\partial x_i} + \frac{\partial}{\partial x_j}\left[(\nu + \nu_\mathrm{t})\frac{\partial \overline{u}_i}{\partial x_j}\right] \tag{5.8}$$

$$\overline{u_j}\frac{\partial \overline{T}}{\partial x_j} = \frac{\partial}{\partial x_j}\left[\left(\frac{\nu}{\mathrm{Pr}} + \frac{\nu_\mathrm{t}}{\mathrm{Pr}_\mathrm{t}}\right)\frac{\partial \overline{T}}{\partial x_j}\right] + S_h \tag{5.9}$$

$$\frac{\partial}{\partial x_j}\left[\sigma\frac{\partial \phi}{\partial x_j}\right] + S = 0 \tag{5.10}$$

$S_h$ is the source term in the energy equation (Equation 5.9) for Joule's heating. The term is defined as: $S_h = \sigma|\nabla\phi|^2$.

Pressure inlet boundary condition is used at the inlet to specify the inlet pressure and fluid temperature at the inlet. Mass flow outlet boundary condition is used at the

outlet. The leads of the heater are given constant potential. 12V is provided to the positive terminal and 0V is provided to the negative terminal. The outer walls of the computational domain are insulated.

Nitrogen is the working fluid in the simulations. Since the pressure drop across the heater is very less (approximately 100 Pa), only temperature dependent properties are used for the fluid. Polynomial fitting is used to get properties of the fluid: density, viscosity, specific heat and thermal conductivity of the fluid. The solid material has constant properties as we are solving for steady state temperature distribution on the heater. The resistivity of the heater is the most important parameter. The resistivity for the graphite heater is measured in-house and used in these simulations. The elctrical conductivity of the fluid does not play a major role in these simulations.

### 5.3.3 Results

Steady-state simulations are run to get the temperature profile of the graphite heater and the outlet temperature of the domain. The outlet of this heater is used as the inlet for hot side of the heat exchanger.

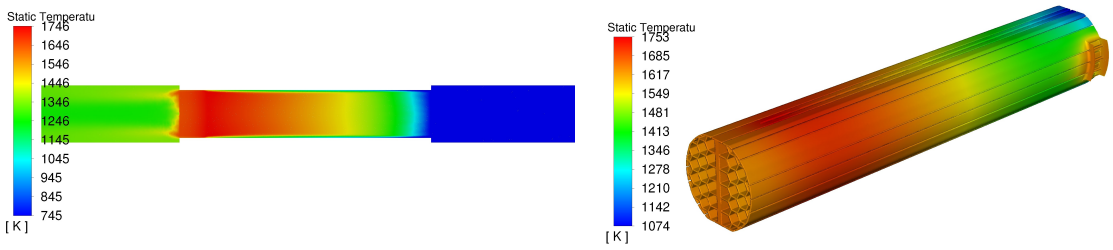


(a) Temperature contour of the middle plane (b) Temperature contour of the graphite heater

Figure 5.9: Temperature contour

The simulations are run for a mass flow rate of 0.006866 kg/s at 25.3 bar. The area-averaged temperature at the inlet is 745 K and the area-averaged temperature at the outlet is 1301.278 K. An increase of 556 K is observed. The outlet temperature calculated from experiments at the centre of the outlet patch is 1207 K and from CFD it is 1256.7588. The error between the CFD prediction and experiment is 4.11%. This shows that CFD is able to predict the performance of the heater.

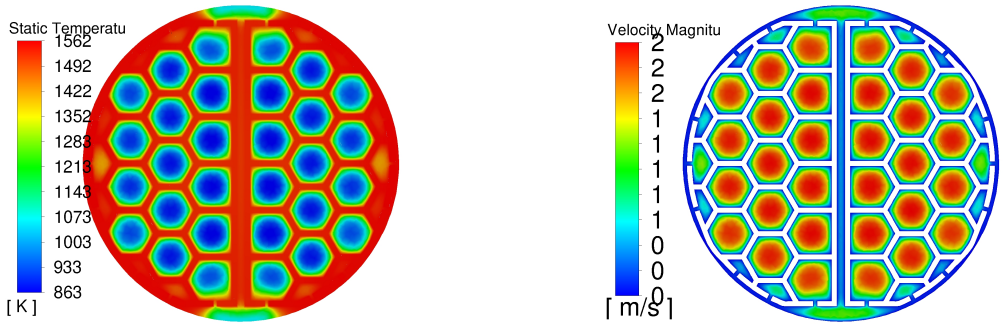


(a) Temperature contour (b) Velocity contour

Figure 5.10: Contours at the centre of the heater

## 5.4 Full scale heat exchanger simulations

In this section, we discuss the performance of heat exchangers that are designed for high temperature and high pressure applications. The operating temperatures in the heat exchanger vary from $300^oC$ to $1100^oC$. The materials considered for the heat exchangers is Haynes 214. The properties of the material is taken from the Haynes 214 brochure [91]. The properties are given in Table 5.3.

The datasheet provided by Haynes International does not contain the Youngs modulus which is necessary for doing Thermo-Mechanical simulations. The Youngs modulus data at various temperatures can be obtained from these published sources [92]. The data obtained is for rolled and subsequently solution heat-treated strips. The data is shown in Table 5.4. The data might vary with additively manufactured parts.

Table 5.3: Properties of Haynes 214

| Temperature | Expansion cofficient $\times 10^{-6}$°C | Thermal conductivity W/m · °C | Specific heat J/kg°C |
|---|---|---|---|
| 20 | – | 12 | 452 |
| 100 | – | 12.8 | 470 |
| 200 | 13.3 | 14.2 | 493 |
| 300 | 13.6 | 15.9 | 515 |
| 400 | 14.1 | 18.4 | 538 |
| 500 | 14.6 | 21.1 | 561 |
| 600 | 15.2 | 23.9 | 611 |
| 700 | 15.8 | 26.9 | 668 |
| 800 | 16.6 | 29.7 | 705 |
| 900 | 17.6 | 31.4 | 728 |
| 1000 | 18.6 | 32.7 | 742 |
| 1100 | 20.2 | 34.0 | 749 |

Table 5.4: Themo-physical properties of Haynes 214

| Temperature ($^oC$) | E (GPa) | G (GPa) | $\nu$ |
|---|---|---|---|
| 20 | 217.2 | 83.2 | 0.305 |
| 50 | 212.4 | 81.0 | 0.312 |
| 100 | 209.8 | 80.0 | 0.311 |
| 150 | 206.5 | 78.6 | 0.314 |
| 200 | 202.5 | 76.7 | 0.319 |
| 250 | 199.3 | 75.8 | 0.314 |
| 300 | 195.9 | 74.5 | 0.315 |
| 350 | 191.6 | 72.5 | 0.321 |
| 400 | 188.1 | 70.9 | 0.327 |
| 450 | 185.5 | 70.1 | 0.324 |
| 500 | 182.2 | 68.7 | 0.326 |
| 550 | 179.2 | 67.6 | 0.326 |
| 600 | 174.9 | 65.6 | 0.333 |
| 650 | 171.2 | 64.2 | 0.334 |
| 700 | 165.7 | 62.1 | 0.335 |
| 750 | 163.1 | 61.1 | 0.336 |
| 800 | 159.1 | 59.6 | 0.335 |
| 850 | 153.6 | 57.3 | 0.339 |
| 900 | 151.2 | 56.3 | 0.343 |
| 950 | 144.5 | 54.7 | |
| 1000 | 139.2 | 50.0 | |

### 5.4.1 Geometry Description

The plate frame heat exchangers are designed for two configurations: Cold-Hot-Cold (CHC) and Cold-Hot (CH). The plate thickness is chosen to be 4 mm and the the fin thickness is 1 mm. The inlet and outlet holes are located 15.53 mm from the edges of the plate. This dimension is chosen to accommodate for the experimental apparatus present in the university and also for sealing. The inlet and outlet in the top and bottom plates need to be sealed to the flanges to avoid leakages. The CAD drawing of the CHC is shown in Figure 5.11 and that of CH configuration is shown in Figure 5.12.

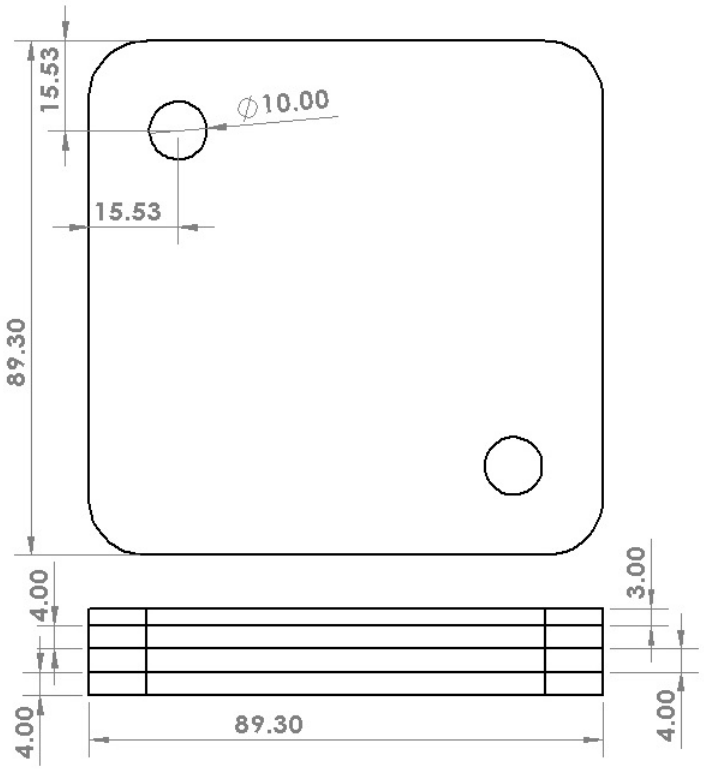


Figure 5.11: CHC configuration heat exchanger (in mm)

The heat exchanger is designed to have a capacity of 50 KW. To achieve this the plates are stacked up in their respective configurations and the necessary capacity is reached. The stacked up heat exchanger is shown for the CHC combination in Figure 5.13. The fin shapes in the heat exchanger is not optimized and the pitch of the fin distributions in the x and y direction is based on existing literature and has not been optimized for the current geometry. The fin shape and pitch length will be optimized in the next part of

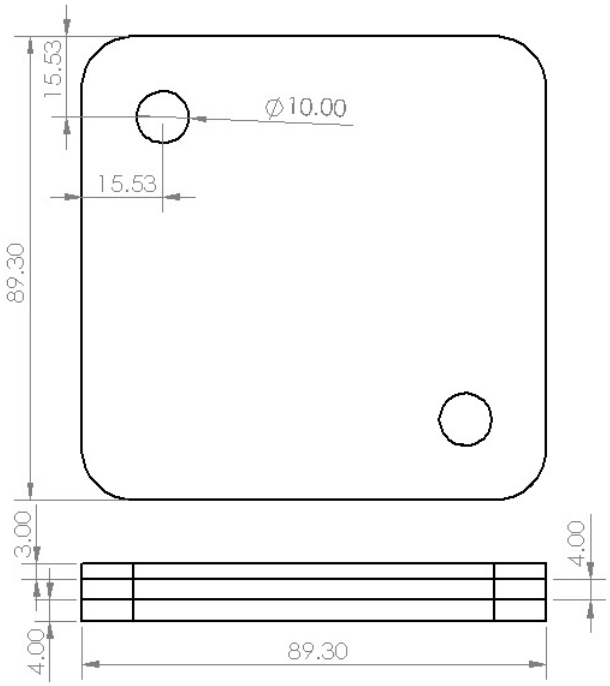


Figure 5.12: CH configuration heat exchanger (in mm)

the project.

### 5.4.2 Simulations

#### CFD Simulations

The CFD simulations are run in ANSYS Fluent. The inlet mass flow rate is fixed at 0.007 kg/s. The Reynolds number corresponding to the inlet mass flow rate is 8625.783 on the hot side and 13831.828 on the cold side based on the diameter of the inlet and outlet. The boundary conditions used are displayed in Table 5.5. The MNIST database is used to get the properties of $CO_2$. A lookup table is created within ANSYS Fluent using the in-built MNIST database to get the properties of the fluid. The properties of the solid material are given as in Table 5.3 and piecewise-linear.

The mesh is generated using ICEM CFD. Unstructured volume meshing is used to create the mesh. The $y^+$ values near the fins is maintained between 10-30. $k-\omega$ SST turbulence model is used to describe the turbulent flow field. The $y^+$ values obtained are acceptable if wall functions are used along with the turbulence models. The Energy

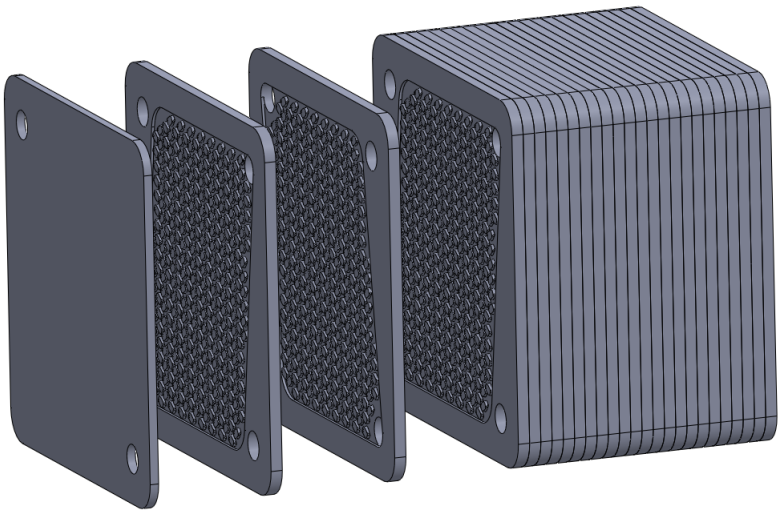

Figure 5.13: Exploded view of the staked up heat exchanger

Table 5.5: Boundary conditions

| **Patch/Surface** | **Boundary condition** |
|---|---|
| Hot Inlet | Pressure Inlet (8 MPa and 1373 K) |
| Cold Inlet | Pressure Inlet (25 MPa and 573 K) |
| Hot Outlet | Mass flow outlet (0.007 kg/s) |
| Cold Outlet | Mass flow outlet (0.007 kg/s) |
| External walls | Adiabatic walls |
| Internal walls and fins | No slip and Coupled wall for heat transfer |

equation is solved for heat transfer. Steady State simulations are used. The simulations are run till convergence of 0.001 is obtained in the continuity, momentum and energy equations.

The outlet temperature and pressure drop across the heat exchangers is calculated. The power capacity of the heat exchanger is also calculated. The power is calculated using the following the formula:

$$Q = \dot{m}(h_{in} - h_{out}) \tag{5.11}$$

where $\dot{m}$ is the mass flow rate in kg/s and $h$ is the enthalpy of the fluid in J/kg. The enthalpy of the fluid is also calculated using the MNIST database in ANSYS Fluent.

**Mesh Independence Study**

Table 5.6: Mesh independence

| Parameters | Mesh 1 | Mesh 2 | Mesh 3 | Mesh 4 | Mesh 5 |
|---|---|---|---|---|---|
| Number of cells | 6,228,924 | 13,082,814 | 17,762,678 | 33,395,894 | 70,829,479 |
| y+ | 18-32 | 15-25 | 10-20 | 8-15 | 6-11 |
| $\Delta P_{Hot}$ (kPa) | 38.1931 | 37.190 | 36.836 | 37.089 | 39.8951 |
| $\Delta P_{Cold}$ (kPa) | 3.466 | 3.546 | 3.643 | 3.877 | 4.258 |
| $\Delta T_{Hot}$ | 356.2057 | 362.4732 | 380.361 | 401.8403 | 411.8797 |
| $\Delta T_{Cold}$ | 379.1651 | 385.7156 | 396.624 | 415.978 | 428.1011 |
| Power (KW) | 3.25 | 3.38 | 3.48 | 3.61 | 3.73 |

### 5.4.3 Results

The plate heat exchangers are tested for various designs and sizes. The geometrical size is varied keeping in mind the constraints from manufacturing. The simulations are run for a range of sizes and the results are tabulated in Table 5.7 and 5.8. All the plates are made to have the same fin design and arrangement to study only the effect of the different geometrical configurations.

The specific power (Power/Mass) decreases with increased size of geometry. The C-H configuration provides higher specific power compared to the C-H-C configuration, but the pressure drop in the cold side is much higher compared to the C-H-C configuration.

Table 5.7: Different Designs 1

| Parameters | Design 1 | Design 2 | Design 3 | Design 4 | Design 5 |
|---|---|---|---|---|---|
| Dimension | 90 mm x 90 mm | 100 mm x 100 mm | 110 mm x 110 mm | 125 mm x 125 mm | 90 mm x 90 mm |
| Configuration | C/H/C | C/H/C | C/H/C | C/H/C | C/H |
| $\Delta P_{hot}$ (kPa) | 30.6351 | 36.429 | 34.596 | 29.287 | 31.4106 |
| $\Delta P_{cold}$ (kPa) | 3.888 | 3.443 | 3.480 | 2.772 | 14.834 |
| $\Delta T_{hot}$ (K) | 347.3908 | 384.1103 | 414.9515 | 461.2647 | 311.7672 |
| $\Delta T_{cold}$ (K) | 364.7999 | 402.1847 | 439.9473 | 474.0436 | 315.981 |
| Power (KW) | 3.2 | 3.4 | 3.8 | 4.2 | 2.8 |
| Mass (kg) | 0.8722 | 1.0984 | 1.3317 | 1.5358 | 0.6439 |
| Volume ($m^3$) | 0.0001083 | 0.000136 | 0.0001654 | 0.0001907 | 0.00007998 |
| A ($m^2$) | 0.02028 | 0.02717 | 0.03476 | 0.04793 | 0.01369 |
| U ($W/m^2K$) | 489.5181 | 647.2350 | 393.0789 | 234.2732 | 500.1031 |
| UA ($W/K$) | 9.9274 | 17.5854 | 13.6635 | 11.2287 | 6.8464 |
| Number of plates (Hot/Cold) | 16/32 | 15/30 | 14/28 | 12/24 | 18/18 |
| Mass (kg) | 11.075 | 13.103 | 14.8527 | 16.5144 | 8.3488 |
| Volume ($m^3$) | 0.001375 | 0.001627 | 0.001845 | 0.002051 | 0.001037 |
| Power/Mass (KW/kg) | 4.5146 | 3.8156 | 3.3663 | 3.0276 | 5.9888 |
| Power/Volume (KW/$m^3$) | 36363.63 | 30731.4 | 27100.27 | 24378.35 | 48216 |
| Power/UA ($K$) | 5036.5654 | 2843.26 | 3659.38 | 4452.87 | 7303.1 |

Table 5.8: Different Designs 2

| Parameters | Design 6 | Design 7 | Design 8 | Design 9 |
|---|---|---|---|---|
| Dimension | 125 mm x 62.5 mm | 100 mm x 100 mm | 125 mm x 125 mm | 80 mm x 80 mm |
| Configuration | C/H/C | C/H | C/H | C/H/C |
| $\Delta P_{hot}$ (kPa) | 63.046 | 42.0021 | 30.814 | 42.711 |
| $\Delta P_{cold}$ (kPa) | 4.013 | 14.141 | 10.696 | 2.589 |
| $\Delta T_{hot}$ (K) | 321.3259 | 356.456 | 424.0308 | 307.9151 |
| $\Delta T_{cold}$ (K) | 324.543 | 377.294 | 442.8071 | 318.9162 |
| Power (KW) | 2.9 | 3.3 | 3.9 | 2.8 |
| Mass (kg) | 0.8583 | 0.811 | 1.2718 | |
| Volume ($m^3$) | 0.0001066 | 0.0001007 | 0.0001579 | |
| A ($m^2$) | 0.01747 | 0.01825 | 0.03217 | 0.0148 |
| U ($W/m^2K$) | 423.2571 | 613.9139 | 456.7999 | 461.8864 |
| UA ($W/K$) | 7.3943 | 11.2043 | 14.695 | 6.8359 |
| Number of plates (Hot/Cold) | 18/36 | 15/15 | 13/13 | 18/36 |
| Mass (kg) | 12.253 | 8.8162 | 12.029 | |
| Volume ($m^3$) | 0.001522 | 0.0011 | 0.001494 | |
| Power/Mass (KW/kg) | 4.0806 | 5.64256 | 4.1566 | |
| Power/Volume (KW/$m^3$) | 32851.51 | 45454.545 | 33467.2021 | |
| Power/UA ($K$) | 6761.9 | 4462.5 | 3402.5178 | 7.3143 |

**Scaling up**

Table 5.9: Large scale HX simulations

| Parameters \Number of plates | 1 set | 5 set | 10 set | 18 set |
|---|---|---|---|---|
| Configuration | C/H | C/H | C/H | C/H |
| Dimensions | | 100 x 100 x 43 | 100 x 100 x 83 | 100 x 100 x 147 |
| Mass flow rate (kg/s) | 0.007 | 0.035 | 0.07 | 0.126 |
| $\Delta P_{hot}$ (kPa) | 42.0021 | 39.2187 | 46.536 | 65.3604 |
| $\Delta P_{cold}$ (kPa) | 14.141 | 13.375 | 15.741 | 24.597 |
| $\Delta T_{hot}$ (K) | 356.456 | 364.1612 | 369.517 | 364.1432 |
| $\Delta T_{cold}$ (K) | 377.294 | 370.7624 | 376.074 | 372.032 |
| Power (KW) | 3.3 | 16.24 | 33.1 | 59.45 |
| Mass (kg) | 0.811 | 3.0989 | 5.958 | 10.5335 |
| Volume ($m^3$) | 0.0001007 | 0.0003849 | 0.0007401 | 0.001308 |
| A ($m^2$) | 0.01825 | 0.09004 | 0.1797 | 0.3233 |
| U ($W/m^2K$) | 613.9139 | 615.7687 | 665.3 | 634.8958 |
| UA ($W/K$) | 11.2039 | 55.4438 | 119.5544 | 205.2618 |
| Power/Mass (KW/kg) | 4.069 | 5.2405 | 5.55 | 5.6438 |
| Power/Volume ($KW/m^3$) | 32770.605 | 42192.777 | 44723.685 | 45451.0703 |
| Power/UA (K) | 294.5402 | 292.909 | 276.8614 | 289.6301 |

**Influence of mass-flow rate**

This section discusses the effect of mass flow rate on the power rating of the heat exchanger. The Cold-Hot-Cold combination of plates is taken to discuss the results.

Table 5.10: Effect of mass flow rate

| Mass Flow Rate (kg/s) | Power (KW) | Power Density (KW/kg) |
|---|---|---|
| 0.007 | 3.4 | 3.09 |
| 0.0084 | 4.03 | 3.668 |
| 0.01 | 4.6 | 4.189 |
| 0.02 | 7.6 | 6.92 |
| 0.03 | 10.3 | 9.38 |
| 0.035 | 11.5 | 10.46 |

### Effectiveness and NTU

For calculating the effectiveness of the heat exchanger, we need the minimum of the specific heat ($C_p$) between the hot and cold side. The specific heat is minimum in the outlet of the hot side. The variation of Specific heat for $CO_2$ is shown in Figure 5.14.

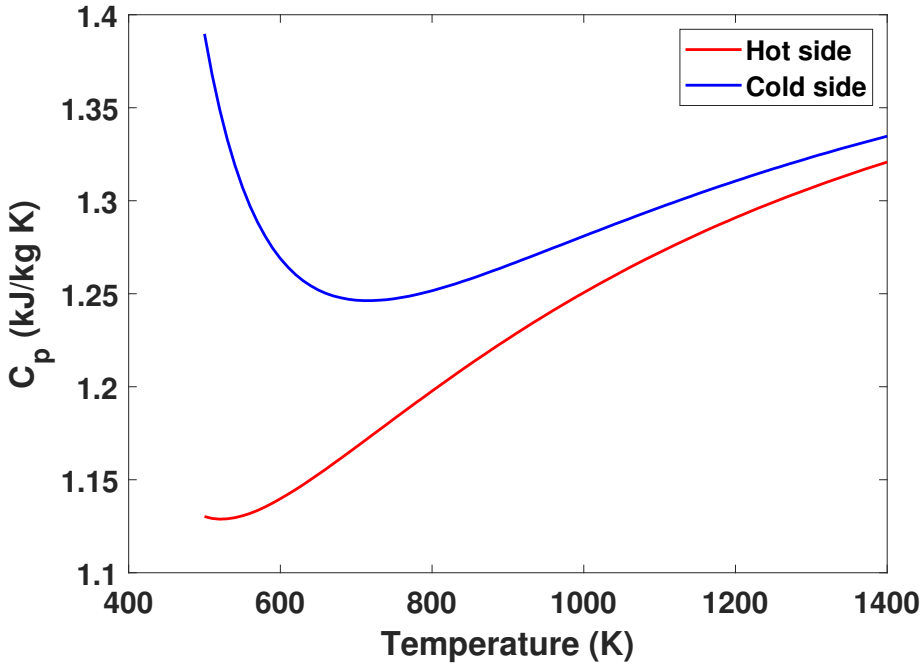


Figure 5.14: Specific Heat values for $CO_2$

To study the effectiveness of fins, 4 different designs with different angles of twist and different fin widths are chosen and studied at different mass flow rates to study the variation of effectiveness and power output. The different designs are shown in Figure 5.15. Two different angles of twist are chosen $20^o$ and $40^o$. Two different fin widths of 1.8 mm and 3.2 mm. The bigger fin width is chosen to provide more structural support to the system.

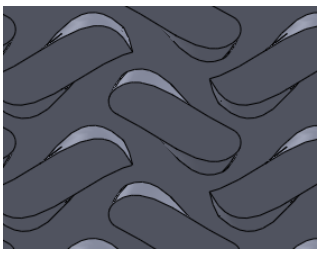

(a) Fin width, d 1.8 mm, Twist angle $20^o$

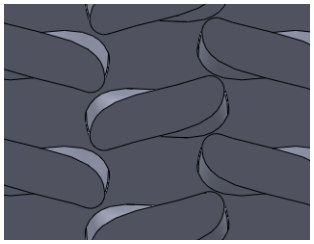

(b) Fin width, d 1.8 mm, Twist angle $20^o$ oriented vertical to flow

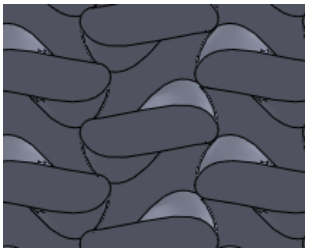

(c) Fin width, d 1.8 mm, Twist angle $40^o$

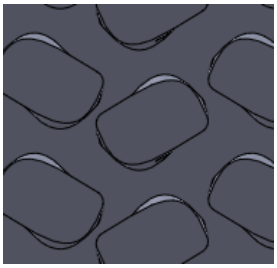

(d) Fin width, d 3.2 mm, Twist angle $20^o$

Figure 5.15: Different fin designs

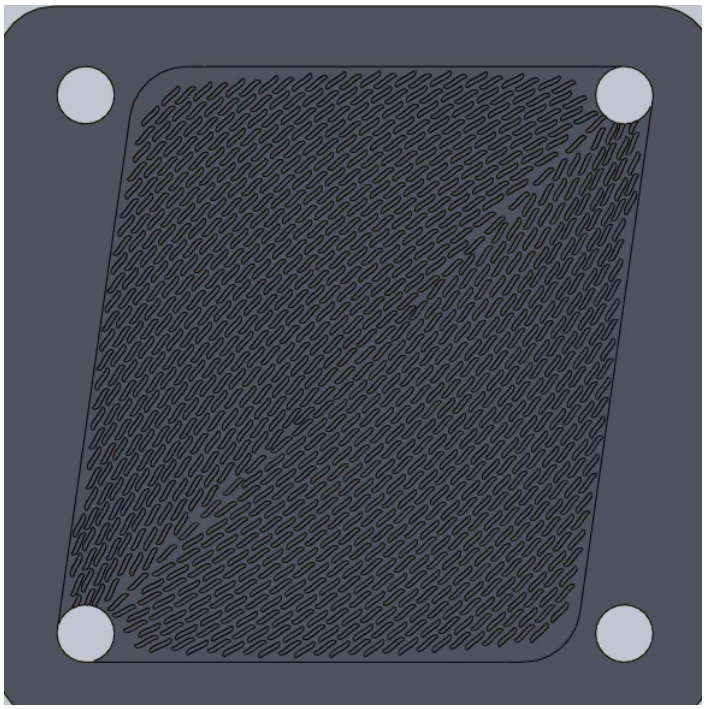

Figure 5.16: New arrangement of fins

Table 5.11: Effectiveness for 10 cm x 10 cm HX

| Fin shape | $\dot{m}_h$ (kg/s) | $\dot{m}_c$ (kg/s) | $T_{h,in}$ (K) | $dP_h$ (kPa) | $dP_c$ (kPa) | Specific Power ($KW/kg$) | Power Density ($KW/m^3$) | Power/UA | Effectiveness | NTU |
|---|---|---|---|---|---|---|---|---|---|---|
| Fin Width 3.2 mm, Twist Angle $20^o$ | 0.007 | 0.014 | 1173 | 32.91 | 43.46 | 47.38 | 35267.07 | 296.7 | 0.532 | 1.075 |
| | 0.007 | 0.02 | 1173 | 32.96 | 83.04 | 4.69 | 37732.01 | 309.1 | 0.569 | 1.104 |
| | 0.007 | 0.028 | 1173 | 33.19 | 153.94 | 5.04 | 40567.82 | 316.6 | 0.612 | 1.159 |
| | 0.009 | 0.027 | 1173 | 53.64 | 142 | 5.78 | 46522.18 | 339.4 | 0.545 | 0.964 |
| Fin Width 1.8 mm, Twist Angle $20^o$ | 0.009 | 0.027 | 1173 | 139.42 | 205.51 | 6.60 | 50734.50 | 313.8 | 0.591 | 1.131 |
| | 0.007 | 0.028 | 1173 | 84.77 | 206.61 | 5.36 | 43154.21 | 294.6 | 0.647 | 1.317 |
| | 0.007 | 0.035 | 1173 | 84.01 | 325.54 | 5.50 | 44266.97 | 300.7 | 0.663 | 1.323 |
| Fin Width 1.8 mm, Twist Angle $20^o$, vertical to flow | 0.007 | 0.028 | 1173 | 78.82 | 198.58 | 5.40 | 43452.35 | 289 | 0.651 | 1.351 |
| | 0.007 | 0.035 | 1173 | 79.06 | 294.85 | 5.5 | 44259.15 | 293.4 | 0.663 | 1.355 |
| | 0.009 | 0.045 | 1173 | 129.67 | 479.08 | 6.56 | 52772.65 | 321.2 | 0.615 | 1.148 |
| | 0.01 | 0.04 | 1173 | 164.48 | 393.22 | 7.13 | 57424.99 | 325.9 | 0.602 | 1.108 |
| | 0.01 | 0.05 | 1173 | 165.10 | 598.45 | 7.29 | 58715.19 | 325.7 | 0.615 | 1.134 |
| Fin Width 1.8 mm, Twist Angle $40^o$ | 0.007 | 0.035 | 1173 | 57.28 | 274.98 | 5.46 | 43931.02 | 302.8 | 0.658 | 1.303 |
| | 0.012 | 0.06 | 1173 | 176.97 | 788.01 | 8.24 | 66347.38 | 357.4 | 0.58 | 0.973 |

Table 5.12: Effectiveness for 12.5 cm x 12.5 cm HX

| Fin shape | $\dot{m}_h$ (kg/s) | $\dot{m}_c$ (kg/s) | $T_{h,in}$ (K) | $dP_h$ (kPa) | $dP_c$ (kPa) | Specific Power ($KW/kg$) | Power Density ($KW/m^3$) | Power/UA | Effectiveness | NTU |
|---|---|---|---|---|---|---|---|---|---|---|
| Fin Width 1.8 mm, Twist Angle $40^o$ | 0.007 | 0.035 | 1173 | 49.34 | 280.13 | 4.11 | 33116 | 207.9 | 0.775 | 2.236 |
| | 0.007 | 0.035 | 1373 | 55.78 | 290.68 | 5.6 | 45068.17 | 264.4 | 0.772 | 2.337 |
| | 0.007 | 0.042 | 1173 | 48.75 | 403.25 | 4.18 | 33656.63 | 214.0 | 0.788 | 2.208 |
| | 0.01 | 0.05 | 1173 | 99.43 | 622.53 | 5.43 | 43732.94 | 259.2 | 0.717 | 1.659 |
| | 0.012 | 0.06 | 1173 | 145.94 | 819.83 | 6.40 | 51537.01 | 274.1 | 0.704 | 1.540 |
| | 0.012 | 0.072 | 1173 | 144.79 | 1197.49 | 6.43 | 51746.94 | 282.9 | 0.707 | 1.498 |
| | 0.015 | 0.075 | 1173 | 232 | 1294.09 | 7.51 | 60488.03 | 302.4 | 0.661 | 1.311 |
| | 0.02 | 0.1 | 1173 | 427.95 | 2356.51 | 9.37 | 75443.06 | 334.7 | 0.618 | 1.108 |



Table 5.13: Effectiveness for new design 12.5 cm x 12.5 cm HX

| $\dot{m}_h$ (kg/s) | $\dot{m}_c$ (kg/s) | $T_{h,in}$ (K) | $dP_h$ (kPa) | $dP_c$ (kPa) | Specific Power ($KW/kg$) | Power Density ($KW/m^3$) | Power/UA | Effectiveness | NTU |
|---|---|---|---|---|---|---|---|---|---|
| 0.007 | 0.042 | 1173 | 25.3297 | 158.479 | 3.69 | 29711.59 | 304.77 | 0.691 | 1.361 |
| 0.02 | 0.02 | 1173 | 229.9244 | 41.623 | 5.23 | 42099.42 | 369.60 | 0.343 | 0.557 |
| 0.04 | 0.04 | 1173 | 982.7119 | 158.866 | 8.43 | 67845.00 | 429.15 | 0.276 | 0.386 |

The results of the fin designs are tabulated in Table 5.11 and Table 5.12. The mass flow rate on the cold side is deliberately made greater than on the hot side, because of the properties of Haynes 214. The thermal conductivity of Haynes 214 on the hot side is almost twice the thermal conductivity on the cold side. This configuration led to better effectiveness and NTU values.

Based on the above observations that pressure drop needs to be reduced, the fin arrangement is changed to mimic the streamline pattern in the plate. Figure 5.16 shows the new pattern of fins without a twist angle.

### Thickness of plates and Inlet Temperature

Table 5.14: Effect of plate thickness

| Dimension | 100 mm x 100 mm x 9 mm | 100 mm x 100 mm x 7 mm |
|---|---|---|
| Configuration | C/H/C | C/H |
| Mass flow rate (kg/s) | 0.007 | 0.007 |
| Inlet Temperature | 800 | 800 |
| $\Delta P_{hot}$ (kPa) | 29.625 | 31.54 |
| $\Delta P_{cold}$ (kPa) | 3.379 | 12.61 |
| $\Delta T_{hot}$ (K) | 225.14 | 214.33 |
| $\Delta T_{cold}$ (K) | 286.87 | 216.72 |
| Power (KW) | 2.3 | 1.98 |
| Mass (kg) | 0.8653 | 0.6554 |
| Volume ($m^3$) | 0.000107 | 8.1427e-05 |
| A ($m^2$) | 0.02685 | 0.01807 |
| U ($W/m^2K$) | 972.4576 | 483.0305 |
| UA ($W/K$) | 17.57 | 8.733 |
| Power/Mass (KW/kg) | 3.511 | 2.9 |
| Power/Volume ($KW/m^3$) | 28246.1 | 23337.8 |
| Power/UA (K) | 0.1308 | 0.2175 |

## 5.5 Conclusion and Future Work

In this chapter, the performance of a single plate, high temperature graphite heater and full scale heat exchanger are discussed. The CFD models used to predict the performance

was able to give a good approximation. A heat exchanger capable of operating for supercritical $CO_2$ cycles has also been proposed. The heat exchanger can operate at $800^o$ C inlet temperature on the hot side.

The single heat exchanger plate performance was well captured for the flat plate as the effects of roughness was minimal and the error in the Nusselt number prediction was in the range of 10%-18%. The prediction for the finned case was less accurate than the flat plate case. The error in the Nusselt number for the finned case was 30%-40%. The reason was the mismatch in the predictions by CFD and experiments can be attributed to: 1. Turbulence modelling and 2. Surface roughness. Surface roughness has been shown to increase heat transfer effectiveness. The friction factor prediction for the finned case was close to the experimental values. The maximum error observed was 14%. The friction for the unfinned case has an error of 27% for the lower Reynolds numbers.

The turbulent conjugate heat transfer simulation with potential equation has been solved to predict the performance of the graphite heater for high temperature application. The error in the outlet temperature prediction is 4%. This validates the numerical methodology used for this problem.

The performance of full-scale heat exchangers are computed for various mass flow rates, fin shapes and dimensions are calculated. An entire 50 KW heat exchanger with 200M cells is also computed and we find that the heat exchanger scales linearly as we increase the number of plates. The maximum performance for the assembly is observed when the mass flow rate on the cold side is about 6 times the mass flow rate on the hot side and this is because of the difference in the thermal conductivity of Haynes 214 on the hot side and cold side.

Two different configurations of assembly are studied and it is found that the CH combination is much efficient as less material is used. The maximum performance for the heat exchanger assembly observed is for the $40^o$ twisted fins in the 12.5 cm x 12.5 cm heat exchanger. The maximum specific power observed is 9.37 KW/kg with an effectiveness of 0.618 and NTU of 1.108. The pressure drop on the hot side is much higher than the cold side. Arranging the fins along the streamline helps in reducing the pressure drop.

# Chapter 6

## Summary, Conclusion and Future Work

This work focuses on the workings of two different types of industrial equipment which operate in the turbulent regime. CFD simulations are used to understand the working of these equipment and design modifications are proposed for improved performance of the equipment.

Cyclone separators are used for separating the solid phase from the gaseous phase. Hybrid turbulence models are studied to check their applicability for swirling flows. Mean flow quantities and Reynolds stress predictions from the hybrid turbulence models match the experimental data available in the literature. Using hybrid turbulence models will drastically reduce the computational time and resources required. Lagrangian particles are then injected into the mean turbulent flow. The lagrangian motion of particles is studied in LES. Based on the observation of the hydrodynamics, there are vortices in the sharp corners at the roof of the cyclone separators. Particles get stuck in these vortices and tend to continuously erode the surface. A design modification is proposed to introduce fillets in the roof of the cyclone separator to reduce the vortices forming at the roof. The introduction of the fillets reduces the overall erosion of the cyclone separator. Major reductions are seen in the roof of the cyclone separator, but there is a slight increase in the erosion in the cone region of the cyclone separator.

Novel 3D twisted S-shaped fins are designed for plate heat exchangers. These heat exchangers are to be used in the next generation supercritical $CO_2$ power plants. There is always a need to improve the performance of heat exchangers to reduce the pumping requirement without losing heat transfer performance. Instead of simulating the entire plate of the heat exchanger, a representative periodic domain is chosen to reduce the computational time for studying more designs. Periodic heat transfer with turbulence modelling is used to gather data on the performance of the 3D twisted S-shaped fins. The 3D twisted S-Shaped fins provide almost 75% reduction in the pumping requirement with improved performance efficient coefficient of 10%-13%.

Experimental data for a single plate heat exchanger is available. The results from the

CFD simulations are compared with the experimental data. There is a mismatch of 35%-38% in the Nusselt number prediction for the finned case. This can be due to 2 different reasons: 1. Turbulence modelling and 2. Surface roughness. It has been recorded in literature that the surfaces from additive manufacturing can have high roughness and this roughness can enhance the heat transfer. The Nusselt number prediction for the flat plate case was much better with maximum error of 18%.

A graphite heater was designed by the experimental team for the high temperature inlet flow in heat exchangers. Running many experiments on this heater is resource consuming, therefore it is beneficial to use CFD to predict the performance of the graphite heater. The graphite heater works on the principle of Joule heating. In addition to the energy equation, an additional equation for the electric potential is also solved. This increases the complexity of the problem. The outlet temperature prediction from CFD was within 5 % of the experimental value.

Full scale heat exchanger simulations are carried out in ANSYS Fluent to predict the performance of the heat exchangers. The simulations are run for various mass flow rates, configurations, geometry and fin shapes. CFD really shows its advantage over experiments in being to able to gather the performance for many design points quickly. The maximum performance for the heat exchanger assembly observed is for the $40^o$ twisted fins in the 12.5 cm x 12.5 cm heat exchanger. The maximum specific power observed is 9.37 KW/kg with an effectiveness of 0.618 and NTU of 1.108. The pressure drop on the hot side is much higher than the cold side. Arranging the fins along the streamline helps in reducing the pressure drop.

This thesis has explored the use of CFD for design of equipment. Even though comprehensive work has been completed as a part of this thesis, there are still some gaps which can be filled by further research. There is still a mismatch in the data between CFD and experiments for rough surfaces. There is scope to improve CFD modelling to be able to account for the roughness generated by additive manufacturing processes. The 3D twisted fins have been studied upto a certain extent, there is scope to do an optimization problem to find the most optimal fin shape for different operating conditions. The

graphite heater can be optimized to increase its heat transfer performance.

## REFERENCES


[1] Arjen Jacco Hoekstra. Gas flow field and collection efficiency of cyclone separators. 2000.

[2] Long Ni, Jinyi Tian, Tao Song, Yongson Jong, and Jianing Zhao. Optimizing geometric parameters in hydrocyclones for enhanced separations: a review and perspective. *Separation & Purification Reviews*, 48:30–51, 2019.

[3] B Dabir and CA Petty. Laser Doppler anemometry measurements of tangential and axial velocities in a hydrocyclone operating without an air core. In *Second International Conference on Hydrocyclone. BHRA, England*, pages 15–26, 1984.

[4] Luo Quian, Deng Changlie, Xu Jirun, Yu Lixin, and Xiong Guangai. Comparison of the Performance of Water-Sealed and Commercial Hydrocyclones. *International Journal of Mineral Processing*, 25:297–310, 1989.

[5] GQ Dai, WM Chen, JM Li, and LY Chu. Experimental study of solid–liquid two-phase flow in a hydrocyclone. *Chemical Engineering Journal*, 74:211–216, 1999.

[6] Jiangang Wang, Zhishan Bai, Qiang Yang, Yi Fan, and Hualin Wang. Investigation of the simultaneous volumetric 3-component flow field inside a hydrocyclone. *Separation and Purification Technology*, 163:120–127, 2016.

[7] Zhengliang Liu, Ying Zheng, Lufei Jia, Jinyu Jiao, and Qikai Zhang. Stereoscopic PIV studies on the swirling flow structure in a gas cyclone. *Chemical Engineering Science*, 61:4252–4261, 2006.

[8] S Vengadesan and P Nithiarasu. Hybrid LES—Review and assessment. *Sadhana*, 32(5):501, 2007.

[9] Teja Reddy Vakamalla and Narasimha Mangadoddy. Numerical simulation of industrial hydrocyclones performance: Role of turbulence modelling. *Separation and Purification Technology*, 176:23–39, 2017.

[10] Zhuwei Gao, Juan Wang, Jiangyun Wang, Yu Mao, and Yaodong Wei. Analysis of the effect of vortex on the flow field of a cylindrical cyclone separator. *Separation and Purification Technology*, 211:438–447, 2019.

[11] Shuyan Wang, Haolong Li, Ruichen Wang, Xu Wang, Ruichao Tian, and Qiji Sun. Effect of the inlet angle on the performance of a cyclone separator using CFD-DEM. *Advanced Powder Technology*, 30:227–239, 2019.

[12] Yefang Wang, Fan Zhang, Shouqi Yuan, Ke Chen, Xueyuan Wei, and Desmond Appiah. Effect of URANS and Hybrid RANS-Large Eddy Simulation Turbulence Models on Unsteady Turbulent Flows Inside a Side Channel Pump. *Journal of Fluids Engineering*, 142(6), 2020.

[13] H Sajjadi, M Salmanzadeh, G Ahmadi, and S Jafari. Hybrid les/rans model for simulation of particle dispersion and deposition. In *ASME 2018 5th Joint US-European Fluids Engineering Division Summer Meeting*. American Society of Mechanical Engineers Digital Collection, 2018.

[14] Mohammad Safavi and Ehsan Amani. A comparative study of turbulence models for non-premixed swirl-stabilized flames. *Journal of Turbulence*, 19(11-12):1017–1050, 2018.

[15] Han Li, Qiaogao Huang, Guang Pan, and Xinguo Dong. The transient prediction of a pre-swirl stator pump-jet propulsor and a comparative study of hybrid rans/les simulations on the wake vortices. *Ocean Engineering*, 203:107224, 2020.

[16] KT Hsieh and RK Rajamani. Mathematical model of the hydrocyclone based on physics of fluid flow. *AIChE Journal*, 37(5):735–746, 1991.

[17] H Tofighian, E Amani, and M Saffar-Avval. A large eddy simulation study of cyclones: The effect of sub-models on efficiency and erosion prediction. *Powder Technology*, 360:1237–1252, 2020.

[18] S Kazemi, M Adib, and E Amani. Numerical study of advanced dispersion models in particle-laden swirling flows. *International Journal of Multiphase Flow*, 101:167–185, 2018.

[19] SB Pope. Lagrangian PDF Methods for Turbulent Flows. *Annu. Rev. Fluid Mech*, 23:63, 1994.

[20] M Sommerfeld. Some open questions and inconsistencies of lagrangian particle dispersion models. In *Proc. of 9th Symp. on Turbulent Shear Flows*, volume 15, 1993.

[21] J Lipowsky and M Sommerfeld. Les-simulation of the formation of particle strands in swirling flows using an unsteady euler-lagrange approach. In *Proceedings of the 6th International Conference on Multiphase Flow, ICMF*, 2007.

[22] Iain Finnie. Erosion of surfaces by solid particles. *Wear*, 3(2):87–103, 1960.

[23] Y Zhang, EP Reuterfors, B Sf McLaury, SA Shirazi, and EF Rybicki. Comparison of computed and measured particle velocities and erosion in water and air flows. *Wear*, 263(1-6):330–338, 2007.

[24] JH Neilson and A Gilchrist. Erosion by a stream of solid particles. *Wear*, 11(2):111–122, 1968.

[25] Ganghui Liu, Weibing Wang, Junzhi Yu, and Xiaojun Li. Effect of extra inlets structure on cyclone wall erosion. *Powder Technology*, 411:117926, 2022.

[26] G Grant and Widen Tabakoff. Erosion prediction in turbomachinery resulting from environmental solid particles. *Journal of Aircraft*, 12(5):471–478, 1975.

[27] Alister Forder, Martin Thew, and David Harrison. A numerical investigation of solid particle erosion experienced within oilfield control valves. *Wear*, 216(2):184–193, 1998.

[28] Yong-Du Jun and Widen Tabakoff. Numerical Simulation of a Dilute Particulate Flow (Laminar) Over Tube Banks. *Journal of Fluids Engineering*, 116(4):770–777, 12 1994.

[29] Sajed Naiemi Dizajyekan, Gholamhossein Shahgholi, Adel Rezvanivand Fanaei, Vahid Rostampour, Vali Rasooli Sharabiani, Mariusz Szymanek, and Ryszard Kulig. Evaluation of Centrifugal Force, Erosion, Strain Rate, and Wall Shear in a Stairmand Cyclone. *Processes*, 10(5):994, 2022.

[30] YI Oka and T Yoshida. Practical estimation of erosion damage caused by solid particle impact: Part 2: Mechanical properties of materials directly associated with erosion damage. *Wear*, 259(1-6):102–109, 2005.

[31] Ehsan Dehdarinejad and Morteza Bayareh. Impact of non-uniform surface roughness on the erosion rate and performance of a cyclone separator. *Chemical Engineering Science*, 249:117351, 2022.

[32] SB Karri, Ray Cocco, and Ted Knowlton. Erosion in Second Stage Cyclones: Effects of Cyclone Length and Outlet Gas Velocity. In *10th International Conference on Circulating Fluidized Beds and Fluidization Technology - CFB-10*, 2013.

[33] Farzad Parvaz, Seyyed Hossein Hosseini, Khairy Elsayed, and Goodarz Ahmadi. Numerical investigation of effects of inner cone on flow field, performance and erosion rate of cyclone separators. *Separation and Purification Technology*, 201:223–237, 2018.

[34] Thiana Alexandra Sedrez, Rodrigo Koerich Decker, Marcela Kotsuka da Silva, Dirceu Noriler, and Henry França Meier. Experiments and CFD-based erosion modeling for gas-solids flow in cyclones. *Powder Technology*, 311:120–131, 2017.

[35] Det Norske Veritas. Recommended practice rp o501 erosive wear in piping systems. *DNV Recommended Practice*, 4, 2007.

[36] Honggang Yang, Nan Wang, Yingxue Cao, Xiaojing Meng, and Lei Yao. Effects of helical fins on the performance of a cyclone separator: A numerical study. *Advanced Powder Technology*, 34(1):103929, 2023.

[37] Chuanjun Han, Yang Hu, Wenying Li, and Qin Bie. Gas-solid separation performance and structure optimization in 3d printed guide vane cyclone separator. *Advanced Powder Technology*, 33(11):103815, 2022.

[38] Shuangcheng Fu, Faqi Zhou, Guogang Sun, Huixin Yuan, and Jie Zhu. Performance evaluation of industrial large-scale cyclone separator with novel vortex finder. *Advanced Powder Technology*, 32(3):931–939, 2021.

[39] Jihai Duan, Shun Gao, Yuanchun Lu, Weiwen Wang, Pan Zhang, and Chaojie Li. Study and optimization of flow field in a novel cyclone separator with inner cylinder. *Advanced Powder Technology*, 31(10):4166–4179, 2020.

[40] Zhuwei Gao, Zhongxin Liu, Zhenhua Song, Chengxin Li, Xinyu Qi, Haoran Ling, and Yaodong Wei. Peculiarities of particle motion inside cyclone separator by using les-drw model. *Chemical Engineering Research and Design*, 2022.

[41] Lehui Zhang, Junling Fan, Pan Zhang, Fei Gao, Guanghui Chen, and Jianlong Li. Effect of local erosion on the flow field and separation performance of the cyclone separator. *Powder Technology*, page 118007, 2022.

[42] Carlos Antonio Ribeiro Duarte, Francisco José de Souza, and Vinicius Fagundes dos Santos. Mitigating elbow erosion with a vortex chamber. *Powder Technology*, 288:6–25, 2016.

[43] Vaclav Dostal, Pavel Hejzlar, and Michael J Driscoll. High-performance supercritical carbon dioxide cycle for next-generation nuclear reactors. *Nuclear technology*, 154(3):265–282, 2006.

[44] Joo Hyun Park and Moo Hwan Kim. Experimental investigation on comprehensive thermal-hydraulic performance of supercritical co2 in a naca 0020 airfoil fin printed circuit heat exchanger. *International Journal of Heat and Mass Transfer*, 220:124947, 2024.

[45] Nobuyoshi Tsuzuki, Yasuyoshi Kato, Konstantin Nikitin, and Takao Ishizuka. Advanced microchannel heat exchanger with s-shaped fins. *Journal of nuclear science and technology*, 46(5):403–412, 2009.

[46] Dong Eok Kim, Moo Hwan Kim, Jae Eun Cha, and Seong O Kim. Numerical investigation on thermal–hydraulic performance of new printed circuit heat exchanger model. *Nuclear Engineering and Design*, 238(12):3269–3276, 2008.

[47] Tri Lam Ngo, Yasuyoshi Kato, Konstantin Nikitin, and Nobuyoshi Tsuzuki. New printed circuit heat exchanger with s-shaped fins for hot water supplier. *Experimental Thermal and fluid science*, 30(8):811–819, 2006.

[48] Tri Lam Ngo, Yasuyoshi Kato, Konstantin Nikitin, and Takao Ishizuka. Heat transfer and pressure drop correlations of microchannel heat exchangers with s-shaped and zigzag fins for carbon dioxide cycles. *Experimental Thermal and Fluid Science*, 32(2):560–570, 2007.

[49] Nobuyoshi Tsuzuki, Motoaki Utamura, and Tri Lam Ngo. Nusselt number correlations for a microchannel heat exchanger hot water supplier with s-shaped fins. *Applied Thermal Engineering*, 29(16):3299–3308, 2009.

[50] X Zhang, X Sun, RN Christensen, and M Anderson. Preliminary structural assessment of a printed circuit heat exchanger with s-shaped fins. *NURETH-16, Chicago, IL*, pages 7674–7687, 2015.

[51] Miao Ding, Jian Liu, Wen-Long Cheng, Wen-Xu Huang, Qi-Nie Liu, Lei Yang, and Shi-Yi Liu. An adaptive flow path regenerator used in supercritical carbon dioxide brayton cycle. *Applied Thermal Engineering*, 138:513–522, 2018.

[52] Chen Zeng, Yinxi Song, Xiang Zhou, Feixi Zhang, Ming Jiao, Maolong Liu, and Hanyang Gu. Experimental study on heat transfer and pressure drop characteristics in a microchannel heat exchanger assembly with s-shaped fins. *Applied Thermal Engineering*, 210:118406, 2022.

[53] Zhenghua Rao, Tianchen Xue, Kaixin Huang, and Shengming Liao. Multi-objective optimization of supercritical carbon dioxide recompression brayton cycle considering printed circuit recuperator design. *Energy Conversion and Management*, 201:112094, 2019.

[54] Jun-Ming Yin, Qiu-Yun Zheng, and Xin-Rong Zhang. Comparative study on the thermal-hydraulic performance of a shell and plate particle-sco2 moving packed bed heat exchanger with various channel configurations. *Applied Thermal Engineering*, 181:115946, 2020.

[55] Fanli Kong, Chi Xu, Yijiang Fan, Dali Yu, Jie Yu, and Shuyong Liu. Design and assessment of lead–sco2 intermediate heat exchanger for lfrs. In *E3S Web of Conferences*, volume 236, page 01012. EDP Sciences, 2021.

[56] Vladimir Kindra, Ivan Komarov, Sergey Osipov, Olga Zlyvko, and Igor Maksimov. Feasibility study of the co2 regenerator parameters for oxy-fuel combustion power cycle. *Inventions*, 7(3):66, 2022.

[57] Henry G Weller, Gavin Tabor, Hrvoje Jasak, and Christer Fureby. A tensorial approach to computational continuum mechanics using object-oriented techniques. *Computers in physics*, 12:620–631, 1998.

[58] F. R. Menter, M. Kuntz, and R. Langtry. *Ten Years of Industrial Experience with the SST Turbulence Model*. Begell House, Inc., 2003.

[59] Mishra, Aashwin Ananda and Mukhopadhaya, Jayant and Iaccarino, Gianluca and Alonso, Juan. Uncertainty estimation module for turbulence model predictions in SU2. *AIAA Journal*, 57:1066–1077, 2019.

[60] Brian Edward Launder, G Jr Reece, and W Rodi. Progress in the development of a Reynolds-stress turbulence closure. *Journal of Fluid Mechanics*, 68:537–566, 1975.

[61] H Shalaby, K Pachler, K Wozniak, and G Wozniak. Comparative study of the continuous phase flow in a cyclone separator using different turbulence models. *International journal for numerical methods in fluids*, 48(11):1175–1197, 2005.

[62] Mishra, Aashwin A and Girimaji, Sharath S. Toward approximating non-local dynamics in single-point pressure–strain correlation closures. *J. Fluid Mech*, 811:168–188, 2017.

[63] Mishra, Aashwin A and Girimaji, Sharath S. Intercomponent energy transfer in incompressible homogeneous turbulence: multi-point physics and amenability to one-point closures. *Journal of Fluid Mechanics*, 731:639–681, 2013.

[64] Osami Kitoh. Experimental study of turbulent swirling flow in a straight pipe. *Journal of fluid mechanics*, 225:445–479, 1991.

[65] Aashwin Ananda Mishra and Sharath Girimaji. Linear analysis of non-local physics in homogeneous turbulent flows. *Physics of Fluids*, 31(3):035102, 2019.

[66] MA Leschziner and S Hogg. Computation of highly swirling confined flow with a reynolds stress turbulence model. *AIAA journal*, 27(1):57–63, 1989.

[67] S. Poncet, S. Viazzo, and R. Oguic. Large eddy simulations of Taylor-Couette-Poiseuille flows in a narrow-gap system. *Physics of Fluids*, 26:105–108, 2014.

[68] F. Nicoud and F. Ducros. Subgrid-scale stress modelling based on the square of the velocity gradient tensor. *Flow, Turbulence and Combustion*, 62:183–200, 1999.

[69] M Strelets. Detached Eddy Simulation of massively separated flows. In *39th Aerospace sciences meeting and exhibit*, page 879, 2001.

[70] Mikhail S Gritskevich, Andrey V Garbaruk, Jochen Schütze, and Florian R Menter. Development of DDES and IDDES formulations for the k-$\omega$ shear stress transport model. *Flow, Turbulence and Combustion*, 88:431–449, 2012.

[71] Bruno Chaouat. The state of the art of hybrid RANS/LES modeling for the simulation of turbulent flows. *Flow, Turbulence and Combustion*, 99:279–327, 2017.

[72] Jeongseog Oh, Sangil Choi, and Jeonggeun Kim. Numerical simulation of an internal flow field in a uniflow cyclone separator. *Powder Technology*, 274:135–145, 2015.

[73] Carlos Oropeza-Vazquez. *Multiphase flow separation in Liquid-Liquid cylindrical cyclone and Gas-Liquid-Liquid cylindrical cyclone compact separators*. PhD thesis, Citeseer, 2001.

[74] AJ Hoekstra, JJ Derksen, and HEA Van Den Akker. An experimental and numerical study of turbulent swirling flow in gas cyclones. *Chemical engineering science*, 54(13-14):2055–2065, 1999.

[75] AJ Hoekstra, E Van Vliet, JJ Derksen, and HEA Van den Akker. Vortex core precession in a gas cyclone. In *Advances in Turbulence VII*, pages 289–292. Springer, 1998.

[76] Links Schiller. A drag coefficient correlation. *Zeit. Ver. Deutsch. Ing.*, 77:318–320, 1933.

[77] Renwei Mei. An approximate expression for the shear lift force on a spherical particle at finite reynolds number. *International Journal of Multiphase Flow*, 18(1):145–147, 1992.

[78] Renwei Mei and JF Klausner. Shear lift force on spherical bubbles. *International journal of heat and fluid flow*, 15(1):62–65, 1994.

[79] Sol I Rubinow and Joseph B Keller. The transverse force on a spinning sphere moving in a viscous fluid. *Journal of Fluid Mechanics*, 11(3):447–459, 1961.

[80] M Sommerfeld et al. Theoretical and experimental modelling of particulate flows. *Lecture series*, 6:3–7, 2000.

[81] SCR Dennis, SN Singh, and DB Ingham. The steady flow due to a rotating sphere at low and moderate reynolds numbers. *Journal of Fluid Mechanics*, 101(2):257–279, 1980.

[82] Todd L Bocksell and E Loth. Stochastic modeling of particle diffusion in a turbulent boundary layer. *International journal of multiphase flow*, 32(10-11):1234–1253, 2006.

[83] Y. Zhang, E.P. Reuterfors, B.S. McLaury, S.A. Shirazi, and E.F. Rybicki. Comparison of computed and measured particle velocities and erosion in water and air flows. *Wear*, 263(1):330–338, 2007. 16th International Conference on Wear of Materials.

[84] Gabriel Chucri Pereira, Francisco José de Souza, and Diego Alves de Moro Martins. Numerical prediction of the erosion due to particles in elbows. *Powder Technology*, 261:105–117, 2014.

[85] M Sommerfeld and N Huber. Experimental analysis and modelling of particle-wall collisions. *International journal of multiphase flow*, 25(6-7):1457–1489, 1999.

[86] Michael Breuer, Michael Alletto, and Felix Langfeldt. Sandgrain roughness model for rough walls within eulerian–lagrangian predictions of turbulent flows. *International journal of multiphase flow*, 43:157–175, 2012.

[87] Jakob Hærvig. jakobhaervig/cyclicTemperatureFoam: cyclicTemperatureFoam - An OpenFOAM solver for cyclic heat transfer, May 2018.

[88] S. V. Patankar, C. H. Liu, and E. M. Sparrow. Fully Developed Flow and Heat Transfer in Ducts Having Streamwise-Periodic Variations of Cross-Sectional Area. *Journal of Heat Transfer*, 99(2):180–186, 05 1977.

[89] Allen Bjerg and Kristian Christoffersen. *Numerical Investigation of Flow Structures and Their Impact on Heat Transfer Performance in a Staggered Arrangement of Rectangular Winglet Pair Vortex Generators in a Fully Developed Channel Flow.* PhD thesis, Aalborg University, 2015.

[90] Himani Garg, Lei Wang, and Christer Fureby. Heat transfer enhancement with additively manufactured rough surfaces: Insights from large-eddy simulations. *Physics of Fluids*, 36(2), 2024.

[91] Haynes International. *Haynes 214*, 2017.

[92] Sonun Ulan kyzy, Rainer Völkl, Oliver Munz, Tim Fischer, Sarah Welzenbach, and Uwe Glatzel. Thermo-physical properties of Hastelloy X and Haynes 214 close to the melting range. *Materials Science and Technology*, 36(10):1012–1019, 2020.